Controlling the Correlated State of Matter at Oxide Interfaces

Inauguraldissertation
zur
Erlangung der Würde eines Doktors der Philosophie
vorgelegt der
Philosophisch-Naturwissenschaftlichen Fakultät
der Universität Basel

von

Federico Stramaglia

2024

Genehmigt von der Philosophisch-Naturwissenschaftlichen Fakultät

auf Antrag von

Erstbetreuer/in: Prof. Dr. Frithjof Nolting

Dr. Carlos A. F. Vaz

Zweitbetreuer/in: Prof. Dr. Christian Schönenberger

Externe/r Experte/in: Prof. Dr. Christian Bernhard

Basel, 19/12/2023

Prof. Dr. Marcel Mayor, Dekan

Contents

1 Introduction

The disruption of the translational symmetry, which naturally occurs at the interface between different materials, is accompanied by modified electronic and magnetic states, resulting in the observation of novel and exotic properties that differ significantly from the bulk. The control of the unique properties found at the interface becomes of particular interest for future technologies. Examples of widely investigated interfacial effects include the electronic reconstruction occurring at polar oxides interfaces [1, 2], with the appearance in some cases of an interfacial 2D electron gas state with exotic electronic, superconducting and magnetic properties [3–5]; the control of the superconducting properties of thin cuprate films achieved by applying an electric field [6, 7] and electron-spin scattering at the interfaces of multilayer systems. A further example is the magnetoelectric coupling at the interface between ferroelectric and ferromagnetic systems – so-called artificial multiferroics – whereby the order parameters of the two materials, i.e., ferroelectricity and magnetism, are coupled either through elastic, spin exchange or charge interactions across the interface [8, 9]. In this thesis, I investigate the magnetic, electronic and structural properties of thin manganite films, both as single layers and in heterostructures, with the goal of improving their properties and to understand their behavior and interactions. In particular, the aim is to investigate the interfacial correlated state in manganite-titanate and manganite-manganite heterostructures, by exploiting the element selectivity of soft x-rays to probe the magnetic and orbital state of the manganite layer. Several effects, such as spin-exchange, charge leakage, charge screening, interdiffusion and strain-induced distortions are investigated in order to control the interfacial state and to tune the properties of the manganites, with the final goal of controlling the interfacial magnetic properties in view

of future technological applications.

Strongly correlated oxides give the perfect playground to engineer systems with peculiar interfacial properties, because of the strong correlation between spin, charge and lattice distortions; their similar crystal structure allows the deposition of epitaxial thin films. Among several oxides, the colossal magnetoresistance manganites are of peculiar interest when grown as thin films: their electronic malleability allows one to control magnetism through several parameters such as strain, thickness and hole doping; this is manifest in the phase diagrams of hole-doped manganites, exhibiting a big variety of magnetic and electronic states [10–19]. The main physics of manganites, with a general formula $AMnO_3$, where A is a divalent or trivalent alkaline earth, is determined by the Mn $3d$ orbital state which hybridizes with the O $2p$ orbitals surrounding the Mn in an octahedral environment. Therefore, the magnetic and electric properties of manganites can be controlled through the interplay of several parameters such as doping, strain and thickness, which strongly modify the number of electrons in the Mn $3d$ orbital or their shapes.

Despite the large amount of research carried out on the colossal magnetoresistance manganites, some fundamental aspects are still lacking an explanation. As an example, $La_{1-x}Sr_xMnO_3$ grown as thin film on $SrTiO_3$ is known to have degraded properties at the interface with the substrate, observed in the formation of a magnetic dead layer; this fact implies the necessity of depositing a relatively thick film in order to have robust magnetic and transport properties, at the expense of the interfacial effects, which become less significant when the film thickness is increased. Although the origin of the dead layer is still controversial [20–32], several studies were dedicated to improving the interfacial magnetic properties of the $La_{1-x}Sr_xMnO_3$; the general approach is to disentangle the film from the substrate by introducing an antiferromagnetic buffer layer, resulting in some cases in full spin polarization, by exploiting spin and charge exchange [22,33–36]. A particular case concerns the introduction of a $LaMnO_3$ buffer layer [22,33,34]: the magnetic properties of relatively thick manganite films (of the order of 120-150 nm) in $La_{1-x}A_xMnO_3/LaMnO_3/SrTiO_3$ heterostructures were investigated, resulting in improved interfacial properties when the $LaMnO_3$ buffer layer is introduced at the interface with the $SrTiO_3$ substrate. Nevertheless, some questions remained open, such as what happens if one uses $La_{0.8}Sr_{0.2}MnO_3$ films, i.e., when the system is at the border between two competing ground states, or if the film thickness is reduced down to 1 unit cell. In chapter 4, I use antiferromagnetic conducting $La_{0.45}Sr_{0.55}MnO_3$ and nominally antiferromagnetic insulating $LaMnO_3$ buffer layers to improve the interfacial properties of ultrathin $La_{0.8}Sr_{0.2}MnO_3$ films, which show full spin polarization down to 1 unit cell (uc) thickness when a $LaMnO_3$ buffer layer is used. The latter, although in its bulk form is an A-type antiferromagnetic insulator, when grown as thin film develops a net magnetic moment, whose origin is still today controversial [37–51]. The ferromagnetic spin alignment of the $LaMnO_3$

may play an important role in reducing the dead layer of the $La_{1-x}Sr_xMnO_3$ through spin-exchange. Several studies point to a strain effect or interaction with the substrate, while some others to off-stoichiometry for the appearance of the magnetic moment. Here, I show through x-ray photoemission spectroscopy that interdiffusion of Sr or Ca from the substrate into the film is responsible for a slight hole doping in the $LaMnO_3$ film up to the surface, probably leading to a spin canted or ferromagnetic state. The results for the $La_{0.45}Sr_{0.55}MnO_3$ buffer layer are different, showing no net magnetic moment up to 4 uc thickness of the top $La_{0.8}Sr_{0.2}MnO_3$ layer. The magnetic coupling of the $La_{0.8}Sr_{0.2}MnO_3$ layer with the $La_{0.45}Sr_{0.55}MnO_3$ buffer layer is also investigated using photoemission electron microscopy, showing an antiferromagnetic alignment up to 3 uc; starting from 4 uc thickness, a ferromagnetic contrast is observed, in agreement with the bulk magnetometry results.

Regardless of the dead layer, the decrease in the Curie temperature observed with decreasing $La_{1-x}Sr_xMnO_3$ film thickness [52–54] and attributed to a decrease of the in-plane transfer integral caused by tensile strain, may still represent a limit for future applications in ultrathin films, albeit, also in this case, the introduction of a buffer layer has been shown to be effective in reducing this strain-driven effect [55]. The opposite behavior was instead observed for $La_{1-x}Ba_xMnO_3$: an improvement of the magnetic properties (i.e., increase of the Curie temperature of about 30 K) has been observed with decreasing thickness from 200 to 20 nm [56]. A different interplay between orbital occupancy and in-plane lattice parameter among the different manganite systems seems to be responsible for such a different behavior, together with a different octahedral rotation due to the slightly different lattice mismatch with the substrate [18, 56, 57]. This aspect has never been addressed experimentally and is still only a theoretical prediction. Despite the interesting properties of $La_{1-x}Ba_xMnO_3$ for thin films applications, the $La_{1-x}Sr_xMnO_3$ remains the most studied system, mainly because of the relatively high Curie temperature.

Because of their interesting properties, colossal magnetoresistance manganites are often explored as magnetic layer in ferroelectric field-effect devices. The main idea behind this concept is to control the interfacial magnetic state through the application of a gate voltage to the ferroelectric layer, whose polarization is screened by the charge carriers; the accumulation or depletion of carriers at the interface results in a modified magnetic state. Differently from the field effect transistors, the large charge carrier density of the order of 10^{21} cm^{-3} results in a Thomas-Fermi screening length of the order of one unit cell [58–60], requiring ferroelectric gates to modulate the charge density at the interface up to 0.1 electron/unit cell in ferroelectric field-effect devices structures. The origin of charge-mediated magnetoelectric coupling was first explained by *Vaz et al.* in $Pb(Zr_{0.2}Ti_{0.8})O_3/La_{0.8}Sr_{0.2}MnO_3$ heterostructures [8] and Burton and Tsymbal in $BaTiO_3/La_{1-x}A_xMnO_3$ heterostructures [61]; subsequently, such magnetoelectric coupling attracted the

interest of the scientific community [62–69]. Of particular interest is the case of 0.2 and 0.5 doped $La_{1-x}Sr_xMnO_3$, i.e., where the system is at the boundary between two competing magnetic phases and is expected to be more susceptible to external perturbations. The magnetoelectric coupling with $La_{1-x}Ba_xMnO_3$ thin films has been less extensively studied, despite the peculiar properties of thin $La_{1-x}Ba_xMnO_3$ films. The few reports in the literature indicate an opposite behavior with respect to $La_{1-x}Sr_xMnO_3$ [70–72], whose understanding requires further investigation. In chapter 5 I report the first imaging of the magnetoelectric coupling in $BaTiO_3/La_{0.9}Ba_{0.1}MnO_3$ heterostructures. Square ferroelectric domains are written on the ferroelectric surface with atomic force microscopy in contact mode using a conducting tip. Several voltages ranging between ± 8 V are applied and the changes in the magnetic properties in the $La_{0.9}Ba_{0.1}MnO_3$ layer are imaged with x-ray photoemission electron microscopy.

The hole accumulation or depletion at the interface with the ferroelectric layer is accompanied by a different in-plane and out-of-plane orbital occupation, which in turn results in an antiferromagnetic or ferromagnetic alignment of the interfacial $La_{0.8}Sr_{0.2}MnO_3$ layer, respectively. The variation in the orbital occupation is explained based on a piezoelectric effect: the switching of the ferroelectric polarization results in elongated or contracted out-of-plane lattice parameter which, in turn, modifies the interfacial orbital shapes and the preferred orbital occupation of the $La_{0.8}Sr_{0.2}MnO_3$ layer [73–77]. Chapter 6 is dedicated to $La_{0.8}Sr_{0.2}MnO_3/BaTiO_3$ multiferroic hetetrostructures; in particular, the relation between orbital degree of freedom and magnetism is investigated. I report the first observation of the band structure of $La_{1-x}Sr_xMnO_3$ at 0.2 doping in $BaTiO_3/La_{0.8}Sr_{0.2}MnO_3$ heterostructures when the polarization of the ferroelectric $BaTiO_3$ is switched. The interfacial band structure is probed with soft x-ray angle resolved photoemission spectroscopy (ARPES), which has the advantage of probing buried interfaces in resonance with the Mn L-edge, enhancing the photoemission from the Mn d orbitals. As we switch the ferroelectric polarization of the $BaTiO_3$ layer, we see a rigid shift of the Fermi energy, which reflects the variation of the number of carriers modulated by the screening of the ferroelectric polarization. Furthermore, by taking advantage of the ARPES selection rules, the different d orbitals are probed, allowing us to link specific orbital variations to the modified interfacial magnetic properties. The magnetic profile of these samples is then investigated by resonant x-ray scattering. By combining the advantages of scattering and absorption techniques, resonant scattering gives information on the magnetic moment as well as on the atomic structure, allowing us to determine the magnetic profile across the film thickness and to localize the changes in the magnetic moment. Our results are consistent with previous polarized neutron reflectometry studies [78,79] and allow us to link specific variation of the orbital state to the interfacial magnetic configuration.

The colossal magnetoresistance manganites show interesting and peculiar properties which are often the result of the interplay between several degrees of freedom, such as charge, spin and orbital order, strain, thickness and local distortions. Therefore, the study of all these parameters is fundamental in order to fully describe the physics of manganites. The peculiar environment at PSI allows the use of several experimental techniques which can probe these different degrees of freedom, revealing of fundamental importance when dealing with complex strongly correlated oxides. The comprehensive understanding of thin films properties and interfacial effects is fundamental in order to engineer new materials with robust magnetic and electric properties at room temperature, specially in order to develop full polarized ultrathin films where the interfacial effects are much more important then in relatively thick films.

2 Physical Background

In this chapter I provide an overview of the physical properties of the manganites and titanates. The first section is dedicated to the physics of magnetism, where the main interaction mechanisms present in this thesis are summarized. I will then deal with the properties of the materials used in this study and discuss their magnetic and ferroelectric properties. The last section of this chapter is focused on the magnetoelectric coupling in multiferroic heterostructures.

2.1 Magnetic interactions

Although magnetism is a well-known phenomenon, a formal description was possible only in the last century, with the emergence of quantum mechanics. Nonetheless, a unified theory of magnetism is nowadays still missing. Here, we want to recall the basic principles behind the magnetic interactions, namely, the exchange integrals, to focus next on the magnetic interactions which are fundamental in colossal magnetoresistance manganite systems.

2.1.1 Direct exchange interaction

In order to derive the exchange interaction at the origin of magnetism, let us first discuss the $H_2{}^+$ molecule, i.e., two nuclei sharing a single electron. The following description is based on [80]. The hamiltonian of this problem can be written as

$$H(r) = \frac{p^2}{2m_\mathrm{e}} + \frac{\mathrm{e}^2}{4\pi\varepsilon_0}\frac{1}{|\mathbf{R}_B - \mathbf{R}_A|} - \frac{\mathrm{e}^2}{4\pi\varepsilon_0}\left[\frac{1}{|\mathbf{r} - \mathbf{R}_B|} + \frac{1}{|\mathbf{r} - \mathbf{R}_A|}\right] \qquad (2.1)$$

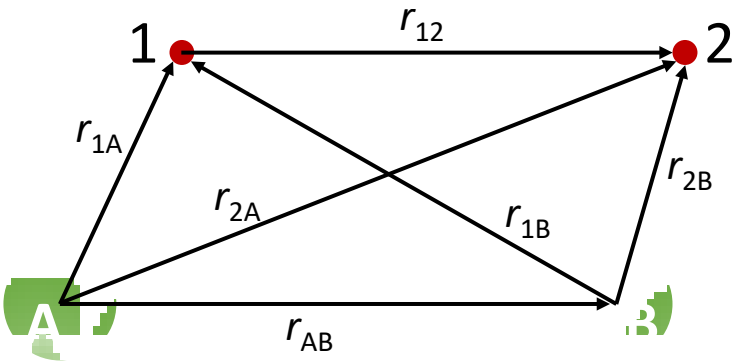

Figure 2.1: Representation of the H_2 molecule. The green spheres are the nuclei A and B, while the red ones represent the electrons 1 and 2.

Where $\mathbf{r}$, $\mathbf{R}_A$ and $\mathbf{R}_B$ are the position vectors of the electron and the hydrogen atoms A and B, respectively. The electronic wavefunction can be expressed as a linear combination of atomic orbitals (LCAO) as follows

$$|\psi_{\pm}\rangle = \frac{1}{\sqrt{2}}\left(|\phi_{\mathrm{a}}\rangle \pm |\phi_{\mathrm{b}}\rangle\right) \tag{2.2}$$

where $|\phi_a\rangle$ and $|\phi_b\rangle$ are the two electronic orbitals. We can now calculate the energy of this system by simple quantum mechanical relations: the atomic (E_0) and interaction (E_{ab}) energies are defined as follows

$$\begin{aligned} E_0 &= \langle\phi_{\mathrm{a}}|H|\phi_{\mathrm{a}}\rangle = \langle\phi_{\mathrm{b}}|H|\phi_{\mathrm{b}}\rangle \\ E_{\mathrm{ab}} &= \frac{\langle\phi_{\mathrm{b}}|H|\phi_{\mathrm{a}}\rangle}{\langle\phi_{\mathrm{b}}|\phi_{\mathrm{a}}\rangle} = E_{\mathrm{ba}} = \frac{\langle\phi_{\mathrm{a}}|H|\phi_{\mathrm{b}}\rangle}{\langle\phi_{\mathrm{a}}|\phi_{\mathrm{b}}\rangle} \end{aligned} \tag{2.3}$$

We note that the exchange energy E_{ab} drops exponentially to zero with the atomic distance, since the orbital overlap, defined as $O = \langle\phi_b|\phi_a\rangle = \langle\phi_a|\phi_b\rangle$, decays exponentially. The problem can be extended to a H_2 molecule through the simple Heitler-London model: we first split the hamiltonian into an unperturbed term (H_0) and a perturbation(H_1), defined as

$$\begin{aligned} H &= H_0 + H_1 \\ H_0 &= \underbrace{\frac{1}{2m}(p_1^2 + p_2^2)}_{\text{Electron kinetic energies}} \underbrace{- \frac{\mathrm{e}^2}{4\pi\varepsilon_0}\left(\frac{1}{r_{1\mathrm{A}}} + \frac{1}{r_{1\mathrm{B}}}\right)}_{\text{Electron-nucleus}} \\ H_1 &= \underbrace{\frac{\mathrm{e}^2}{4\pi\varepsilon_0}\left(\frac{1}{R_{\mathrm{AB}}}\right)}_{\text{Nucleus-nucleus}} + \underbrace{\frac{\mathrm{e}^2}{4\pi\varepsilon_0}\left(\frac{1}{r_{12}}\right)}_{\text{Electron-electron}} \underbrace{- \frac{\mathrm{e}^2}{4\pi\varepsilon_0}\left(\frac{1}{r_{1\mathrm{B}}} + \frac{1}{r_{2\mathrm{A}}}\right)}_{\text{Electron-nucleus}} \end{aligned} \tag{2.4}$$

where the distances are defined in Figure 2.1. In order to calculate the energies, we need to build the wavefunctions. For a two electron system,

the spin part of the wavefunction could be either a singlet (χ_s) or a triplet (χ_t) state; the radial part is chosen such that the total wavefunction is antisymmetric according to the Pauli exclusion principle. A simple solution to the problem can be found in the independent electrons picture, where the electron-electron interaction in equation 2.4 is neglected; in this scenario, we can use the LCAO approximation for the radial part of the wavefunction. The Heitler-London approximation consists of neglecting the ionic term in the radial wavefunction and considering only the covalent nature of the bond. This picture is particularly effective in the case of correlated or localized electrons. The two wavefunctions can be written as

$$\begin{aligned}\psi_s^{HL} &= \frac{1}{\sqrt{2(1-S)}}\left[\phi_a(\mathbf{r}_1)\phi_b(\mathbf{r}_2)+\phi_b(\mathbf{r}_1)\phi_a(\mathbf{r}_2)\right]\chi_s \\ \psi_t^{HL} &= \frac{1}{\sqrt{2(1+S)}}\left[\phi_a(\mathbf{r}_1)\phi_b(\mathbf{r}_2)-\phi_b(\mathbf{r}_1)\phi_a(\mathbf{r}_2)\right]\chi_t\end{aligned} \tag{2.5}$$

Here, S is the double overlap integral defined as

$$S = \langle\phi_a(\mathbf{r}_1)\phi_b(\mathbf{r}_2)|\phi_a(\mathbf{r}_2)\phi_b(\mathbf{r}_1)\rangle$$

The energies obtained in this model for the singlet and triplet states are

$$\begin{aligned}E_s &= \frac{\langle\psi_s^{HL}|H(\mathbf{r}_1,\mathbf{r}_2)|\psi_s^{HL}\rangle}{\langle\psi_s^{HL}|\psi_s^{HL}\rangle} = 2E_0+\frac{C+X}{1+S} \\ E_t &= \frac{\langle\psi_t^{HL}|H(\mathbf{r}_1,\mathbf{r}_2)|\psi_t^{HL}\rangle}{\langle\psi_t^{HL}|\psi_t^{HL}\rangle} = 2E_0+\frac{C-X}{1-S}\end{aligned} \tag{2.6}$$

where E_0 and S are the H atom energy and overlap integral, respectively. The Coulomb integral is defined as

$$C = \langle\phi_a(\mathbf{r}_1)\phi_b(\mathbf{r}_2)|H_1|\phi_a(\mathbf{r}_1)\phi_b(\mathbf{r}_2)\rangle \tag{2.7}$$

and the exchange integral as

$$X = \langle\phi_a(\mathbf{r}_2)\phi_b(\mathbf{r}_1)|H_1|\phi_a(\mathbf{r}_1)\phi_b(\mathbf{r}_2)\rangle \tag{2.8}$$

These last two terms arise from the perturbation in the hamiltonian. In particular, the exchange integral comes from the exchange of coordinates between the two electrons. The difference between the triplet and singlet state

$$E_s - E_t = 2J = 2\frac{X-SC}{1-S^2} \tag{2.9}$$

is the energy that the system needs in order to switch from a singlet to a triplet state. If X and C are zero, the two states are equivalent in energy, but if they are non-zero, one of the two states is favoured in energy and the spins are favourably parallel or antiparallel aligned. The difference between

the singlet and triplet state generally defines the exchange constant J, i.e., the singlet-triplet splitting is equal to $2J$. Summarizing, the singlet-triplet splitting has a fundamental role in magnetism: in some systems, in order to lower the exchange energy, the electrons tend to align their spins parallel or antiparallel, lowering the exchange energy and giving rise to magnetic phenomena. The exchange and Coulomb integrals are of great importance for magnetism in solids. Although the Heitler-London is a simple model, it is fundamental in the understanding of the solid state physics. Nonetheless, when dealing with solid crystals, further approximations, like Hartree-Fock, density functional theory or local density approximation, are needed, in order to include the electron-electron interactions. The many body problem is a complex topic which will not be treated here, but finds its starting point in the simple model just discussed.

In the discussed treatment, the hamiltonian does not contain the spin, which enters in the problem only by requiring that the total electronic wavefunction is antisymmetric. The exchange hamiltonian can be written in a different formalism, namely

$$H_{\text{exch}} = -\sum_{\text{i}\neq\text{j}} J_{\text{ij}}\mathbf{S}_{\text{i}} \cdot \mathbf{S}_{\text{j}} \tag{2.10}$$

where J_{ij} is the exchange integral and $\mathbf{S}_{\text{i}}$ and $\mathbf{S}_{\text{j}}$ the spins in the crystallographic positions i and j, respectively. The link between spin coupling and exchange interaction as we understand it nowadays comes from this picture, called Heisenberg model. The hamiltonian defined in equation 2.10 is the Heisenberg exchange hamiltonian and describes the direct interaction of spins in a solid; in one dimension, it reduces to the Ising model. The Heisenberg hamiltonian is particularly useful in the case of localized electrons. A second well known model for describing magnetism was developed by Hubbard, where the magnetic ground state is determined by the competition of two energies: the *hopping energy*, which involves the electron transfer between two different atoms, and the *Coulomb energy*, responsible for the electrostatic repulsion between two electrons. While the former favours itinerant or delocalized electrons, the latter interaction is responsible for the formation of localized moments. The Hubbard hamiltonian can be written as

$$H_{\text{Hub}} = -t \sum_{\sigma=\uparrow,\downarrow} \left(c^{\dagger}_{1\sigma} c_{2\sigma} + c^{\dagger}_{2\sigma} c_{1\sigma} \right) + U \left(n_{1\uparrow} n_{1\downarrow} + n_{2\uparrow} n_{2\downarrow} \right) \tag{2.11}$$

The operators $c^{\dagger}_{\text{i}\sigma}$ and $c_{\text{i}\sigma}$ respectively create and destroy an electron with spin σ on the atom i, while the operator $n_{\text{i}\sigma} = c^{\dagger}_{\text{i}\sigma} c_{\text{i}\sigma}$ is the number operator and counts the number of electrons on the atom i with spin σ. From these definitions, it is clear that the first term represents the hopping energy, with t being the transfer integral, while the second term is the Coulomb interaction, whose magnitude is determined by the Coulomb integral U. The Hubbard

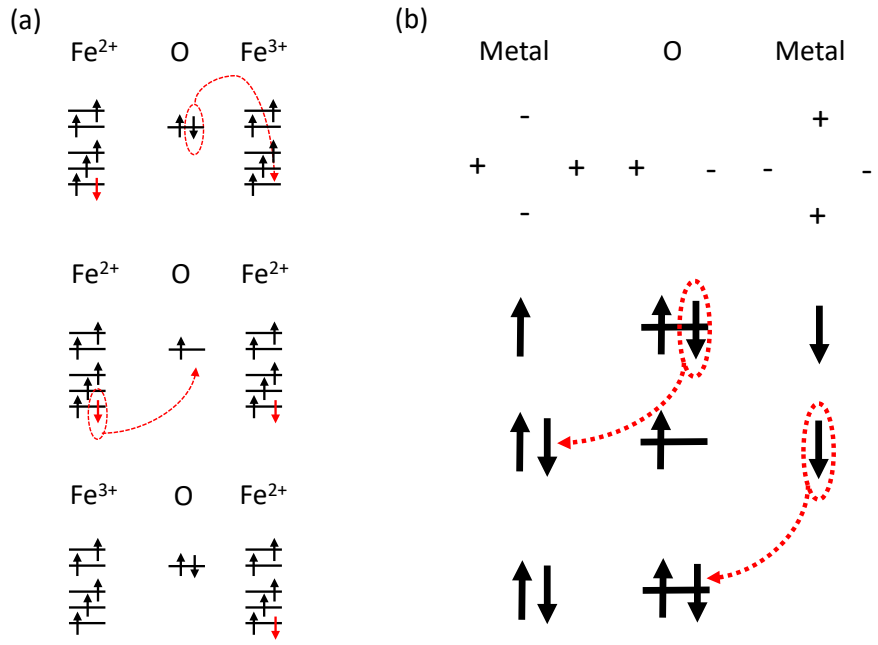

Figure 2.2: (a) Schematics of the double exchange process in the case of Fe in mixed 2+/3+ state. The red arrow represents the unpaired electron hopping through the oxygen p orbital, while the black arrows are the core spins, whose sum is indicated in the text by a double arrow. (b) Superexchange mechanism between two metal ions mediated by the oxygen p orbital, showing the electron hopping in the case of antiferromagnetic alignment of the two atoms.

model does not allow spin flips. The minimum of the energy of the system is obtained by minimizing two energy contribution in the most efficient way: the kinetic energy, given by t, and the Coulomb interaction U.

The discussion provided here ignores spin-orbit coupling and relativistic effects. Although in some systems these give important contributions to the magnetic ground state, it is not the case for the materials treated in this thesis. In the rest of this section, only the relevant magnetic interactions needed for the understanding of the physics of manganites are discussed. A complete treatment of magnetism can be found elsewhere [80, 81].

2.1.2 Double exchange

Double exchange is typically found in systems where the magnetic ion can be in two different oxidation states. A common example is the compound $La_{1-x}Sr_xMnO_3$, where the Mn atom is present in a mixed 3+/4+ oxidation state. The difference with the direct process is that the electron exchange between two cations happens here through the intermediary anion atom, which,

in the special case of manganites, is O^{2-}. The double exchange process, first introduced by Zener [82] and then developed by Anderson and Hasegawa [83] and de Gennes [84], is illustrated in Figure 2.2(a). Since the oxygen p orbital is fully occupied, the process must happen in two steps: first, an electron from the O orbital hops to the Mn; secondly, an electron from the other Mn atom fills the vacancy left by the previous electron in the O p orbital. Since spin flip is not allowed, this mechanism favours ferromagnetic alignment between the Mn atoms. From a formal point of view, the double exchange can be discussed in terms of the Hubbard model, from which the ground state energies can be obtained. A complete treatment is beyond the scope of this thesis [85]. Here, we just obtain the ground state energy in the simple case of Fe^{2+}/Fe^{3+} with spin pointing the same direction and we focus only on the spin part of the wavefunction. Three possible ground states are possible, listed in order of decreasing energy:

$$\begin{aligned} |\phi_3\rangle &= |\Uparrow\downarrow, \Uparrow\rangle + |\Uparrow, \Uparrow\downarrow\rangle\,, \quad & E_3 &= U + t \\ |\phi_2\rangle &= |\Uparrow\downarrow, \Downarrow\rangle\,, & E_2 &= U \\ |\phi_1\rangle &= |\Uparrow\downarrow, \Uparrow\rangle - |\Uparrow, \Uparrow\downarrow\rangle\,, \quad & E_1 &= U - t \end{aligned}$$

where the double arrow represents the core spin and the simple arrow an extra electron as shown in Figure 2.2. The wavefunction $|\phi_2\rangle$ corresponds to antiferromagnetic alignment of the Mn ions, while $|\phi_3\rangle$ and $|\phi_1\rangle$ are linear combinations of states where the Mn ions are aligned ferromagnetically. The corresponding energies are calculated using the Hubbard hamiltonian defined in equation 2.11. The lowest energy state is found for ferromagnetic alignment of the Fe spins, while the antiferromagnetic alignment has higher energy due to the impossibility to exchange an electron between adjacent Fe sites.

2.1.3 Superexchange and antiferromagnetism

Another important example of indirect exchange is superexchange, where the two magnetic ions are not in different oxidation states. An example of superexchange is found in $LaMnO_3$, where the Mn ions are in a 3+ oxidation state. The superexchange mechanism was first introduced by Kramers [86] in 1934 and later developed by Anderson [87, 88]. Figure 2.2(b) shows a sketch of the process between two magnetic ions, i.e., where at least one unpaired electron is present. It considers virtual electronic transitions between two ions with unfilled $3d$ shell. From a qualitative point of view, superexchange can be understood in terms of electron hopping from one Mn site to the next one: let us consider an electron with a well defined spin which is transferred through the oxygen p orbital, as represented in Figure 2.2(b). Since spin flip is forbidden, electron exchange is possible only if the two Mn atoms are aligned antiferromagnetically. Hence, superexchange favours the

antiferromagnetic ground state.[1] Intuitively, the process is similar to the one explained for the H_2 molecule, where the exchange integral lowers the energy of the system if the electrons align antiparallel, with the only difference that the exchange process is mediated by the oxygen p orbital. Analogously to the calculations performed in the case of double exchange, a more quantitative analysis can be performed using the Hubbard model: given the Mn atoms 1 and 2, we can write the eigenfunction of the system as $|\mathbf{S}_1, \mathbf{S}_2\rangle$, so that the eigenstates and eigenvalues in decreasing energy order are

$$\begin{aligned} |\phi_3\rangle &= |\uparrow\downarrow, 0\rangle - \frac{t}{U} |\uparrow, \downarrow\rangle , \quad & E_3 &= U + \frac{t^2}{U} \\ |\phi_2\rangle &= |\uparrow, \uparrow\rangle , & E_2 &= 0 \\ |\phi_1\rangle &= |\uparrow, \downarrow\rangle + \frac{t}{U} |\uparrow\downarrow, 0\rangle , \quad & E_1 &= -\frac{t^2}{U} \end{aligned}$$

It is clear that the lowest energy state, calculated with the Hubbard hamiltonian, corresponds to antiferromagnetic alignment. In this treatment, we have ignored the states where $\uparrow$ and $\downarrow$ are exchanged, which has only the consequence of adding a factor of 2 to the energies.

The Goodenough-Kanamori rules

Superexchange is a simple theory to explain antiferromagnetic alignment in complex oxides. Nonetheless, it cannot explain anisotropic exchange interactions, i.e., A or C-type antiferromagnetism. In these cases, the magnetic moments are aligned ferromagnetically in a selected plane and antiferromagnetically along the perpendicular direction; an example of A-type antiferromagnetic order can be found in bulk $LaMnO_3$. This is the main reason which lead Goodenough to develop his theory of semicovalence in 1955 [89]: the s and p empty orbitals close in energy to the valence ones cannot be ignored, but they hybridize and participate in the covalent bond with the intermediate oxygen atom. It is assumed that the hybrid orbitals are either d^2sp^3 or dsp^2, which possess octahedral and planar geometry, respectively, which match the perovskite structure typical of manganites. Let us consider an oxygen atom between two Mn ions with the same oxidation state. Four possible scenarios can occur (represented in Figure 2.3):

(a) *Two covalent bonds are possible.* Since the two electrons in the O orbital must have opposite spins, the two Mn atoms tend to align their spins antiferromagnetically. In this way, the electron hopping between the oxygen and Mn orbitals is favoured by the Hund rules.

(b) *Only one covalent bond is possible.* In this case, above the Curie temperature both electrons have the same probability of spending the same

[1] In particular cases, when the bond angle is 90°, the superexchange mechanism can favour ferromagnetism. Here, we restrict the discussion to the case of 180° bond angle.

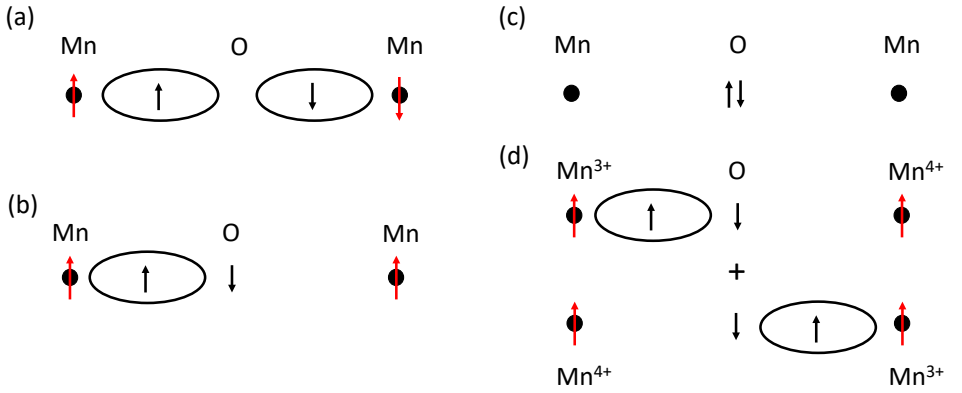

Figure 2.3: Representation of the four possible scenarios predicted by the Goodenough theory: (a) two covalent bonds lead to antiferromagnetic spin alignment of the Mn, (b) if only one covalent bond is possible, the Mn align ferromagnetically, (c) if no covalent bonds are formed, the system is in a paramagnetic state and (d) represents the case of double exchange, as the Mn is in mixed 3+/4+ state. The ellipses here represent a covalent bond between the O and the Mn atoms, while the red and black arrows are the core Mn and the O spins, respectively.

time on the Mn atom. Below the Curie temperature, in order to lower the exchange energy, the electron in the O orbital which creates a bond with the Mn atom has the same spin as the Mn. The electron left without coupling has the opposite spin, which results in a net magnetic moment of the oxygen atom which is opposite to the Mn spin. The neighbour Mn, which forms an ionic bond, aligns antiferromagnetically to the O atom because of direct exchange coupling, resulting in a ferromagnetic alignment of the Mn sites.

(c) *No covalent bonds are possible.* In this case, paramagnetic order will be dominant.

(d) *The two Mn atoms have different oxidation states.* In this case, double exchange occurs and ferromagnetism dominates the magnetic long range order.

With this representation, it is possible to correlate the orbital occupation with the magnetic order, describing the onset of A-type and C-type antiferromagnetism, as well as the CE spin configuration found experimentally in bulk $La_{1-x}Ca_xMnO_3$ with 0.5 doping, which could not be explained with the theory of superexchange as introduced by Kramers [90]. The symmetry of the orbitals is not considered in the development of this picture and is then introduced by Kanamori through the concept of orthogonality: in order to form a covalent bond, the two involved orbitals must be orthogonal,

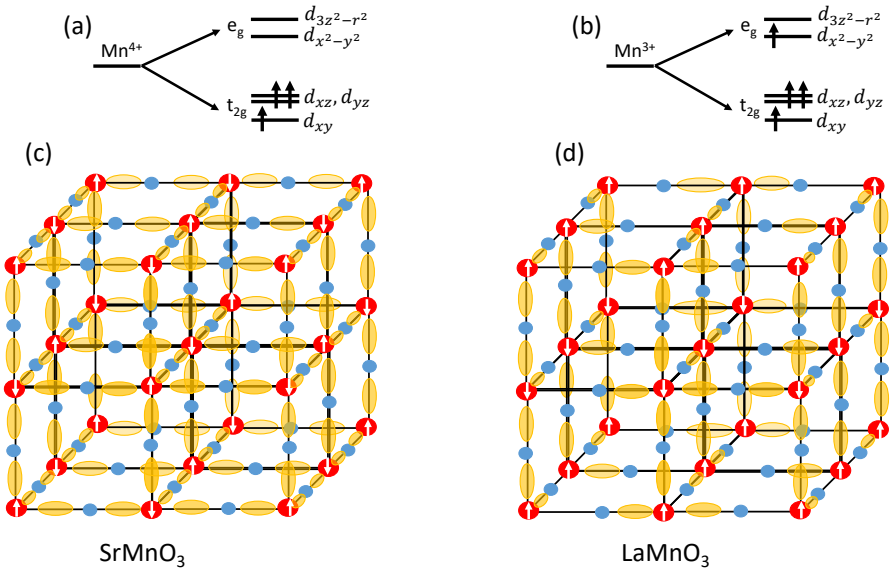

Figure 2.4: Energy level splitting for Mn^{4+} (a) and Mn^{3+} (b): as a consequence of the crystal field, the d orbitals are split into a lower energy t_{2g} and a higher energy e_g state. The tensile strain induced by the $SrTiO_3$ substrate is responsible for a further splitting of the d orbitals, as shown in Figure. (c) and (d): Orbital arrangement and spin configuration for M[II]MnO_3, where the Mn has oxidation state 4+, and $LaMnO_3$, with the Mn in the 3+ state, resulting in G-type and A-type antiferromagnetism, respectively. The red circles represent the Mn with their spin alignment shown with the white arrow, the blue circles are the oxygen atoms and the yellow ellipses the covalent bonds.

i.e., their integral over the whole space must vanish. Hence, the covalent bond can be formed only between specific orbitals, which adds a second constraint to the Goodenough theory; the ensemble of the two theories forms the Goodenough-Kanamori rules, which are fundamental to determining the magnetic ground state based on the orbital configuration of the magnetic ions and the surrounding environment.

We now apply the Goodenough theory to the $La_{1-x}M[II]_xMnO_3$ system, where M[II] is a divalent metal like Sr, Ca or Ba, to see the implications of the different orbital configurations on the magnetic properties.

(i) *The M[II]MnO_3 system.* Since M[II] is a divalent metal, it has oxidation state 2+ and the Mn ion is found in the 4+ valence state, resulting in 3 electrons occupying the $3d$ orbital. According to the Goodenough picture, the empty orbitals which are close in energy to the valence ones hybridize in the d^2sp^3 orbital, which possess octahedral symmetry and permits the Mn atom to form 6 covalent bonds with the six oxygen

atoms surrounding the Mn. Therefore, every oxygen is involved in covalent bonds in every direction and it will form two covalent bonds with the Mn, which, according to point (a) of the Goodenough-Kanamori rules, results in an antiferromagnetic alignment of the Mn ions. Figure 2.4(c) shows a schematic of the covalent bonds and the spin arrangement. This kind of antiferromagnetic order is called G-type and is characterized by all the nearest neighbours to be in an antiferromagnetic spin configuration.

(ii) *The $LaMnO_3$ system.* In the case of $LaMnO_3$, charge neutrality imposes 3+ oxidation state to the Mn ion, which means that four electrons occupy the $3d$ orbital. Since there are five empty orbitals (i.e., one $4s$, three $4p$ and one $3d$), the empty orbitals hybridize in the dsp^2 orbital (otherwise the geometry of the hybrid orbital would not be compatible with the octahedra) which has planar geometry. This choice implies that the oxygen forms only four covalent bonds, the other bonds being forced to be ionic since there are not enough free orbitals available on the Mn side. The bond configuration is shown schematically in Figure 2.4(d): along the c axis, the Mn atoms are always involved in a covalent bond, while in the ab plane the covalent bonds alternate, resulting in a ferromagnetic alignment in the plane, according to the Goodenough-Kanamori rule (b), and an out-of-plane antiferromagnetic alignment, as predicted by rule (a). The configuration of ferromagnetic planes aligned antiferromagnetically to the next plane in a stacking sequence along the c axis, as represented in Figure 2.4(d), is called A-type antiferromagnetism.

(iii) *The $La_{1-x}M[II]_xMnO_3$ system.* The intermediate doping regions are characterized by a mixed valence of the Mn atoms. Let us start our discussion in the $LaMnO_3$ case, and we slowly add hole carriers by doping the system with A. As soon as some Zener carriers are present, the antiferromagnetic configuration distorts into a spin-canted state, lowering the exchange energy [84]. In doping regions where a random distribution of the two valence states is possible, i.e., in the range $0.2 < x < 0.5$, the double exchange mechanism dominates the exchange integral and the system is in a ferromagnetic state. The case $x = 0.5$ is more complex: according to the Goodenough picture, the lowest energy state is a CE-type antiferromagnetic, which would only appear in case of charge and orbital ordering, which in turn implies an ordered arrangement of the 3+/4+ Mn ions. CE antiferromagnetism is characterized by the coexistence of both C and E-type antiferromagnetic order, the former similar to A-type but along the (110) plane, the latter comprising a more complex order where each cation has two neighbours with parallel and four neighbours with antiparallel spin

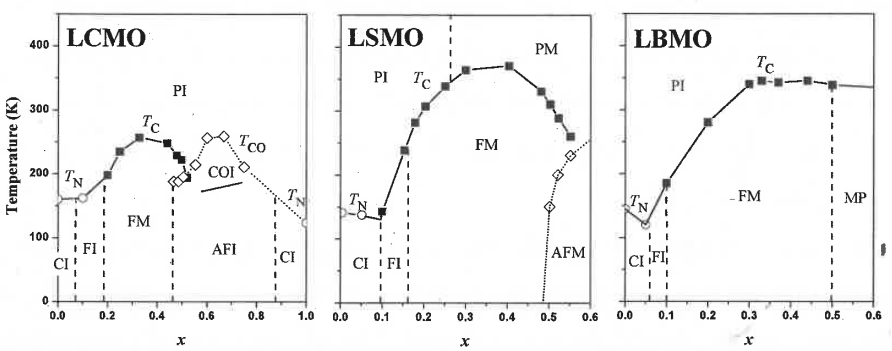

Figure 2.5: Magnetic phase diagram for Ca, Sr and Ba-doped $LaMnO_3$, named LCMO, LSMO and LBMO, respectively (from [96]).

configuration. In bulk systems, CE antiferromagnetism has been observed [91–93]; Chmaissem *et al.* report the observation of competing ferromagnetic and antiferromagnetic order [94], while in thin films the magnetic properties strongly depend on the choice of the substrate [95]. For $0.5 < x < 0.75$, the number of covalent bonds along the c axis increases and A-type antiferromagnetism is recovered. At 0.75 doping, the magnetic order becomes C-type and it gradually changes to the G-type antiferromagnetism as the doping increases to 1, recovering the magnetic state of the M[II]MnO_3 system.

2.2 Physics of the manganites

The colossal magnetoresistance manganites (CMR) are characterized by the structural formula $AMnO_3$, where A is a divalent or trivalent alkaline earth. The Mn atoms are surrounded by the O ions in an octahedral environment and the main physics in this system is determined by the outer Mn electrons which interact, through the O atom, with the other Mn. The effect of the A atom is to balance the charge, ensuring charge neutrality in the system. However, it has a big impact on the properties of the manganites: on one side, changing a trivalent ion for a divalent one, as in the case of Sr or Ba-doped $LaMnO_3$, the valence state of the Mn atom is changed to a mixed 3+/4+, having a big impact on the electronic and magnetic properties of the system. On the other hand, by varying the size of the A cation, the lattice parameters change, influencing the properties of the system through strain and chemical pressure.

2.2.1 Crystal and electronic structure

Manganites generally crystallize in the perovskite structure, where the Mn occupies the center of a pseudocube surrounded by the oxygen atoms in an octahedral environment; the A cation occupies the corners of the cubic structure. Nonetheless, the perfect perovskite structure is almost never encountered in real systems because of distortion phenomena which are generally present both in bulk and thin films [97]. The occupation of the outer Mn orbitals is responsible for the magnetic and electric properties of the system and plays a fundamental role in determining the ground state; the strong electron correlations in this band are responsible for the variety of interesting phenomena occurring in these materials. As already mentioned before, the oxygen octahedra has a strong influence on the properties of manganites, creating covalent bonds and hybridizing its orbitals with the Mn ones. The octahedral environment is also responsible of the degeneracy breaking of the d orbitals: because of the strong Coulomb repulsion between the electrons, the orbitals energetically favourable are the ones which do not point towards the O sites and have smaller overlap with the p orbitals, i.e., d_{xy}, d_{xz} and d_{yz}. The d orbitals are consequently split in e_g and t_{2g} states due to the crystal field, the energy separation between these two states is generally written as $10Dq$ and in the manganites it is of the order of 1-2 eV [98]. Further, the Mn-O-Mn bond angles are almost never planar; as an example, a bonding angle between 155° and 164° has been reported for stoichiometric $LaMnO_3$ [97].

2.2.2 Transport properties and colossal magnetoresistance

As already discussed, the phase diagram of the CMR manganites is very complex, presenting several magnetic and electronic configurations; the transport properties are strongly correlated to the magnetic ones. Indeed, in proximity to the Curie or Néel temperature, the resistivity shows a peak indicative of a metal to insulator transition. The change in the electronic properties is explained by Zener in terms of double exchange: the magnetic configuration of the system is such as to reduce the exchange integral and favours hopping of electrons between two Mn atoms through the oxygen ion. In this picture, below the transition temperature the transfer integral is reduced and the electrons hop more easily, changing the character of the system from insulating to metallic. Nonetheless, for compositions where the system is in a ferromagnetic ground state, a big drop in the resistivity is observed when a magnetic field is applied across the paramagnetic to ferromagnetic temperature [99]; this effect was called colossal magnetoresistance to distinguish it from the giant magnetoresistance observed in heterogeneous ferromagnetic materials [100]. However, the double exchange interaction is by itself not sufficient to explain this magnetoresistive effect, but the hamiltonian of the system needs to be modified. Millis *et al.* [101, 102] and Roder *et*

al. [103,104] proposed an additional term in the hamiltonian that accounts for electron-phonon coupling; other studies show that the CMR effect is due to a reduction of the localization by spin fluctuation scattering with the application of a magnetic field [105]. Although CMR is not investigated in this thesis, it has played a significant role in enhancing the interest of manganites for technological applications such as read-head hard drives, which are nowadays implemented with materials showing giant magnetoresistance.

2.2.3 Magnetism in colossal magnetoresistance manganites

The understanding of magnetism in the colossal magnetoresistance manganites is not trivial, and during the years several models have been proposed in order to fully understand and predict their behavior. The double exchange theory, first developed by Zener [82], was then adapted by Anderson and Hasegawa [83] in order to consider the bond angle between nearest neighbours; the effective hopping term is proportional to $\cos(\theta/2)$, introducing the idea that the hopping cancels for $\theta = \pi$, corresponding to an antiferromagnetic background. Also the idea of superexchange has seen many developments, leading to the introduction of the concept of semicovalent bonds by Goodenough. De Gennes [84] proposed a spin-canting behavior as a transition from antiferromagnetic behavior at $x = 0$ to ferromagnetic. Nonetheless, the CE-type antiferromagnetism predicted by Goodenough and observed in $La_{1-x}Ca_xMnO_3$ is not seen in the $La_{1-x}Sr_xMnO_3$ system at half doping, indicating that a comprehensive picture which could predict the magnetic behavior of manganites was still missing. Only later, when the electron-phonon coupling was added to the hamiltonian to explain the colossal magnetotransport behavior, were some issues addressed experimentally. Most probably, the complex phase diagram of manganites is explained through an interplay between the electron-phonon coupling and the strong Hund coupling [102,106–108].

From a formal point of view, the hamiltonian of the system can be written as the sum of several contributions [110]

$$H = H_{\text{kin}} + H_{\text{Hund}} + H_{\text{AFM}} + H_{\text{el-ph}} + H_{\text{el-el}} \tag{2.12}$$

which are respectively the kinetic energy of the e_g electrons, the Hund coupling between the e_g and t_{2g} states, the Heisenberg antiferromagnetic coupling between nearest neighbours, the electron-phonon scattering and the electron-electron Coulomb interaction among the e_g electrons. An estimation of the parameters [111–119] finds that the largest contribution is given by the Coulomb repulsion; the Hund coupling is of the order of 1-2 eV, larger than the hopping term, of the order of fractions of electronvolts, and is responsible for the formation of high-spin states; the electron-phonon coupling is not negligible and has a large impact on the system properties and the antiferromagnetic coupling among the localized spins is of the order of

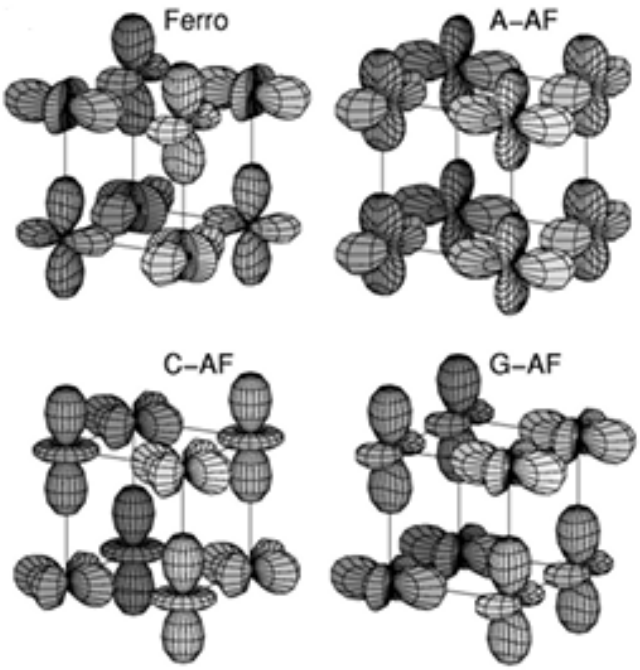

Figure 2.6: Orbital order for the different magnetic configurations [109].

tenths of electronvolts, but still large enough to determine the competition between antiferromagnetic and ferromagnetic ground state. The problem is challenging and requires some approximations in order to be solved: a possible solution is to ignore the Jahn-Teller and Coulomb interactions. This results in an oversimplified one-electron picture (so called one-orbital model) corresponding to the double exchange already discussed. Two other possible approaches are the Jahn-Teller phononic model and the Coulombic model, the former ignoring the electron-electron interactions and emphasizing the electron-phonon term, the latter introducing the Coulomb interaction between electrons and using mean-field approximations. Both models give similar results: the A-type and C-type antiferromagnetic order can be explained through orbital ordering, which could not be obtained in the one-orbital model. It is not surprising that, as a consequence of the Jahn-Teller distortion, which breaks the degeneracy of the e_g orbitals, the distortion of the octahedra leads to an orbital ordering which is in turn responsible for the magnetic configuration of the system. The orbital configuration for each magnetic state was determined by Hotta *et al.* [109] and is shown in Figure 2.6. It is worth noticing that at small Jahn-Teller distortions and for doping $x = 0$, it results in a ferromagnetic ground state with disordered orbitals [120], which could explain the tendency to develop ferromagnetic order in $LaMnO_3$. Furthermore, in thin films, the Jahn-Teller effect is sup-

pressed by the epitaxial strain, which naturally breaks the degeneracy of the e_g states to favour the $d_{x^2-y^2}$ or the $d_{3z^2-r^2}$ for tensile or compressive strain, respectively. The biaxial strain acts in a different way as compared to Jahn-Teller, and this could be another explanation for the appearance of a net ferromagnetic moment in thin $LaMnO_3$ films.

The magnetic phase diagram

The strong interplay between lattice, orbital, charge and spin order parameter is responsible for the rich magnetic behavior observed in the manganites, which is reflected in a complex phase diagram as a function of hole doping. Figure 2.5 shows the phase diagram for Ca, Sr and Ba-doped $LaMnO_3$. As already mentioned, the undoped system is (in its bulk form) antiferromagnetic, although when deposited as thin film it develops a net magnetic moment which origin is still controversial. $LaMnO_3$ is characterized by an insulating behavior in both bulk and thin films [49, 51, 121]. As we increase the hole doping, a transition to ferromagnetic conducting behavior is observed, which is associated to an isotropic orbital occupation and a disordered orbital state, where double exchange dominates the magnetic interaction mechanism. By increasing further the hole doping, a transition to G-type antiferromagnetism is observed, passing through the CE-type or A or C-type antiferromagnetism at half doping, depending on the divalent metal used to dope the system. At the other extreme of the phase diagram (i.e., $x = 1$), the system behaves as G-type antiferromagnet.

The magnetic behavior of the colossal magnetoresistance manganites is very rich and complex and, although they have been investigated for long time, a unified theory which could explain their physics is still missing. This fact highlights the interest in studying this system and understanding the physics of strongly correlated materials. Furthermore, the variety of the parameters that can be tuned in order to control their properties makes these systems very appealing for future technological applications.

2.3 Titanates and ferroelectricity

The titanates are another example of a system where the orbital configuration is of vital importance in determining their properties. The general formula $R_{1-x}A_xTiO_3$, where R and A are a trivalent and divalent earth, respectively, shows the Ti ion to be in mixed $3+/4+$ state. Differently from the case of manganites, the t_{2g} orbitals lie at the Fermi level and, despite the structural similarities, titanates show completely different properties, which are still not clearly understood; the compound $LaTiO_3$, for example, is an antiferromagnet whose spin and orbital alignment has still not been fully elucidated [122]. The physics of the titanates and the origin of their magnetic moment, although of fundamental interest to expand our knowledge of

orbital physics in transition metal oxides, is not investigated in this thesis. Nonetheless, titanates are employed as ferroelectric layers in multiferroic heterostructures and exploited in order to investigate the magnetoelectric coupling at the interface with manganite layers. Examples of ferroelectric titanates are $BaTiO_3$ or $Pb(Zr_{0.2}Ti_{0.8})O_3$; the former, used as ferroelectric layer in the heterostructures studied in this thesis, is considered the prototype of ferroelectrics and piezoelectrics, while the latter is of particular interest for technological applications such as FeRAMs, pressure and stress sensors, ultrasound generators, diesel engine injectors and many others. In order to introduce the physics of ferroelectrics, we will discuss here the properties of the $BaTiO_3$ system, which is the main focus of this section.

2.3.1 Origin of ferroelectricity

A ferroelectric is an insulating system with two stable states of non zero electric polarization in zero applied electric field [123]. It is vital that the ferroelectric polarization $\mathbf{P}$ can be switched between these stable states through the application of an electric field $\mathbf{E}$, which couples to the polarization as $-\mathbf{E} \cdot \mathbf{P}$. The switching of the polarization is generally understood in terms of growth and shrinking of ferroelectric domains, i.e., it does not happen in the single unit cell but it involves the whole material with a long range order. And it is just the long range order which plays a fundamental role in developing the macroscopic ferroelectric moment, given by the alignment of the microscopic ferroelectric moments in the single unit cells. In $BaTiO_3$, the electric dipole originates from a polar displacement of the atoms in the unit cell. In this particular case, an off-center displacement of the Ti atom in the octahedral environment leads to a deformation of the cubic structure to tetragonal. The ferroelectric moment can be calculated by knowing the displacement u and the Born effective charge Z^*e according to the relation $\mathbf{P} = \frac{1}{\Omega} \sum Z^* e u$, where Ω is the volume of the unit cell. Although ferroelectricity can only be present in crystals with a polar structure, in order to be ferroelectric, a material must allow the switching of the polarization with an applied electric field, giving rise to the ferroelectric hysteresis loop. This implies that not all polar crystal structures result in a ferroelectric material; generally, the presence of stable states is ensured when a small symmetry-breaking distorts the crystal from a high to a lower symmetry state, as is the case of the titanates. The application in devices requires high polarizations and coercive fields in order to have a stable moment at zero field.

Finite size effects

As mentioned before, the long range order is fundamental for the presence of a macroscopic ferroelectric moment. A natural question that arises is that of the effect of finite size in these materials, i.e., what is the ferroelectric re-

sponse to the reduction of the size of the material [124]. A sharp decrease of the Curie temperature is observed in $BaTiO_3$ nanowires when the diameter is decreased below 30 nm [125], while lamellae with thickness 250-300 nm show bulk-like Curie temperature [126]. In thin films, ab-initio calculations and experimental observations report a critical thickness of 2.4 nm for $BaTiO_3$, below which the film is no longer ferroelectric [127,128]. Given the importance of using ultrathin films in this research project, this is an important aspect to keep in consideration.

2.4 Magnetoelectric coupling in multiferroic heterostructures

The control of magnetism through an applied electric field is an interesting and stimulating topic due to the potential enormous impact on technological devices. Since the discovery of multiferroics, i.e., materials which simultaneously possess magnetic and ferroelectric properties, the investigation and understanding of the strong electron correlation responsible for the coupling of the two order parameters has progressed significantly. If we consider a system with two components, specifically, a magnetic and a ferroelectric component, the free energy can be expressed as a sum of the electric (P) and magnetic (M) induction, which can be written as [9,129,130]

$$\begin{aligned} P_{\mathrm{i}} &= P_{\mathrm{si}} + \epsilon_0 \sum_j \chi^{\mathrm{e}}_{\mathrm{ij}} E_{\mathrm{j}} + \frac{1}{\mu_0} \sum_j \alpha_{\mathrm{ij}} B_{\mathrm{j}} + ... \\ M_{\mathrm{i}} &= M_{\mathrm{si}} + \frac{1}{\mu_0} \sum_j \chi^{\mathrm{m}}_{\mathrm{ij}} B_{\mathrm{j}} + \frac{1}{\mu_0} \sum_j \alpha_{\mathrm{ji}} E_{\mathrm{j}} + ... \end{aligned} \tag{2.13}$$

where the first two terms in the sum correspond, respectively, to the spontaneous and induced polarization, the latter linearly dependent on the electric and magnetic susceptibility χ; the third is a cross-term induced by the magnetoelectric coupling, it shows that the coefficient α can be expressed as

$$\alpha_{\mathrm{ij}} = \mu_0 \frac{\partial P_{\mathrm{i}}}{\partial B_{\mathrm{j}}} = \frac{\mu_0 \partial M_{\mathrm{i}}}{\partial E_{\mathrm{j}}} \tag{2.14}$$

From the above expression can be shown that α is limited by the physical constraint $\alpha \leq \sqrt{\epsilon_0 \mu_0 \chi^{\mathrm{m}}_{\mathrm{ij}} \chi^{\mathrm{e}}_{\mathrm{ij}}}$ [131], in fact limiting the size of the linear magnetoelectric effect.

The field of multiferroics remains challenging and open questions are still present; only a small fraction of materials present multiferroic properties, and the coupling between ferroelectricity and magnetism is generally weak. A possible approach to solve this problem is to engineer artificial multiferroics, i.e., to employ thin films in a stacking sequence where ferroelectric and magnetic layers are alternated. This kind of structure is called

artificial multiferroic heterostructure, since the multiferroicity is artificially built by choosing the two materials. The heterosctructure can hence be optimized by selecting the materials with the desired properties, which in turn leads to an improvement of the coupling between the two order parameters. In artificial multiferroics, three main mechanisms are identified as mediators for the magnetoelectric coupling: strain, exchange and charge mediated effect [129, 132–137].

Strain-mediated magnetoelectric coupling

The strain-mediated mechanism relies on the piezoelectric and magnetostrictive or magnetoelastic effect to produce a ferroelectric response to an applied magnetic field (direct) or a magnetic response to the applied electric field (inverse), respectively. More specifically, in the direct coupling a magnetic field is applied to a multiferroic system, which contracts because of the magnetostrictive effect; the converse piezoresponse activated by the strain induced through the magnetic field in turn generates an electric response. The case of inverse coupling works in the opposite: as a response to an applied electric field, the piezoelectric effect induces a strain, in response to which the magnetostrictive effect produces a magnetic effect. It is evident that a strong elastic coupling is fundamental in order to achieve such a magnetoelectric coupling. Of particular technological interest is the inverse coupling, which was also proposed for memory devices exploiting the magnetostrictive effect [138–141].

Exchange-mediated magnetoelectric coupling

Many insulating $3d$ metal oxides show an antiferromagnetic or ferrimagnetic alignment of the spins mediated by the superexchange mechanism. This happens also in some multiferroic materials, where an electric polarization is linked to an antiferromagnetic spin alignment. Therefore, it is possible to exploit exchange bias to control the magnetic state of an adjacent ferromagnetic layer: if the temperature of the system is below the Curie and above the Néel temperature and the system is cooled to below the Néel temperature, the exchange interaction between the antiferromagnetic and ferromagnetic layers leads to a preferential direction of the interfacial antiferromagnetic spins, inducing a bias effect that leads to a shifting of the *M-H* hysteresis loop towards positive or negative magnetic fields [142]. Exchange-mediated magnetoelectric coupling was first observed in Cr_2O_3 [143, 144], where the application of an electric field resulted in a net magnetization whose direction was dependent on the direction of the electric field.

Charge-mediated magnetoelectric coupling

In strongly correlated systems, where charge, orbital and spin order parameters are strongly correlated, the control of the magnetic order can be achieved by modulating the charge density. This can be performed by engineering multiferroic heterostructures and adopting an approach similar to that of a field effect transistor: the surface bound charge of a ferroelectric layer and the charge screening from the magnetic layer leads to the accumulation or depletion of charge carriers at the interface depending on the direction of the ferroelectric polarization and the carrier type. The advantage with respect to traditional transistors is the density of carriers in strongly correlated oxides, which is $\sim 10^{21}$ cm^{-3}, resulting in a screening length of few angstroms. Interesting materials for these applications are the colossal magnetoresistance manganites, which exhibit a complex phase diagram with a rich magnetic behavior as a function of hole doping. In principle, by choosing x at the boundary between two competing magnetic ground states, the accumulation or depletion of holes does not only have the effect of changing the net spin at the interface as a consequence of the charge carrier density variation, but drives the interface to a different magnetic state by modifying the exchange interaction. Vaz *et al.* studied $Pb(Zr_{0.2}Ti_{0.8})O_3/La_{0.8}Sr_{0.2}MnO_3$ heterostructures with hard x-ray absorption spectroscopy and bulk magnetometry techniques, revealing a different spin organization at the ferroelectric/ferromagnetic interface when the system is switched between depletion and accumulation states [8, 145, 146]. First principle calculations on $BaTiO_3/La_{0.5}Sr_{0.5}MnO_3$ have shown that the magnetic reconstruction happens within the first two or three unit cells in proximity with the ferroelectric $BaTiO_3$, with a variation in the magnetic moment up to 7 μ_B per interfacial Mn atom [61]. Differently from the first two cases, in which the magnetoelectric coupling influences the whole film, the charge-mediated magnetoelectric coupling is an interfacial effect limited in depth by the Fermi screening length.

3
Experimental Techniques

In this chapter I provide an overview of the experimental techniques used in this project, not with the goal to treat the techniques exhaustively from a formal point of view (for which well specialized books are already available and suggested in the text) but to explain the peculiarities of the instruments and methods used in relation to this specific research project. Particular emphasis is given to the film deposition through oxide molecular beam epitaxy, which is at the basis of the experimental part.

3.1 Oxide Molecular Beam Epitaxy

The improvement in the deposition techniques brought by the technological progress has lead to an increased quality of the films, surfaces and interfaces during the last years, opening new scenarios and challenges focused on the implementation of surface and interfacial properties in technological applications. While on one hand commercial high quality substrates are today largely available, on the other hand, in-situ characterization techniques became more performing and user-friendly, allowing a perfect control of the surface quality and film thickness during the deposition of the film. Furthermore, the growth of laser science, bringing along more powerful lasers at a low cost, has played a fundamental role in the development and spread of laser deposition techniques. Indeed, as far as concerns oxide films, the main vapour evaporation methods used nowadays for high quality thin films deposition are molecular beam epitaxy (MBE), sputtering deposition and pulsed laser deposition (PLD). In the former (discussed in detail in section 3.1.1), the chemical elements are situated in separated crucibles and, when warmed up to the evaporation temperature, they evaporate in a controlled

environment, condensing onto the substrate surface. In the latter, the evaporation of the film occurs through a pulsed laser which, hitting a target with a well defined stoichiometry, evaporates the material onto the substrate. The high deposition rates, allowing a relatively quick growth of the films, and its simplicity, has lead to a huge development of PLD during the last years. Moreover, the versatility in changing the material by substituting the target without breaking the vacuum is fundamental in projects requiring several different materials. Furthermore, as far as concerns the deposition of oxides, the oxygen environment during the deposition is quite rich, reaching pressures of $\sim 10^{-1}$ mbar, compared to the typical $\sim 10^{-7}$ mbar of MBE. While on one side this allows a better oxygenation of the films, on the other hand it is a well established cause for point defects formation in the film. Indeed, mainly two parameters are responsible for their occurrence during the deposition: the particles' kinetic energy and the mean free path [147]. Techniques with high energy flux, such as PLD and sputtering, are susceptible to the formation of point defects caused by re-sputtering from the substrate surface or by the impact of the high energy beams with other components in the vacuum chamber, leading to the incorporation of impurities in the film [147–150]. The mean free path (λ) of the beam in the chamber plays a role in the formation of points defects. The expression [151]

$$\lambda = \frac{\mathrm{k_B}T}{\sqrt{2}\pi D^2 p} \tag{3.1}$$

where $\mathrm{k_B}$ is the Boltzmann constant, T is the temperature and D is the diameter of the atoms or molecules, states that the mean free path is inversely proportional to the pressure p. Therefore, a higher pressure during the deposition leads to the interaction of the evaporating beam with the environment, which could produce undesired oxides and, consequently, deposit point defects on the surface. Despite the increasing importance of PLD for research and application purposes, the low oxygen partial pressure and kinetic energy of the evaporating beam in MBE, combined with the ability to change the film stoichiometry by controlling the evaporation rates, make MBE a unique tool for the growth of thin films and oxides heterostructures. The optimal quality of the films obtained, the possibility of using characterization techniques in real time during the deposition (such as reflection high energy electron diffraction), as well as the ability to change the stoichiometry of the films and explore the phase diagram of complex oxides, are the main advantages in its usage for film deposition in this research project.

3.1.1 Elements of molecular beam epitaxy

Molecular beam epitaxy is a deposition technique which allows epitaxial deposition of atomic or molecular beams onto the substrate surface. The beam is obtained by thermal heating of the elements situated in crucibles,

which evaporate above a certain temperature and, reacting with the oxygen present in the environment, deposit on the substrate. If the deposited film has the same crystalline orientation of the substrate and the same in-plane lattice parameter, the film is said to be epitaxial and fully strained. In order to reduce the number of contaminants in the chamber, low base pressures, of the order of 10^{-10} mbar, are required.

Thermal-evaporation cells and flow measurement

For simplicity, we consider here the case of Knudsen cells, i.e., we assume that the vapour and solid are in equilibrium [152,153], following the approach from [151]. In this approximation, we can write the evaporation flux Φ of the substance from an aperture A according to the Knudsen and Langmuir's theories of evaporation:

$$\Phi = Ap(T)\left(\frac{\mathrm{N_A}}{2\pi M k_\mathrm{B} T}\right)^{1/2} \tag{3.2}$$

where $\mathrm{N_A}$, M, k_B and T are the Avogadro's constant, the molecular mass of the element, the Boltzmann's constant and the temperature of the element, respectively. $p(T)$ is the equilibrium pressure in the crucible. At a given point P on the substrate at a distance r_P from the aperture of the crucible, the flow Φ_P of the evaporant will depend on the angles θ and φ defined in Figure 3.1(a) according to

$$\Phi_\mathrm{P} = \frac{\Phi}{\pi}\frac{1}{{r_\mathrm{P}}^2}\cos(\theta)\cos(\theta+\varphi) \tag{3.3}$$

Equation 3.3 describes the dependence of the flow from the solid angle defined by θ and φ. Therefore, if an MBE is equipped with several crucibles, it is important that the substrate position is exactly at the cross-point of all the evaporating beams of the different species, in order to obtain spacial homogeneity in a film which contains more than one element. Some deposition systems are equipped with a rotating plate which allows homogeneity of the film during the deposition. The main drawback of this approach is that characterization techniques such as reflection high energy electron diffraction cannot be used during the deposition. Equation 3.3 holds in the case of perfect crucibles with small apertures, while the real flow strongly depends on geometric factors which are not straightforward to consider. Therefore, the calculation of the evaporation rate has to be performed with other methods. Two common approaches use a quartz crystal microbalance or mass spectrometer, the latter allowing one to monitor of the evaporation rates during the deposition of the film.

Choice of the substrate

The substrate plays a vital role in the quality and properties of the films. The most important properties to take into account in order to deposit epitaxial films are the crystal symmetry and the in-plane lattice constant. Epitaxial growth occurs only if the difference between the substrate and film lattice parameter (mismatch) is within a few percent. The mismatch is defined as [154]

$$\varepsilon = \frac{a_{\text{film}} - a_{\text{substrate}}}{a_{\text{substrate}}} \tag{3.4}$$

where a is the in-plane lattice constant. If ε is positive (negative), the film is in compressive (tensile) strain state. If ε is too large, the film may not grow fully strained but relaxes through the onset of misfit dislocations or may not grow epitaxially at all. As we will see in the course of the thesis and already mentioned in chapter 2, strain plays a fundamental role in the properties of thin films and is one of the important parameters that affects the magnetic and electric properties of the manganites. In some cases, also the electrostatic repulsion between the atomic layers is considered when choosing the substrate. Let us consider as an example two substrates: $SrTiO_3$ and $LaAlO_3$; the former consists of a stacking sequence of SrO and TiO_2 planes. The total charge of each plane is zero (O contributes with -2, Ti with +4 and Sr with +2 according to simple chemical rules) and it is therefore a non-polar crystal. The latter is instead divided in LaO and AlO_2 consequent planes, having net charges of +1 and -1, respectively; the crystal is said to be polar. When a polar film is grown on a non-polar substrate (or vice versa), the disruption of the polarity at the interface between different materials modifies as well the properties of the film, bringing the so-called polar catastrophe.

Growth modes

The lattice mismatch is not the only parameter which influences the growth process: an important role is played by the film and substrate free energies. Let us consider the deposition of a film A on a substrate B. If the components in the gas state and the film surface are in equilibrium, the total free energy can be written as [155]

$$\Delta\gamma = \gamma_{\text{A}} + \gamma_{\text{i}} - \gamma_{\text{B}} \tag{3.5}$$

where γ_{A} and γ_{B} are the surface free energy of A and B and γ_{i} is the interfacial free energy, which contains the strain energy and the interactions between the two layers at the interface. If the quantity defined in equation 3.5 is negative, i.e., if the substrate energy exceeds $\gamma_{\text{A}} + \gamma_{\text{i}}$, layer-by-layer growth (also called Frank-van der Merwe) will occur. In this case, the film will complete the deposition of one layer before the growth of the new layer starts (Figure 3.1(b) shows a schematic of the growth processes). When

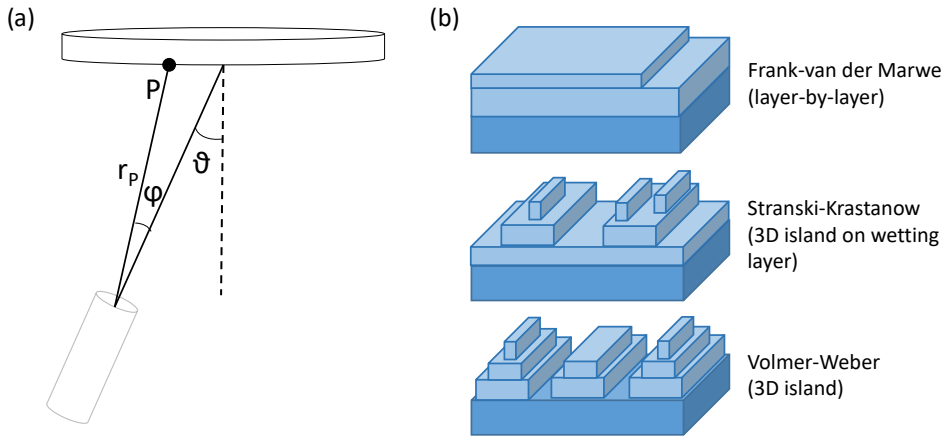

Figure 3.1: (a) Representation of the evaporation geometry in MBE. (b) Sketch of the three main growth processes.

the film thickness is increased, γ_i increases linearly. This defines a critical thickness after which $\Delta\gamma$ becomes positive, and the nucleation of 3D islands appears on the top of the layer-by-layer section (in this case, the growth mode is called Stranski-Krastanow or 3D island on wetting layer). Alternatively, in the case where γ_A is greater than γ_B, the growth is 3D-kind from the first stages of the deposition. In this case it is called Volmer-Weber or 3D island. Obviously, in the case of zero lattice mismatch (i.e., $\gamma_i \sim 0$), the growth process depends entirely on the substrate and film free energies. An interesting consequence of these considerations is the importance, when growing heterostructures, of choosing the correct order of the staking layers. Indeed, if $\Delta\gamma < 0$ for A/B stacking layers, it will necessary be $\Delta\gamma > 0$ for the B/A configuration, unless surfactants are used to reduce the surface energy [156].

3.1.2 Reflection high energy electron diffraction

Reflection high energy electron diffraction (RHEED) is a powerful technique for the characterization of the surface quality during the film deposition. A typical RHEED setup is shown in Figure 3.2(a): an electron gun shoots an electron beam with energies in the range 10-30 keV towards the sample surface with a low angle of incidence; the electrons are diffracted by the sample surface and hit a fluorescent screen; the diffraction pattern is hence collected by a camera. The main characteristics are the limited mean free path of the electrons in a solid and the small angle of incidence, of the order of few degrees, which make RHEED a very surface sensitive technique. The main advantage of this technique when compared to low energy electron diffraction (LEED) is its geometry: while in the latter the electrons hit the

sample with an angle of 90° with respect to the surface, in RHEED the angle of incidence is very small. This allows one to monitor the surface quality in real time during the deposition of the film, which is not possible with LEED since the detection system and the electron gun have to be perpendicular to the surface and would obstruct the molecular flow. The RHEED pattern reflects the crystallinity and quality of the surface and can qualitatively be discussed in terms of the Ewald construction. Let us consider an electron beam coming out of the electron gun with wavevector $\boldsymbol{k}_0$ and only elastic scattering. The reflected electron beams indicated in Figure 3.2(a) as $\boldsymbol{k}_1$ and $\boldsymbol{k}_2$ have the same modulus as $\boldsymbol{k}_0$; the three vectors are three different radii of the same sphere, called Ewald sphere. We now consider for simplicity a 1D chain of atoms aligned along the direction of propagation of the electron beam. The Fourier transform in the reciprocal space is a set of planes; the intersections between the planes and the Ewald sphere consists of concentric circles, denominated Laue zones. If we now consider a 2D arrangement of atoms, for example a square lattice, the Fourier transform is given by the planes just described and the corresponding planes rotated by 90 degrees. The intersection between these planes gives a series of rods which, intersecting the Ewald sphere, give rise to a series of spots lying on concentric circles corresponding to the different Laue zones (Figure 3.2(c), example a). The main spots will lay on the 0^{th} zone, the secondary in the 1^{st} zone and so on. If the surface is not smooth or the atoms are not well ordered, the RHEED pattern deviates from the geometry just described, the reciprocal rods assume complicated shapes which will be reflected in the RHEED pattern by the appearance of stripes, double dots and, in the case of a 3D surface, a transmission-like pattern [Figure 3.2(c)]. In some cases, an indication of the inelastic scattering can appear in the RHEED pattern, manifesting through the so-called Kikuchi lines [157]. They appear along the radial direction and connect different Laue zones; in proximity of these lines higher brilliance spots can be observed. Figure 3.2(b) shows an example of a RHEED pattern for a Si(111) crystal, where the RHEED spots as well as Kikuchi lines are visible. The quality of the surface is reflected also by the Kikuchi lines, which appear sharp and well defined in the case of perfect crystal structure and surface, while they are broaden and diffuse when the surface becomes more rough.

RHEED intensity oscillations

RHEED is not only a useful tool to judge the quality of the surface before, during and after the deposition, but it also allows one, when the growth occurs layer-by-layer in the 2D islands mode, to monitor the film thickness and the evaporation rates during the deposition. Indeed, reflecting the smoothness of the surface, the intensity of the RHEED spots oscillates during the deposition as schematically shown in Figure 3.2(d): the maximum of the

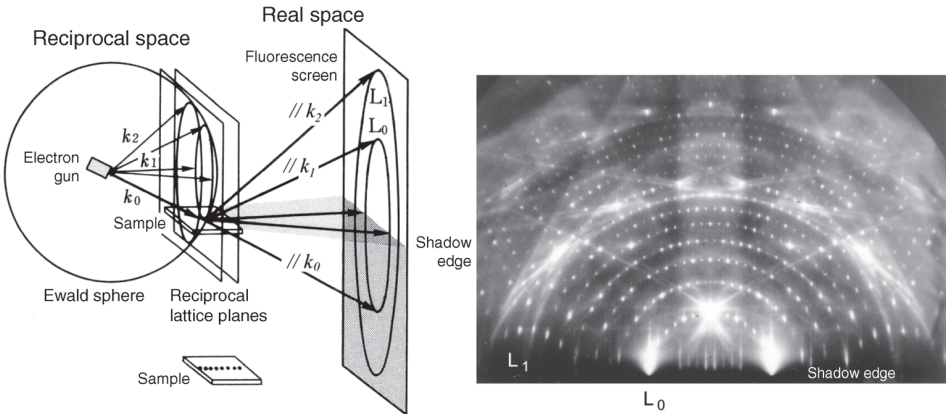

(a) *RHEED geometry* (b) *RHEED pattern of a Si(111)*

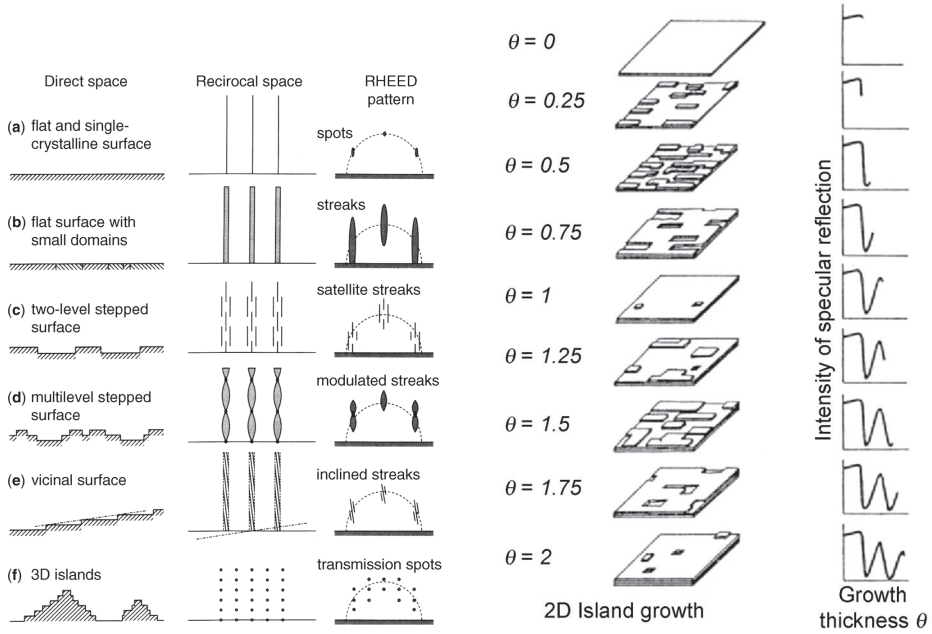

(c) *Examples of patterns* (d) *Intensity oscillations*

Figure 3.2: (a) Schematic of the RHEED scattering geometry, showing the electron wavevectors $\boldsymbol{k}_0$, $\boldsymbol{k}_1$ and $\boldsymbol{k}_2$ and the Ewald sphere. (b) Example of a RHEED pattern from Si(111), where Kikuchi lines are visible. (c) Schematic of the RHEED patterns based on the quality of the surface, from a flat surface, (a) for which the RHEED pattern shows well defined spots lying on an arch, to a rough surface (f) where a bulk-like diffraction pattern can be observed. (d) Graphical explanation of the layer-by-layer growth process and its correlation with the RHEED intensity oscillations. Figure adapted from [158].

RHEED intensity is found when the sample presents a perfect atomically smooth surface. During the deposition of one monolayer, the surface becomes rough and small islands grow on it, resulting in a lower intensity of the RHEED spots. The RHEED intensity reaches its minimum once half of the monolayer is evaporated to the surface. After that point, the islands converge again into a smooth surface, resulting in the increasing of the RHEED intensity up to a new maximum, when again an atomically smooth surface reconstruction occurs. Within this picture, each maximum of the RHEED intensity corresponds to the complete deposition of one monolayer, allowing a perfect control over the film thickness at an atomic level. In some cases, the behavior of the RHEED intensity oscillations can be used as a probe to understanding the growth mechanism and can be important to optimize the growth parameters.

3.1.3 Chamber calibration and sample growth

The oxide molecular beam epitaxy chamber used in this project is equipped with a RHEED system, a load-lock chamber for the sample transfer and 5 effusion cells, filled with Mn, Ti, Sr, La and Ba. In order to deposit the films, the MBE chamber has to be calibrated and the correct parameters have to be set for proper growth. The evaporation rates of the metals in the crucibles are measured through a quartz crystal microbalance (QCM): the quartz crystal oscillates with a typical resonance frequency of 10 MHz. As soon as a material deposits on its surface, the quartz oscillation frequency decreases when the mass increases. Thus, the relative variation in the crystal resonance frequency is directly proportional to the mass of the substance evaporating and gives the deposition rate in Å/min. In principle, the QCM is inserted at the same height where the substrate is held during the film deposition. However, slight changes between the deposited rates and the one measured by the QCM may occur. In order to calibrate the QCM for such differences, two films containing all the elements in the crucibles were initially grown (namely, $La_{0.5}Sr_{0.5}MnO_3$ and $BaTiO_3$) on a Si substrate held at room temperature during the deposition. Rutherford backscattering (RBS) measurements[1] were performed on these two films in order to obtain the actual stoichiometry. By knowing the expected (QCM) and the actual (RBS) stoichiometry, one could calculate the tooling factors as follows

$$T = T_{\mathrm{i}} \times \frac{C_{\mathrm{RBS}}}{C_{\mathrm{QCM}}} \tag{3.6}$$

Where T and T_i are respectively the new and old tooling factors, i.e., the correction to the measured evaporation rates, and C_{RBS} and C_{QCM} the stoichiometric factors as measured by RBS and QCM, respectively. Once the

[1] The RBS measurements were performed at ETH Zürich-Ion Beam Physics by Max Doebeli.

calibration of the QCM is performed, it is of fundamental importance to find the correct growth parameters in order to grow epitaxial films. The important parameters in MBE are three:

(i) The substrate temperature during the deposition (T_S)

(ii) The oxygen partial pressure (P_{O_2})

(iii) The evaporation rates.

After several attempts, in which the quality of the films is judged by the RHEED pattern and oscillations, atomic force microscopy measurements and x-ray fluorescence spectroscopy,[2] the optimal parameters were found for titanates and manganites films as summarized in Table 3.1. If not differently specified, these are the parameters used for the samples grown in this project.

Prior to the deposition, the substrates are prepared with different recipes according to their nature. The quality of the substrate surface is indeed of vital importance in surface and interface science. In particular, in order to promote the growth of smooth and high quality films, the $SrTiO_3$ substrates are chemically etched in a HCl:HNO_3 solution and annealed at 1000 °C in air for 1 h to obtain single TiO_2-terminated surface [159, 160]. The LSAT substrates are instead annealed at 1200 °C for 1 h in a tube furnace, with a $LaAlO_3$ substrate in proximity of the LSAT surface. During the annealing, the $LaAlO_3$ increases the La vapour pressure, avoiding the formation of SrO mounds during the surface reconstruction process and giving a single terminated surface [161]. If not differently specified, the samples are post annealed in air or under O_2 flow at 600 °C for 6 h to allow full oxygenation of the film.

Table 3.1: List of growth parameters used in the film deposition throughout this project. One unit cell (uc) typically corresponds to ~ 4 Å.

Sample	T_S	P_{O_2}	Deposition rates
Manganites	720 °C	5.0×10^{-7} mbar	0.5 uc/min
Titanates	680 °C	4.0×10^{-7} mbar	0.5 uc/min

3.2 Interaction of light with matter

Let us consider an electromagnetic wave which interacts with a solid. The intensity of the incoming wave I_0 decays exponentially inside the material as a function of the thickness t, according to the law

$$I = I_0 e^{-\mu t} \tag{3.7}$$

[2] The measurements have been performed at the microXAS beamline at SLS (PSI) with the help of Dario F. Sanchez.

where μ us the absorption coefficient of the material. When an electron absorbs the beam, two different scenarios can take place: either the electron is photoemitted into the continuum or is excited to an empty orbital level. In the latter case, the relaxation process may occur in three main different mechanisms: emission of a photon (fluorescence), emission of an electron (Auger electrons) or formation of secondary electrons. All these processes can be detected: the detection of photons is generally performed through a photodiode. The mean free path of a photon in a solid is grater than that of the electron, meaning that fluorescence experiments are more bulk sensitive than the electron-based ones. Secondary electrons, created from the scattering of primary electrons and photons with other electrons, possess kinetic energies lower than 50 eV [162] and can be distinguished from the photoemitted and Auger electrons, characterized by higher kinetic energies. Since when using soft x-rays the absorption coefficient cannot be measured in transmission mode, except if the sample is very thin (like in the case of free standing films or membranes), the fluorescence signal (fluorescence yield) or the secondary electrons (electron yield) are measured. From a formal point of view, the problem is generally discussed in a semiclassical approach: the light is treated classically as an electromagnetic wave, described in terms of the vector potential $\mathbf{A}$ [163], while the electron is treated by quantum-mechanics. The absorption coefficient is directly proportional to the differential cross-section, which describes the number of transitions occurring per unit time over a solid angle $\mathrm{d}\Omega$, defined as [80]

$$\frac{\mathrm{d}\sigma}{\mathrm{d}\Omega} = \frac{\omega_{\mathrm{i}\to\mathrm{f}}}{\Phi_0 \mathrm{d}\Omega} \tag{3.8}$$

where $\omega_{\mathrm{i}\to\mathrm{f}}$ is the probability that an electron in the solid absorbs a photon and is excited from an initial i to a final state f and Φ_0 is the incoming photon flux. The Fermi golden rule expresses $\omega_{\mathrm{i}\to\mathrm{f}}$ in terms of the interaction hamiltonian H_{int}:

$$\omega_{\mathrm{i}\to\mathrm{f}} = \frac{2\pi}{\hbar} \left| \left\langle \psi_{\mathrm{f}}^{\mathrm{N}} \middle| H_{\mathrm{int}} \middle| \psi_{\mathrm{i}}^{\mathrm{N}} \right\rangle \right|^2 \delta(E_{\mathrm{f}}^{\mathrm{N}} - E_{\mathrm{i}}^{\mathrm{N}} - h\nu) \tag{3.9}$$

where $\psi_{\mathrm{i}}^{\mathrm{N}}$ is the initial N-electron ground state wavefunction, $\psi_{\mathrm{f}}^{\mathrm{N}}$ is the final state, $E_{\mathrm{i}}^{\mathrm{N}}$, $E_{\mathrm{f}}^{\mathrm{N}}$ and $h\nu$ are the initial and final energies of the N-electron system and the energy of the photon, respectively. H_{int} is given by

$$H_{\mathrm{int}} = -\frac{\mathrm{e}}{2mc}\mathbf{A}\cdot\mathbf{p} \tag{3.10}$$

The problem can be simplified in the Born-Oppenheimer approximation, where we factorize the wavefunction in two parts: a one-electron term and the (N-1) electrons term

$$\psi_{\mathrm{f}}^{\mathrm{N}} = C\phi_{\mathrm{f}}^{\mathbf{k}}\psi_{\mathrm{f}}^{\mathrm{N}-1} \tag{3.11}$$

where $\phi_{\mathrm{f}}^{\mathbf{k}}$ is the wave function of the photoelectron with wavevector $\mathbf{k}$ and C is an operator which antisymmetrizes the total wavefunction according to the Pauli exclusion principle. Within this approximation, the matrix element can be written as

$$M_{i\to f}^{\mathbf{k}} = \left\langle \psi_{\mathrm{f}}^{\mathrm{N}} \middle| H_{\mathrm{int}} \middle| \psi_{\mathrm{i}}^{\mathrm{N}} \right\rangle = \left\langle \phi_{\mathrm{f}}^{\mathbf{k}} \middle| H_{\mathrm{int}} \middle| \phi_{\mathrm{i}}^{\mathbf{k}} \right\rangle \left\langle \psi_{\mathrm{f}}^{\mathrm{N}-1} \middle| \psi_{\mathrm{i}}^{\mathrm{N}-1} \right\rangle \tag{3.12}$$

If we consider the commutation relations $\hbar\boldsymbol{k}/m = -\mathrm{i}[\boldsymbol{r}, H]$ we can write

$$\left| M_{i\to f}^{\boldsymbol{k}} \right|^2 = \left| \left\langle \phi_{\mathrm{f}}^{\boldsymbol{k}} \middle| \boldsymbol{\epsilon} \cdot \boldsymbol{r} \middle| \phi_{\mathrm{i}}^{\boldsymbol{k}} \right\rangle \right|^2 \tag{3.13}$$

where $\boldsymbol{\epsilon}$ and $\boldsymbol{r}$ are the light polarization vector and the electron position operator, respectively. In equation 3.13, we have assumed the *dipole approximation*: the wavelenght of the electromagnetic wave is longer than the atomic shell radius. The electronic wave function can be factorized in three terms: a radial part ($|R_{n,l}(r)\rangle$), an angular part ($Y_{l,m_l} = |l, m_l\rangle$) and a spin component ($\chi_{s,m_s} = |s, m_s\rangle$). The dipole operator $P = \boldsymbol{\epsilon}\cdot\mathbf{r}$ acts on the three different components separately:

$$\left\langle \phi_{\mathrm{f}}^{\boldsymbol{k}} \middle| P \middle| \phi_{\mathrm{i}}^{\mathbf{k}} \right\rangle = \delta(m_s' - m_s) \left\langle R_{n',l'}(r) \middle| \boldsymbol{r} \middle| R_{n,l}(r) \right\rangle \left\langle Y_{l',m_l'} \middle| P/r \middle| Y_{l,m_l} \right\rangle \tag{3.14}$$

The radial part of this equation gives the element selectivity of x-ray absorption. The spin and orbital part, instead, are responsible for the *dipole selection rules*, which establish the allowed electronic transitions in the dipole approximation:

$$\begin{aligned} &\Delta l = \pm 1 \\ &\Delta m_l = 0, \pm 1 \\ &\Delta s = \Delta m_s = 0 \end{aligned} \tag{3.15}$$

3.3 X-ray absorption spectroscopy: linear and circular dichroism

In an x-ray absorption spectroscopy (XAS) measurement, a photon with energy $h\nu$ is absorbed by a core electron, which is photoexcited to an empty orbital state above the Fermi level. Here, our focus will be on soft x-ray absorption spectroscopy, characterized by photon energies in the range 100-2000 eV, and on the dichroic effects that arise when polarized light is involved in the absorption process. As we have seen in the previous section, the probability that a photon is absorbed by a solid is directly proportional to the matrix elements described in equation 3.13, where the term $\boldsymbol{\epsilon}\cdot\boldsymbol{r}$ is called dipole operator. The polarization vector $\boldsymbol{\epsilon}$ can then be expressed as follows:

for *linearly polarized light*, if we suppose that the x-ray wavevector $\boldsymbol{k}$ is along the direction z, we can have one of the two polarizations

$$\epsilon_x = \begin{pmatrix} 1 \\ 0 \\ 0 \end{pmatrix} \quad \epsilon_y = \begin{pmatrix} 0 \\ 1 \\ 0 \end{pmatrix}$$

Circularly polarized light can be written as a linear combination of two linearly polarized components, separated by a phase shift of $\pi/2$: for a light beam propagating along the z direction

$$\epsilon_z^{\pm} = -\frac{1}{\sqrt{2}}(\epsilon_x + \mathrm{e}^{\pm \mathrm{i}\frac{\pi}{2}}\epsilon_y) = -\frac{1}{\sqrt{2}}(\epsilon_x \pm \mathrm{i}\epsilon_y)$$

or, in matricial notation

$$\epsilon_z^{+} = -\frac{1}{\sqrt{2}} \begin{pmatrix} 1 \\ \mathrm{i} \\ 0 \end{pmatrix} \quad \epsilon_z^{-} = -\frac{1}{\sqrt{2}} \begin{pmatrix} -1 \\ \mathrm{i} \\ 0 \end{pmatrix}$$

Since the matrix elements defined in equation 3.13 depend on the scalar product between the light polarization vector and the electron position operator, the absorption process depends on the polarization of the light. If the difference between two absorption spectra collected with different light polarizations is non zero, then a dichroism effect is observed.

X-ray magnetic circular dichroism

The description below is based on [80]. The intensity I of a XAS is generally dependent on the number of holes N_h available in the final orbital

$$I = CN_\mathrm{h} \tag{3.16}$$

hence, x-ray spectroscopy gives information on the empty density of states. In the particular case of a transition metal, the absorption intensities at the L_3 and L_2 edges are directly proportional to the number of available d states above the Fermi level. Magnetism is probed by making the process spin-dependent, i.e., by using circularly polarized light and exploiting x-ray magnetic circular dichroism (XMCD): the absorption spectra are collected with two opposite circular polarizations of the incoming photon beam; the normalized difference between the two spectra gives the magnetic circular dichroism, which is non zero if the sample has a net magnetic moment along the direction of propagation of the beam. Let us consider a ferromagnetic sample: the d shell is partially filled with electrons whose spins are aligned in parallel. The probability of a transition from the $p_{1/2}$ or $p_{3/2}$ to the empty

d orbital is given by the matrix element defined in equation 3.13, where the interaction matrix is the angular part of the dipole operator

$$\left| \langle d_n, m_s | \frac{P_z^q}{r} | p_j, m_j \rangle \right|^2 . \tag{3.17}$$

Here the index $n = 1, ..., 5$, $m_s = \pm 1/2$, $j = 3/2, 1/2$ and $m_j = \pm 3/2, \pm 1/2$; q is the photon spin. With simple calculations, using the Clebsch-Gordan tabulated values, it is possible to obtain the probability of each allowed transition. In particular, in the absence of spin-orbit coupling, the L_3 and L_2 edges show a dichroic effect which is equal in magnitude but reversed in sign: an x-ray with positive photon spin ($q = +1$) excites more spin up electrons at the L_3 edge then the x-ray with reverse photon spin ($q = -1$); the opposite is found at the L_2 edge.

The XMCD process is described by a simplified two-step model [80]: in a first step, the photon transfers its angular momentum to the electron which is excited after the absorption. If the electron is in a spin-orbit split state (as is the case of $p_{3/2}$ and $p_{1/2}$) the polarization of the photon is in part transferred to the electron through the spin-orbit coupling, which is opposite at the L_3 and L_2 edges (where the spin-orbit coupling is $l + s$ and $l - s$, respectively), resulting in an opposite spin polarization at the two edges. In the second step, the different spin valence shell population (which is naturally found in a magnetic material) is responsible for the difference in the absorption signal: if we consider the extreme case of a half-filled d shell, only electrons with one spin can be excited (the dipole selection rules 3.15 do not allow spin-flips); if the outer shell is filled equally with both spins, the dichroic signal vanishes, as expected for a non magnetic material. In materials where a strong contribution comes from the orbital moment, the XMCD signal at the two edges is not the same in magnitude; the effect of the orbital moment is to make the total integral of the XMCD different from zero.

XMCD sum rules

Since the XMCD shape strongly depends on the orbital and spin magnetic moment, as we mentioned before, it is possible to extract the spin (m_{spin}) and orbital (m_{orb}) contribution to the total magnetic moment. The XMCD sum rules allow one to determine the two contributions according to the relations [164–166]

$$\begin{aligned} m_{\text{orb}} &= -\frac{4}{3} \frac{\int_{L_3+L_2} (\mu_+ - \mu_-) \mathrm{d}\omega}{\int_{L_3+L_2} (\mu_+ + \mu_-) \mathrm{d}\omega} (10 - n_{3d}) \\ m_{\text{spin}} &= -\frac{6 \int_{L_3} (\mu_+ - \mu_-) \mathrm{d}\omega - 4 \int_{L_2} (\mu_+ - \mu_-) \mathrm{d}\omega}{\int_{L_3+L_2} (\mu_+ + \mu_-) \mathrm{d}\omega} (10 - n_{3d}) \left(1 + \frac{7 \langle T_z \rangle}{2 \langle S_z \rangle} \right)^{-1} \end{aligned} \tag{3.18}$$

where μ_+ and μ_- are the XAS spectra collected with circular plus and minus light polarization, respectively, and $\langle T_z \rangle$ and $\langle S_z \rangle$ are the magnetic dipole operator and spin moment expectation values, respectively. In the case of manganites, $\langle T_z \rangle$ can be neglected because of the orthorhombic environment [166]. $(10 - n_{3d})$ is the number of holes of the probed element.

As originally formulated, the sum rules require well distinct absorption edges in order to determine the spin magnetic moment. The overlap of the two edges brings an underestimation of the spin moment, which has to be corrected by multiplying with specific correction factors [167]. In the case of manganites, the spin moment is multiplied by 1.5.

X-ray linear dichroism

In order to understand the origin of the linear dichroic effect, let's first consider the simplest case of $s \rightarrow p$ transitions using once again the matrix element in equation 3.13:

$$\langle 3p|\boldsymbol{\epsilon} \cdot \boldsymbol{r}|2s\rangle$$

For simplicity, we assume that the sample is not magnetic. The absorbing electron can perform three allowed transitions from the s orbital to one of the three p orbitals. If no charge anisotropy is present, the probability of each transition is the same and equals $1/3$. If, otherwise, charge anisotropy modifies the shape of the lobes (as in the case of Jan-Teller distortion or strained films, for example) the probability of the three transitions is not the same but depends on geometrical factors. As an example, we consider a material with a cubic unit cell and the light polarization vector along one of the crystallographic axis. In its bulk form, if no distortion occurs, no linear dichroic effect is present, or, in other words, the absorption spectra collected with different light polarizations are the same. If the material is instead grown as thin film form under epitaxial strain by the substrate (i.e., the in-plane lattice parameter becomes different than the out-of-plane), a dichroic effect emerges. In the experimental geometry depicted in Figure 3.3(a) the two polarizations of the x-rays probe predominantly the in-plane and out-of-plane orbitals, respectively. Since the lattice distortion leads a charge anisotropy, the absorption spectra collected with the two different polarizations is not the same and a x-ray linear dichroism (XLD) is observed, as shown in Figure 3.3(b). In the case of p to d transitions the discussion becomes more complicated, since both orbitals are not spherically symmetric. The number of allowed transitions are 15 (3 p orbitals $\times$ 5 d orbitals) and the probability of each transition is not the same because of the different shapes of the d orbitals, as shown in Figure 3.3(c). In a real experiment, it is impossible to obtain linearly polarized light which is exactly parallel to the out-of-plane lattice parameter, since it would require an angle of incidence of 0 degrees. As a consequence, a small component of the light beam is present along the in-plane direction, and it becomes necessary to correct the spectra

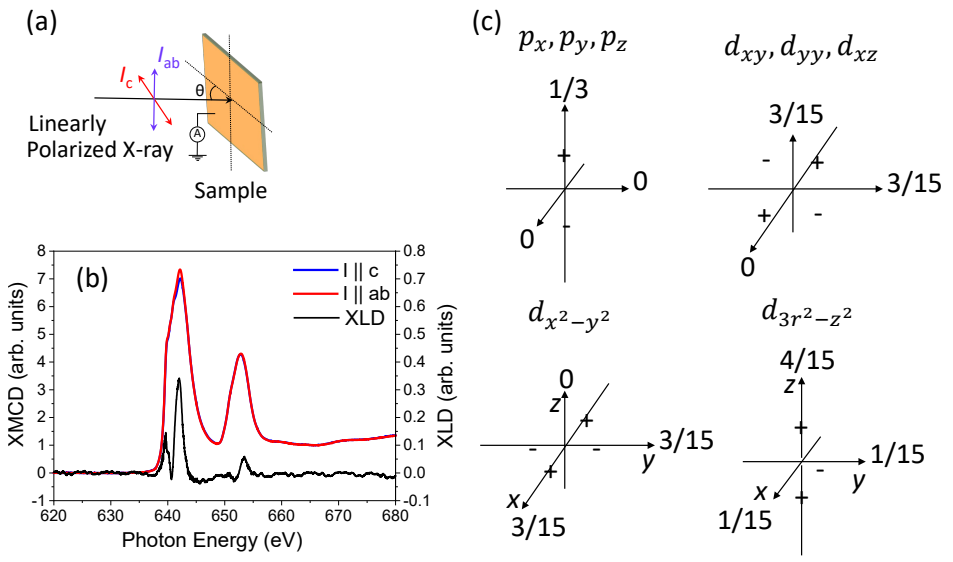

Figure 3.3: (a) Example of the experimental geometry in a XLD experiment. (b) Example of an absorption spectra with linearly polarized light and the corresponding XLD at the Mn L-edge. (c) Transition probabilities from an s to a p orbital (top-left) and from a p to a d orbital (adapted from [80]).

for the angle of incidence used. The angle dependence of the intensity is given by

$$I(\theta) = I_{\parallel} \cos^2\theta + I_{\perp} \sin^2\theta \tag{3.19}$$

from which the perpendicular component can be extracted. The dichroism effect discussed above is generally named "natural", to distinguish it from the magnetic linear dichroism. Indeed, the problem becomes more complicated in the case of a magnetic sample: when the spins are aligned by an exchange interaction, the spin-orbit coupling distorts the charge distribution and contributes to the linear dichroic signal. Indeed, linear dichroism is often used as a probe for antiferromagnetism, although in these cases the disentanglement of the natural and the magnetic dichroism is generally quite challenging. A possible approach is to perform a temperature dependence study, collecting XLD spectra above and below the magnetic transition temperature. In the former case, the magnetic contribution vanishes, while in the latter case both charge anisotropy and magnetic contributions are present.

3.4 X-ray photoemission electron microscopy

X-ray photoemission electron microscopy (XPEEM) combines the advantages of a photoemission microscope with the XMCD or XLD effects arising from polarized x-rays, providing an important tool for the study of magnetic

systems and surfaces. Generally, fully polarized synchrotron light is delivered to the sample which, as a consequence of the absorption process described in section 3.2, emits secondary electrons. These electrons pass through by a series of magnetic lenses which magnifies the electron beam onto a 2D detector [Figure 3.4(a)]. In order to obtain a sharp image, it is necessary to reduce the angular acceptance of the electrons, which is achieved by introducing a pin hole aperture, named contrast aperture. Therefore, a high lateral resolution is obtained at the expense of the intensity.

Data collection and analysis

In principle, with XPEEM it is possible to collect different kinds of data according to the goal of the project. Here, I summarize the principal use made of this technique for the research project explained here, referring to more specialized books for a comprehensive description of this technique [168–170]:

- *Elemental contrast images.* This is a powerful method to highlight the elemental composition of the sample with high spatial resolution. By probing the sample with the photon energy tuned at the edge and at the pre-edge of a selected element, it is possible to check the areas where it is present, which appear as a bright signal in the image; the division of the two images obtained at the edge and pre-edge gives the elemental contrast. It is particularly useful to imaging nanoparticles deposited on a substrate or if one wants to understand particular features arising in the sample (which may arise due to segregation, for example)

- *X-ray absorption spectra.* Here, two series of images are collected with different light polarization as a function of the photon energy, each image corresponding to one energy step. This approach allows one to probe linear or circular dichroism. In principle, the data analysis in PEEM could follow the one used in conventional absorption spectroscopy: after aligning all the images, the normalized difference of the two series obtained with different polarization gives the dichroism spectra. The only difference is that, for each polarization, there are, in principle, as many absorption spectra as the number of pixels, and hence the spatial resolution allows one to extract space-resolved information on the magnetic domains.

- *Magnetic contrast image.* Generally, magnetic contrast images are collected in order to get information on the magnetic state at the sample surface: at a fixed energy, where the XMCD or XLD signal is maximum, two images with opposite polarization are acquired. We focus on the circular dichroism (the analysis is analogous in the case of XLD images) and we write I^+ and I^- as the images collected with circular

plus and minus polarization, respectively. The quantity $^{I^+-I^-}/_{I^++I^-}$ is a contrast image. The different contrasts in this image reflect the different magnetic states at the sample surface. In the example shown in Figure 3.4(b), four different magnetic domains are present, each characterized by the magnetic moment orientation indicated with an arrow. The two domains whose magnetization is perpendicular to the direction of the photon flux appear non-magnetic, since, as explained in section 3.2, XMCD is capable to probe only magnetic moments parallel to the direction of propagation of the light beam. The black and white areas, instead, indicate an opposite magnetic behavior: the difference in contrast between these two areas reflects the opposite magnetic orientation of the domains. Hence, by changing the energy and collecting a contrast image where the XMCD reverts sign, the contrast appears inverted, since we have reverted the momentum brought from the light beam.

- *X-ray photoemission spectroscopy.* The processes described above result from the collection and analysis of the secondary electrons. It is also possible to probe primary electrons with PEEM: the kinetic energy of the emitted electrons is chosen by controlling the so-called start voltage (SV). In the XPEEM experiments described above the SV is set close to zero and the contribution to the signal is mainly brought by the secondary electrons. As we increase the SV, we select electrons with higher kinetic energies, getting rid of the secondary electrons contribution according to the inelastic mean free path of the electrons [171]. In this SV range it is possible to collect primary electrons and, by varying the energy of the incoming photon beam, to obtain an XPS spectra, where the binding energy is defined as the difference between the photon energy and the kinetic energy (i.e., the SV). The disadvantage is that, since the intensity of the primary electrons is much lower than the secondary electrons one, it is challenging to get a space resolved image, for which longer acquisition times are necessary.

3.5 Angle-resolved photoemission spectroscopy

Angle-resolved photoemission spectroscopy (ARPES) is a unique technique which allows one to probe directly the band structure of a crystalline material. Starting from 1960s, it has been widely used in the investigation of condensed matter and has been proven to be fundamental in helping to reveal the hidden electronic properties of novel materials, such as superconductors, topological insulators, 2-D electron gases and many others. Here, we discuss briefly the physics behind the ARPES process and we will introduce soft x-ray ARPES, discussing the advantages and peculiarities of this technique

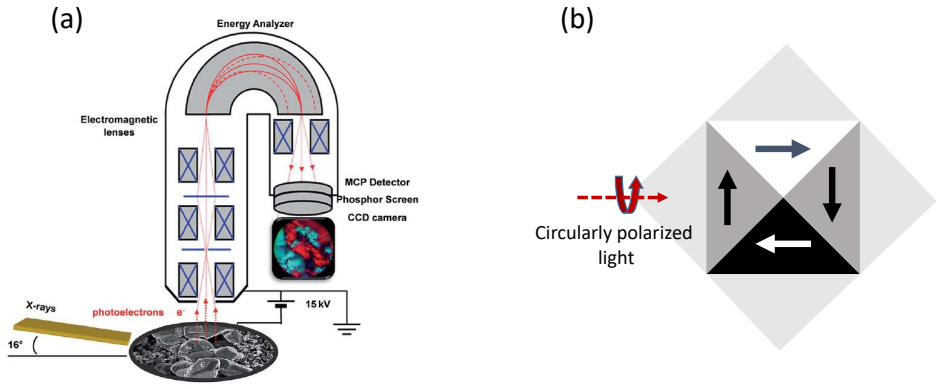

Figure 3.4: (a) Schematics of the XPEEM experimental setup: the secondary electrons are collected by magnetic lenses and focused, after passing the energy analyzer, onto a fluorescent screen (taken from [172]). (b) Example of a PEEM image with different magnetic domains.

as well as drawbacks.

3.5.1 General description

Suppose that a light beam impacts the sample with an angle of incidence θ with respect to the normal to the sample surface. An electron which absorbs such a photon will be photoemitted if the condition $h\nu - \phi - |E_B| > 0$, where $h\nu$ is the incoming photon energy, ϕ is the material work function and $|E_B|$ the electron binding energy, is satisfied. In this case, the kinetic energy (E_k) of the photoemitted electron will be [173–178]

$$E_k = h\nu - \phi - |E_B| \tag{3.20}$$

By using simple relationships, we get

$$E_k = \frac{p^2}{2m} \tag{3.21}$$

$$p = \sqrt{2mE_k} \tag{3.22}$$

where m and p are the mass and the momentum of the electron, respectively. At this point, one could obtain the parallel component of the momentum, dependent on θ:

$$p_{\parallel} = \hbar k_{\parallel} = \sqrt{2mE_k}\sin\theta \tag{3.23}$$

In an ARPES experiment, the sample can generally rotate around three axis [polar, azimuth and tilt, respectively θ, φ and τ, as indicated in Figure 3.5(a)] and the detection of the energy and momentum of the photoemitted electron is performed through an hemispherical analyzer. In this kind of

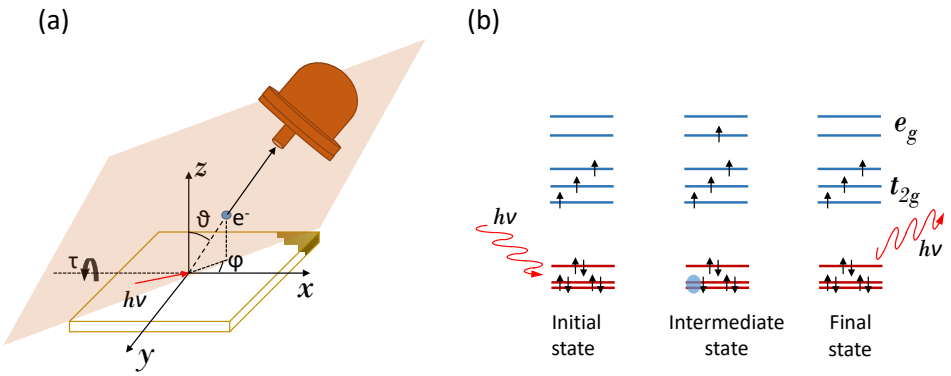

Figure 3.5: (a) Typical geometry of an ARPES experiment, where the angles θ, τ and φ are defined. The scattering plane includes the incoming beam, the photoemitted electron and the detector. (b) Schematic representation of the resonant scattering process, where a virtual excited state is formed between the absorption (initial state) and the emission (final state) of a photon.

detector, two hemispheres are kept at a selected potential difference which deflects the electrons with kinetic energies within a certain range from the chosen energy E_{pass}. The trajectory of the electrons depends both on their energy and on the angle θ. By rotating the sample around the three axis it is therefore possible to navigate the Fermi surface in the x,y plane and to collect the band structure as a function of θ. From a formal perspective, the photoemission problem is generally discussed with a three step model:
(i) The electron absorbs the incoming photon and is excited. The probability of this excitation is described by equation 3.9.
(ii) The photoemitted electron travels through the material towards the sample surface. This step is mainly determined by the mean free path of the electron in a solid [171].
(iii) The electron overcomes the material work function and is photoemitted into the vacuum. Here, because of the breaking of translational symmetry due to surface-vacuum interface, the perpendicular component of the wavevector $\mathbf{k}_\perp$ is not conserved. This is the reason why a proper measurement of the perpendicular component of the Fermi surface can be performed only by making additional approximations.

3.5.2 Soft x-ray ARPES

The main limitations of conventional vacuum ultraviolet (VUV) ARPES are related to the mean free path of the photoemitted electron in the solid, which limits the probing depth of ARPES to the surface states, and the low resolution of the perpendicular component of the wavevector $\boldsymbol{k}_\perp$ due to the breaking of translational symmetry at the interface. While in VUV-ARPES

the photon energies are lower than 100 eV, with soft x-rays it is possible to employ photon energies in the range 300-1600 eV, which change radically the quality and properties of the ARPES measurements. Soft x-ray ARPES (SX-ARPES), pioneered at SPring8 [179,180], brings along three important advantages:
(i) The photoelectron mean free path is increased by a factor of two to five because of its higher kinetic energy, allowing one to probe buried layers with a probing depth up to 2 nm at the Ti L_3 edge [181].
(ii) The definition of $\boldsymbol{k}_\perp$ is much sharper. This is due to two reasons: the higher mean free path λ is, for the Heisemberg uncertainty principle, inversely proportional to the $\boldsymbol{k}_\perp$ resolution ($\Delta\boldsymbol{k}_\perp \propto \lambda^{-1}$) and the photoelectron final state becomes free-electron like, allowing approximations by which it is possible to define $\boldsymbol{k}_\perp$.
(iii) The photoemission matrix elements reduce to the atomic cross section, simplifying the ARPES data analysis.
These advantages make SX-ARPES particularly useful to study heterostructures and multilayer systems or samples which cannot be cleaved in-situ. Furthermore, it is possible to perform resonant experiments, enhancing the photoemission process by a factor 2 or 3 and disentangling the band structures with defined orbital characters. On the other side, a higher photon energy translates into a reduced photoexcitation cross-section, which has to be compensated by a high photon flux requiring synchrotron facilities and beamline instrumentation. Also, the wavelenght of the photoemitted electrons are comparable to the thermal motion amplitudes. This requires low measurement temperatures to reduce the electron-phonon scattering. Finally, the resolution on the momentum is defined (from eq. 3.23) as $\Delta k_\parallel = \sqrt{2mE_k/\hbar^2}\cos\theta\Delta\theta$, where $\Delta\theta$ is the angle acceptance of the analyzer. Therefore, the momentum resolution is higher for conventional ARPES with low kinetic energies.

Matrix element effects and selection rules

The ARPES measured intensity I is defined as [173–178]

$$I(\boldsymbol{k},\omega) = I_0(\boldsymbol{k},\nu,A)f(\omega)A(\boldsymbol{k},\omega) \tag{3.24}$$

where ω is the electron energy with respect to the Fermi surface, $A(\boldsymbol{k},\omega)$ is the one-particle spectral function and $I_0(\boldsymbol{k},\nu,A)$ is directly proportional to the matrix elements defined in equation 3.13. It is clear that, in order to measure photoemission, the overall integral defined in 3.13 must be non-vanishing, i.e., the integrand must be an even function. For simplicity, we consider a symmetry plane which is perpendicular to the sample surface and contains the photon propagation vector and the detector [Figure 3.5(a)] and we suppose that the photoemitted electron can be described with a plane wave [175,182–184]. Since the photoelectron propagation vector is parallel

to the plane (the electron is traveling towards the detector), the wavefront is orthogonal to it, and will hence possess even parity. The symmetry of the integrand is hence defined by the term $(\boldsymbol{\epsilon}\cdot\mathbf{r})\left|\phi_{\mathrm{i}}^{\mathbf{k}}\right\rangle$. Therefore, if $\left|\phi_{\mathrm{i}}^{\mathbf{k}}\right\rangle$ is even under reflection around this plane, $(\boldsymbol{\epsilon}\cdot\mathbf{r})$ must be even (i.e., the polarization of the light must be in-plane), while for $\left|\phi_{\mathrm{i}}^{\mathbf{k}}\right\rangle$ odd, the dipole operator must be odd. These selection rules allow one to distinguish the different orbital characters with symmetry and geometrical arguments, making possible to probe only selected orbital characters in a complex material by tuning the symmetry of the light polarization.
Before closing this section, there is a second effect worth mentioning which is correlated to matrix elements: although the band structure of the system can be directly probed with ARPES, the matrix elements can impose selection rules on the allowed transitions and forbid the access to the whole band structure. It has been observed in graphene and graphite, as well as in systems containing different periodicities, that not all the bands are accessible and measurable with ARPES [185–192]. Hence, it is not uncommon to see a band structure where the periodicity in the Brillouin zone is not observed, and to detect a parabola centered in $k_x = 0$ and no signal in $k_x = 2\pi/a$.

3.6 X-ray resonant reflectivity

The interaction between spin, charge, lattice and orbital degree of freedom is the basic mechanism that governs the rich variety of phenomena that characterize novel materials such as colossal magnetoresistance materials and superconductors. X-ray resonant reflectivity (RXRR) is a technique sensitive to spatial modulations and electronic structure, providing a perfect tool to study simultaneously spatial modulations of spin, charge and orbital degrees of freedom. In a RXRR experiment, the x-ray energy is set to the edge energy of a core electron of a selected element. The core electron, thanks to the photoelectric effect, will be able to perform a dipole-allowed transition to an unoccupied state close to the Fermi energy, after which it will decay back to the initial state emitting a photon with the same energy as the incident one [Figure 3.5(b)]. The scattering problem is well defined through the total coherent elastic scattering amplitude (also called the form factor) defined as [193]

$$f \sim f_0 + f' + if'' + f^{(\mathrm{mag})} \tag{3.25}$$

where f_0 is the Thomson contribution, $f^{(\mathrm{mag})}$ is the magnetic x-ray scattering from a magnetic ion and $f' + if''$ is the contribution from the absorption and dispersive processes, which is a function of the photon energy and of the polarization of the incoming and scattered wave. This last term becomes fundamental when describing the resonant scattering process [193]. Therefore, the knowledge of the atomic scattering factors becomes fundamental when the extrapolation of quantitative information from a resonant scatter-

ing experiment is needed. Although tabulated values are available in the literature, it is better to directly measure the scattering factors in order to consider eventual slight changes in the sample structure and stoichiometry. To this goal, absorption spectra and XMCDs have to be collected and, by using the optical theorem, the components of the scattering factors can be obtained. Indeed, the absorption spectrum is correlated to the imaginary part of the scattering factor; by using the Kramers-Kronig relationship, the real part can be obtained. A detailed treatment of the theory can be found in [194].

RXRR simulation

Two different kinds of data are used in this thesis: angle and energy scans. The former are performed using a fixed beam energy (in resonance with Mn L-edge) and varying the angle of incidence, the latter by choosing a defined angle and varying the energy of the incoming beam across the two Mn L edges. For each scan, circular plus and minus polarizations are used; the difference between the two spectra gives the asymmetry. In this thesis, the quantitative data analysis of the RXRR data is performed using the DYNA software, which, using the matrix formalism developed by *Elzo et al.* [195], reproduces the reflectivity and energy scans. The software requires the knowledge of $f'+if''$ and $f^{(\mathrm{mag})} = m'+im''$, which can be extracted from the XAS and XMCD measurements. In particular, f'' and m'' correspond to the XAS and XMCD spectra, respectively, which can be combined with the off-resonant tabulated values (the tabulated values used in this thesis are extracted from the NIST database [196]) to obtain the f'' and m'' function for a broad energy range. The real part f' can be calculated using the Kramers-Kronig relation [197]

$$f'(E) = \frac{2}{\pi}\int_0^\infty \frac{\omega' f''(\omega')}{E^2-\omega'^2}\mathrm{d}\omega' \tag{3.26}$$

while m' is the difference between f' of two different polarizations.

Once the multilayer structure is defined, DYNA fits the thickness, roughness, density and magnetic moments to the experimental data. In particular, the latter is expressed in units of magnetic moment per atom extracted by the scattering constant m''. In general, also the direction of the magnetic moment can be fitted, although the knowledge of the spin alignment was known a priori in this work.

3.7 Instrumentation

In this section I summarize the main instrumentation used in this thesis. All these instruments are located at the Paul Scherrer Institute (PSI) in Switzerland.

Atomic force microscopy

The atomic force microscopy (AFM) measurements are performed in the Scanning Probe Microscopy (SPM) userlab, using a Bruker Dimension Icon 3100 scanning station mounted on a vibration and sound isolation table. It is equipped with a laser for measuring the vibration of the cantilever and a lock-in amplifier. It can perform AFM measurements in tapping and contact mode as well as magnetic force microscopy measurements by inserting an appropriate tip. Electric gate voltage can be applied to the tip to perform ferroelectric characterization such as piezoresponse force microscopy.

Transport measurements

The transport characterization is carried out in a home-built setup equipped with a liquid He cryostat (with working temperature between 10 and 500 K), a Keithley sourcemeter for applying and measuring voltage, current and resistance, and a four probe contact system in a van der Pauw configuration [198, 199]. The measurements are performed through a Lab View software specifically developed.

SQUID measurements

I have performed the magnetic characterization at the Laboratory for Mesoscopic Systems, ETH Zurich, Switzerland, equipped with a 7 Tesla Quantum Design MPMS3-137 magnetic properties measurement system. It can apply fields up to 7 tesla and operate in the temperature range 2-400 K. It gives the possibility to measure DC as well as vibrating sample magnetization. If not differently specified, a quartz holder has been used to measure the in-plane magnetization.

SIM beamline

At the surface interface microscopy (SIM) beamline of the Swiss light source (SLS), the light is delivered through two undulators which can operate simultaneously and deliver fully polarized linear or circular light in the energy range 90-2000 eV [200]. The permanent station at SIM beamline hosts a photoemission electron microscope which can operate in the temperature range 50-450 K. Depending on the sample holder, it gives the opportunity to apply electric contacts or an out-of-plane magnetic field. By adjusting the start voltage, i.e., by properly selecting the kinetic energy of the electrons, it is possible to observe secondary electrons or photoemitted electrons, allowing PEEM or XPS experiments. The manipulator can rotate by 360°, allowing a magnetic characterization in all the in-plane directions. The field of view goes from 150 μm to 5 μm and the magnetic lateral resolution is $\sim$ 60 nm. By retracting the manipulator the light beam reaches a second endstation which

can be a ptychography chamber, a resonant scattering chamber (RESOXS) or a spectroscopy chamber, all interchangeable with each other. The last two are the ones used in this thesis. RESOXS allows elastic resonant scattering experiments; it is equipped with a permanent magnet and a cryostat with a sample shield to cool down the sample, which is mounted on a 4-axis goniometer. The spectroscopy chamber is instead optimized for XMCD and XLD experiments and allows measurements in total electron yield (TEY) or total fluorescence yield (TFY) using a photodiode. An electromagnet can apply a magnetic field up to 10 kOe and the samples can be cooled down to ~ 20 K.

X-Treme beamline

The X-Treme beamline at SLS is characterized by one undulator which is able to fully polarize the light with circular and linear polarization [201]. It is equipped with a permanent endstation optimized for XMCD and XLD measurements. Differently from the endstation at SIM beamline, it is equipped with a superconducting magnet able to apply a magnetic field up to 6.8 T along the direction of the beam and up to 1 T in the perpendicular plane. The sample temperature can be adjusted from 370 K to 2 K.

ADRESS beamline

The advanced resonant spectroscopy (ADRESS) beamline is optimized for resonant scattering experiments, such as resonant inelastic soft x-ray scattering and soft x-ray ARPES. The light is delivered to the two endstations by an undulator which provides light in the energy range 100-2000 eV [202]. At the ARPES endstation the sample is kept at 10 K, which is a necessary condition in SX-ARPES, and is mounted on a three rotational axis sample holder in order to perform angle resolved photoemission. The detection of the photoemitted electrons is performed using an hemispherical analyzer with an energy resolution better than 5 meV; a MATLAB-based software allows the data collection and analysis.

4

Full Magnetic Polarized Ultrathin $La_{0.8}Sr_{0.2}MnO_3$ Films[1]

4.1 Introduction

The disruption of the atomic structure at the boundary between different materials often gives rise to the emergence of new phenomena that are characteristic of the interface region itself [132, 206]. The study of such interface phenomena is important to understand the role of broken symmetries, electron exchange, and correlation effects to the electronic properties, but may also hold the promise for new electronic devices based on purely interfacial effects. Critical for strong interfacial effects is the growth of sharp and well defined interfaces separating materials with pristine electronic structures; this is because the presence of defects at the interface may strongly disturb the electronic properties of the component phases, for instance, making the

[1] The experimental work in this chapter summarizes the results of three manuscripts submitted for publication [203–205]. My contribution to these papers was the growth of the films, the AFM measurements and the SQUID characterization. The diffraction measurements were carried out by Dr. G. Panchal in collaboration with Dr. C. Schneider. The transport measurements are performed by me in collaboration with Dr. G. Panchal, while the spectroscopic measurements were carried out at SIM beamline by me and Dr. C. A. F. Vaz and at X-Treme beamline by me in collaboration with Dr. D. Vaclavkova and Dr. C. Piamonteze. The XPS and XPEEM measurements were performed at SIM beamline by me, Dr. G. Panchal and Dr. C. A. F. Vaz. I have carried out all the data processing and analysis, with the exception of the XPS and the XPEEM and XLD data, processed by Dr. C. A. F. Vaz and Dr. G. Panchal, respectively.

interdiffused interface of a magnetic material non-magnetic [207] or where the presence of charge traps screens the polarization of a ferroelectric interface [60].

One example of an interfacial effect is the onset of a magnetoelectric coupling emerging at the boundary between ferromagnetic and ferroelectric materials to form multiferroic heterostructures, whereby control of magnetism through electric fields is made possible [9,61,66,68,78,208]. For the particular case of the $Pb(Zr_{0.2}Ti_{0.8})O_3/La_{0.8}Sr_{0.2}MnO_3$ interface, the magnetoelectric coupling was demonstrated to originate from charge-driven modulation of the valency and spin configuration of the interfacial $La_{0.8}Sr_{0.2}MnO_3$ layer induced by charge screening of the ferroelectric polarization [8]. The observed changes in the magnetic moment are of the order of 20%, which is a large effect; however, given the interfacial character of the magnetoelectric coupling, the change in the magnetic moment is associated with only a few unit cells of the whole sample and therefore the total change is averaged out by the remainder of the magnetic film. The latter has a lower thickness limit determined by the magnetic and electric behavior of $La_{1-x}Sr_xMnO_3$ thin films: when grown on high quality $SrTiO_3(001)$ substrates, the onset of electric conductivity occurs at about 10 unit cells (uc), while the magnetic moment is strongly reduced and is absent below 5 uc [209,210], forming magnetic and electric 'dead layers' whose origin has been variously attributed to magnetic or orbital interfacial reconfiguration, cation intermixing or polar discontinuity [20–23,23–32]. It is therefore important to devise solutions for obtaining ultrathin films with bulk-like or with enhanced interfacial characteristics, including full magnetic and ferroelectric polarizations in ferromagnetic and ferroelectric systems, respectively. In addition, one also expects that the relative importance of the interfacial effect will increase as the thickness is reduced, since the interface will then be a larger portion of the overall system. Hence, it is also important that not only the interface is well defined, but also that the electronic properties of the material remain robust with decreasing thickness, ideally down to the monolayer range [60,207].

To overcome the degradation in the magnetic properties of ultrathin manganites, one strategy consists of decoupling the films from the non-magnetic substrate by inserting a magnetically polarized buffer layer [22, 33,34]. For example, the introduction of 2 uc $LaMnO_3$ between a 120 nm thick $La_{1-x}Sr_xMnO_3$ ($x = 0.4$) and the $SrTiO_3$ substrate leads to the disappearance of the dead layer as measured by second harmonic signal generation and ascribed to the interruption of the charge transfer across the $SrTiO_3$ interface, which is otherwise responsible for hole doping of the $La_{0.6}Sr_{0.4}MnO_3$ film [22]. In another instance, 1 uc $La_{1-x}Ba_xMnO_3$ ($x = 0.3$) films sandwiched between two 3 uc $SrRuO_3$ layers are found to be fully magnetically polarized, an effect attributed to the presence of oxygen octahedral rotations induced by the $SrRuO_3$, leading to an orbital reconstruction and an enhancement of the interfacial magnetic properties [35]. In another exam-

ple, $CaRu_{1/2}Ti_{1/2}O_3$ used as interlayer in $La_{2/3}Ca_{1/3}MnO_3$ superlattices has been shown to preserve the magnetic properties of the individual manganite films and to result in antiferromagnetic interlayer coupling [36]. These studies highlight the importance of separating the manganite film from the supporting $SrTiO_3$ substrate and highlight the role of charge transfer, spin exchange and octahedral tilting, together with orbital rearrangement, to the improvement of the magnetic properties toward bulk characteristics.

In this chapter, we explore the magnetic and transport properties of ultrathin $La_{0.8}Sr_{0.2}MnO_3$ films when a manganite buffer layer is introduced at the interface with the $SrTiO_3$ substrate. We employ two different types of buffer layers, a nominally antiferromagnetic insulating $LaMnO_3$ and an antiferromagnetic conducting $La_{0.45}Sr_{0.55}MnO_3$, in order to disentangle the roles of spin and charge exchange at the interface. In the first case, our results show that the $La_{0.8}Sr_{0.2}MnO_3$ film develops robust magnetic properties, with near bulk-like critical temperature and magnetic moments that are independent of thickness starting at 1 uc. In the second case, an antiferromagnetic coupling to the buffer layer is observed for thicknesses up to 3 uc, while for larger thicknesses the top $La_{0.8}Sr_{0.2}MnO_3$ layer transitions to a fully-polarized ferromagnetic state. By probing the electronic band structure using x-ray absorption spectroscopy, we link the magnetic properties of the $La_{0.8}Sr_{0.2}MnO_3$ to the evolution of the orbital occupancy with film thickness.

4.2 Experimental details

The samples in this study consist of $La_{0.8}Sr_{0.2}MnO_3$ films with thicknesses ranging from 0 to 10 uc, grown on a 12 uc $LaMnO_3$ buffer layer (except for the 3 uc $La_{0.8}Sr_{0.2}MnO_3$ sample, grown on 14 uc $LaMnO_3$) or on a 15 uc $La_{0.45}Sr_{0.55}MnO_3$ buffer layer. Figure 4.1(e) shows a schematic diagram of the sample structure. For this study, we used commercially available $SrTiO_3$(001) substrates (SurfaceNet), with $\pm 0.1^o$ miscut, which were chemically treated with a HCl:HNO_3 solution and annealed to 1000 °C in air to provide single TiO_2-terminated surfaces [159, 160]. After growth, the samples belonging to the $LaMnO_3$ series are annealed in air at 600 °C for 6 hours to fully oxygenate the films. Henceforth, the samples are named with the thickness of the top $La_{0.8}Sr_{0.2}MnO_3$ layer in uc. In order to investigate the magnetic properties of the $LaMnO_3$ buffer layer, series of 12 unit cells (uc) thick $LaMnO_3$ films (labelled LMO1-4) were deposited onto TiO_2-terminated $SrTiO_3$(001) substrates. The substrates were held at a temperature of 720°C during growth, except for LMO3 grown at 700°C, and the growth process was monitored by reflection high energy electron diffraction (RHEED).

X-ray absorption spectroscopy (XAS) measurements were carried out at the SIM and X-Treme beamlines at the Swiss Light Source (SLS) at the

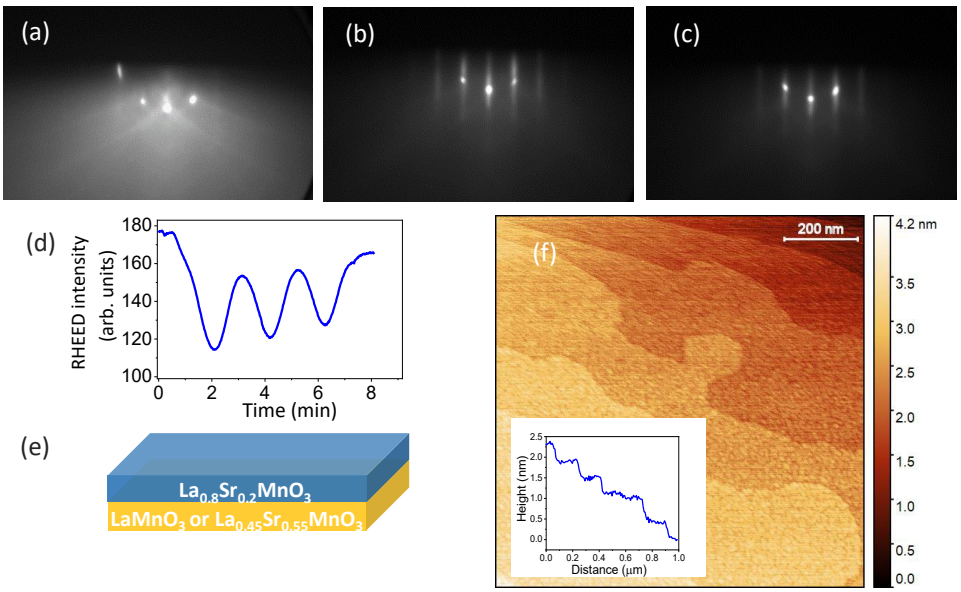

Figure 4.1: (a-c) RHEED patterns of the TiO_2-terminated $SrTiO_3(001)$ substrate, $LaMnO_3$ buffer layer and 3 uc $La_{0.8}Sr_{0.2}MnO_3/LaMnO_3$ film, respectively, along the $\langle 100 \rangle$ azimuth. The energy of the incident electron beam was set to 15 keV. (d) RHEED intensity oscillations as a function of time for a 3 uc $La_{0.8}Sr_{0.2}MnO_3$ deposited on $LaMnO_3$. (e) Schematic of the sample structure. (f) AFM measurement after the growth of 10 uc $La_{0.8}Sr_{0.2}MnO_3/LaMnO_3$, showing a flat surface with single unit cell step terraces (inset). Figure taken from [203].

Paul Scherrer Institute (PSI), Switzerland, with the signal collected in total electron yield (TEY) mode, which has a high surface sensitivity due to the limited mean free path of the electrons in solid materials. When measuring at SIM, before each magnetic XAS measurement, a saturation field of 1 kOe was applied to the sample and the measurements were performed under 200 Oe magnetic field. At X-Treme, the saturation field is 6 T and the measurements are performed at remanence. We have collected XAS spectra with circularly left and right polarized light, from which we obtain the unpolarized (average) spectra and the x-ray magnetic circular dichroism (XMCD) spectra (difference). The latter are normalized by dividing it by the L_3 peak intensity of the respective average XAS spectrum to give the dichroic signal as percentage of the average XAS spectrum. Linear dichroism measurements were carried out at room temperature by measuring the XAS spectra with the sample at a normal angle of incidence and at 45^o to probe, respectively, the in-plane and out of plane orbital states; for one sample (5 uc $La_{0.8}Sr_{0.2}MnO_3/La_{0.45}Sr_{0.55}MnO_3$), the x-ray

linear dichroic (XLD) measurements were carried out using the x-ray photoemission electron microscope at the SIM beamline, where the light impinges the sample at a grazing angle of 16°. In order to compare spectra taken at different geometries, the out of plane XAS spectra is calculated using the expression for the angular dependence of the linear dichroism, $I(\theta) = I_{ab}\cos^2\theta + I_c\sin^2\theta$, where θ is the angle of incidence of the light with respect to the sample surface and I_{ab}, I_c, the x-ray absorption parallel to the sample surface and perpendicular to it, respectively. Local chemical characterization of the samples was carried out at room temperature with x-ray photoemission electron microscopy (XPEEM) at the SIM beamline, operated in x-ray photoemission spectroscopy (XPS) mode [211]. The measurements were carried out by fixing the acceptance energy of the energy analyser (100 and 600 eV) and varying the photon energy, thereby setting the kinetic energy of the detected electrons and the probing depth (a few Å and 2-3 nm, respectively) [171]. XPEEM magnetic measurements were also performed for LMO4 $LaMnO_3/SrTiO_3/SrTiO_3(001)$ and for the $La_{0.8}Sr_{0.2}MnO_3/La_{0.45}Sr_{0.55}MnO_3$ series at 80 K.

4.3 Results

4.3.1 The role of interdiffusion on the magnetism of ultrathin $LaMnO_3$ films

Before going into the details of the magnetic properties of the heterostructures, let us focus on the $LaMnO_3$ buffer layer itself. In its bulk form, $LaMnO_3$ orders antiferromagnetically below 143 K and exhibits an orbital ordered state (up to 780 K) as a result of the Jahn-Teller instability that lifts the degeneracy of the e_g orbitals of the Mn^{3+} [121,212]. However, a strong dependence of the magnetic properties of $LaMnO_3$ on the oxygen stoichiometry has been remarked, where both oxygen excess and deficiency leads to the presence of a non-zero magnetization. In the case of oxygen excess, the ferromagnetic component has been associated with the introduction of La and Mn vacancies that lead to the presence of Mn^{3+}-Mn^{4+} clusters driven to the ferromagnetic state by the double-exchange interaction [37–44], while for oxygen deficiency, the presence of an orthorhombic magnetic phase has been identified [50]. Interest in the magnetic properties of thin $LaMnO_3$ films has also been extensive, in particular since other control parameters can be added, including epitaxial strain induced by the substrate. In fact, *ab initio* calculations have predicted that $LaMnO_3$ becomes ferromagnetic with an enhanced moment when strained in-plane to the lattice parameter of $SrTiO_3$ [51,213,214]. Also in thin films, the oxygen pressure during growth impacts significantly the amplitude of the magnetic moment [45–48], and presence of Mn in a mixed valence state has also been highlighted [47,49]. In

order to better understand the nature of magnetism in the $LaMnO_3$ film, we carried out a detailed study of its magnetic and structural properties, both as-grown and after an annealing step.

Typical RHEED patterns taken immediately after film growth are presented in Fig. 4.2(a-d). They show sharp diffraction spots lying on a Laue arc, characteristic of atomically smooth surfaces, although an elongation along the vertical direction suggests the presence of some surface disorder. Following the time dependence of the RHEED spot intensity allows one to determine the evolution of the surface structure quality and to accurately determine the film thickness through the oscillations in intensity that occur in layer-by-layer film growth, shown in Fig. 4.2(e); the oscillations in the RHEED intensity develop after a time delay, suggesting that the film growth starts as island growth before the surface quality improves with continued $LaMnO_3$ growth. Therefore, although the final RHEED patterns look similar, the film growth process can differ slightly. Atomic force microscopy of the as-grown samples show that the films are atomically smooth, reproducing the atomic step structure of the $SrTiO_3(001)$ substrate. The LMO4 series consist of $LaMnO_3$ films grown simultaneously on three different substrates, $SrTiO_3$, $(LaAlO_3)_{0.3}(Sr_2AlTaO_6)_{0.7}$ (LSAT), and on 4 uc $SrTiO_3/SrTiO_3(001)$, with the $SrTiO_3$ layer grown homoepitaxially on a separate step; the samples were annealed after growth. The lattice parameter for cubic LSAT is a=3.86 Å and for $SrTiO_3$ a=3.905 Å, while the lattice parameters of orthorhombic $LaMnO_3$ are a=5.5367 Å, b=5.7473 Å, and c=7.6929 Å [215], giving an average pseudo-cubit lattice constant of a=3.99 Å. LSAT is more stable to oxygen loss at high temperatures in reducing conditions [161] and has a different lattice mismatch compared to $SrTiO_3$. As shown in Fig. 4.2(f) for LMO2, the as-grown samples show the presence on Mn^{2+}, suggesting that the films are oxygen deficient. Hence, the samples are subsequently grown in pairs and one of the samples is annealed at 600°C for 6 h in air in a tube furnace to fully oxidize the $LaMnO_3$ films. The temperature was chosen to be below that of the growth temperature to minimize mass transport. After annealing, the $LaMnO_3$ XAS spectra show no presence of the Mn^{2+} feature, Fig. 4.2(f).

In Fig. 4.3 we present the results of the bulk magnetic characterization. A first observation is the presence of a ferromagnetic component for both as-grown and annealed samples, which is not expected for stoichiometric bulk $LaMnO_3$ but is similar to what has been reported previously in the literature for $LaMnO_3$ thin films [45–49, 51, 216–218]. The critical temperature is of about 125 K for the as-grown samples but increases to 150-225 K after annealing; as a comparison, the Néel temperature of bulk $LaMnO_3$ is 143 K [121]. Also the behavior at low temperatures is markedly different between the as grown and annealed samples: if no field is applied upon cooling [ZFC curves, marked with empty circled in Figure 4.3(a)] the shape at low temperatures deviates from the field cooled one (filled circles), while

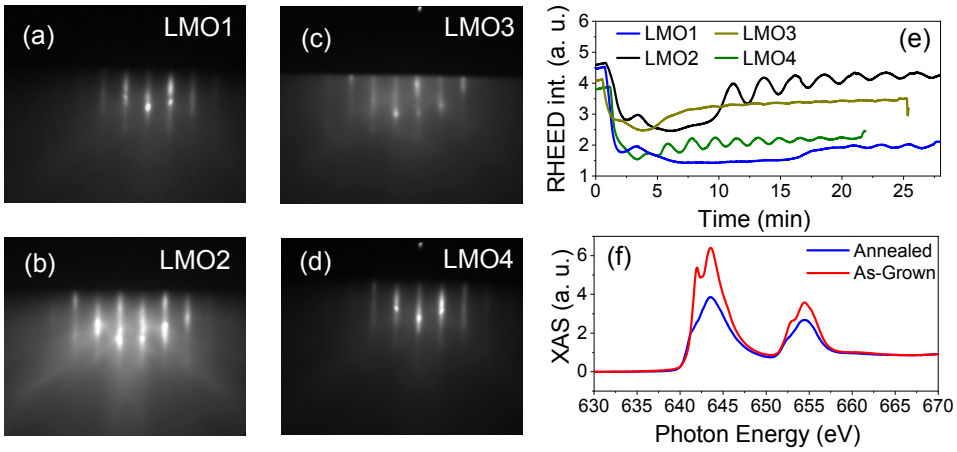

Figure 4.2: (a-d) RHEED patterns of the $LaMnO_3/SrTiO_3(001)$ films. (e) RHEED intensity oscillations observed during film growth for samples LMO1-4. (f) X-ray absorption spectroscopy at the Mn L edge for LMO2. Figure taken from [204].

the same behavior is not observed after the annealing step, where the two curves overlap. The magnetic moment shows a larger variability, ranging from 0.75-1.2 μ_B/Mn at low temperature and increasing as well for the annealed samples. As observed, the magnetic moment is much smaller than the ionic value of 4 μ_B/Mn of the spin $S = 2$ state of Mn^{3+}. The magnetic hysteresis curves also change markedly after annealing, where the large coercivity and rounded *M-H* loops of the as-grown samples give way to curves that have very small coercive fields. In order to determine the impact of the substrate on the magnetic properties of the $LaMnO_3$ films, we have prepared one $LaMnO_3$ series (LMO4) on three different substrates, as already mentioned. The results for the LMO4 samples in Fig. 4.4 show no significant differences between the two $SrTiO_3(001)$ templates and slightly reduced properties for film grown on LSAT.

To determine the origin of the measured magnetic moment, we carried out magnetic x-ray spectroscopy measurements on samples LMO1 and LMO2. Figure 4.5(a) shows the unpolarized XAS spectra before and after annealing. We observe the presence of a strong Mn^{2+} feature in the as-grown samples, whose impact can be seen in the XMCD spectra presented in Fig. 4.5(b) as a sharp drop to zero, showing that this contribution is non-magnetic. In contrast, the spectra of the annealed samples show a slight shift in peak position to higher energies and no Mn^{2+} peak. Despite the slight differences in the spectra, what is clear is that the magnetic signal originates from the Mn cations and increases slightly with sample annealing.

One may attribute the changes in the magnetic properties upon annealing to the full oxidation of the $LaMnO_3$ film, even if stoichiometric $LaMnO_3$

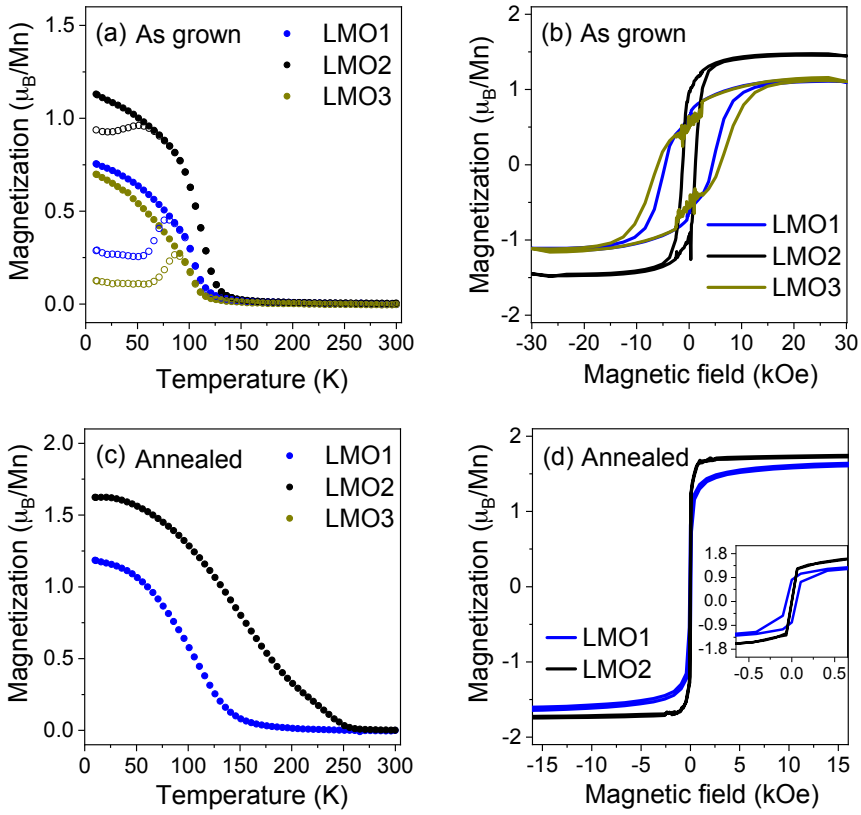

Figure 4.3: SQUID magnetometry data for LMO1-3. Figure adapted from [204].

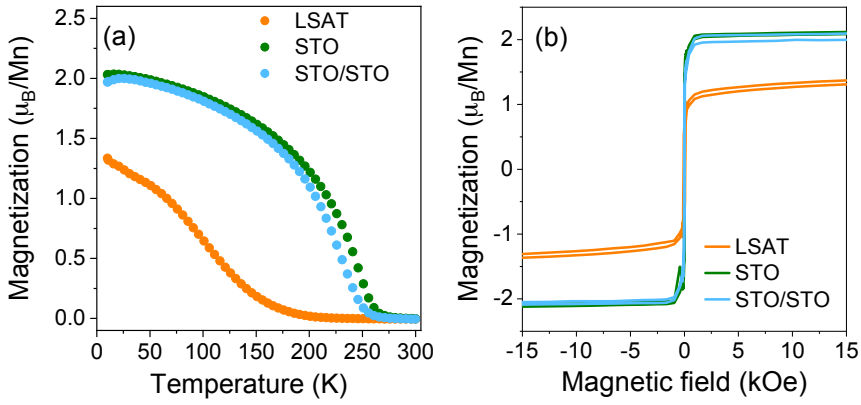

Figure 4.4: SQUID magnetometry data for LMO4. Figure adapted from [204].

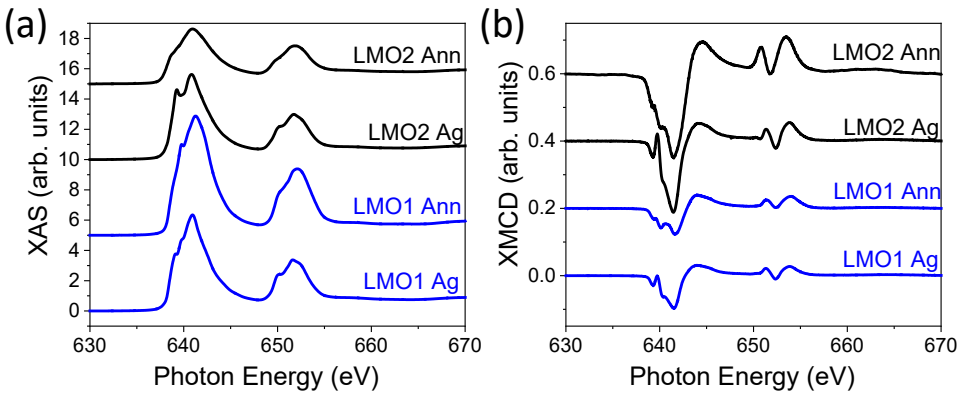

Figure 4.5: (a) XAS and (b) XMCD spectra (normalised to the XAS peak amplitude) for samples LMO1-2. The spectra have been shifted vertically for ease of display. Figure taken from [204].

should be antiferromagnetic. Epitaxial strain could also play a role in driving the system to a ferromagnetic state, although the observation of reduced moments on several substrates seems to suggest that strain may not be the main factor leading the emergence of ferromagnetism in $LaMnO_3$ thin films. Our results show further that the $SrTiO_3$ buffer layer has no significant effect on the magnetic properties, indicating that defects at the $SrTiO_3$ substrate surface are not the determinant factor for the magnetic properties.

A concern with the growth of $LaMnO_3$ on $SrTiO_3$ substrates is that Sr can interdiffuse into the $LaMnO_3$ film, effectively doping it and driving the system into a spin canted ferromagnetic insulating state [121, 219, 220]. To determine whether Sr diffuses from the $SrTiO_3$ substrate to the $LaMnO_3$ film, we carried out XPS measurements using XPEEM [211]. In Fig. 4.6(b) we show the spectra taken for LMO1 over the two small regions of the sample labeled in Fig. 4.6(a). In this region of the sample we identified a defect that exposes the $SrTiO_3$ substrate, as confirmed by the observation of a Ti signal (together with a strong Mn signal, showing that the defect does not simply expose the substrate). We observe no Ti signal over the non-defective area of the surface, in agreement with the limited probing depth of the XPS at a kinetic energy of 100 eV used here. Tellingly, we find the presence of a strong Sr signal over the same area, as well as the presence of a Si impurity signal, which is stronger over the defective region and of Ca, identified in the XAS signal that appears in XPS overview scans as the photon energy was varied. The fact that the impurities arise from the substrate and are not present in the MBE sources is confirmed by measuring a Nb-doped $SrTiO_3$ substrate and a $LaMnO_3$ thin film grown on a Si chip, the former showing Ca and Si impurities, the latter exhibiting no Ca XAS signal. These results confirm the presence of Sr, Ca, and Si, the latter two well-known impurities

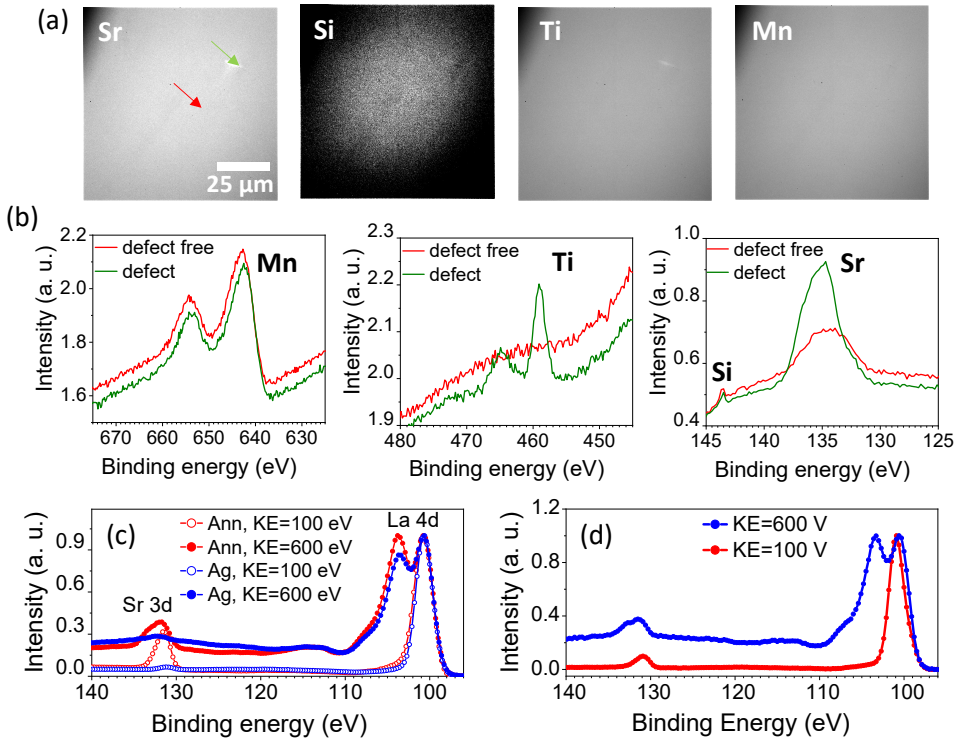

Figure 4.6: (a) XPS spectra for sample LMO1 taken at the two positions indicated in (b), which shows elemental contrast images showing the Sr, Si, Ti, and Mn signal distribution across the sample. (c,d) XPS spectra measured at different kinetic energy of the photoelectrons for samples LMO1 and LMO4 ($LaMnO_3$/LSAT), respectively. Figure taken from [204].

of $SrTiO_3$ [221]. In Fig. 4.6(c) we compare XPS measurements of LMO4 at two values of the electron kinetic energy, showing that, although the Sr signal is detected in all cases, it is weaker at the surface and also in the as-grown film, indicating that the annealing procedure promotes further Sr diffusion. However, also for LMO3, grown at 700°C, and $LaMnO_3$/LSAT, we find the presence of Sr, although in lower amount compared for the $SrTiO_3$ substrate. In fact, the distribution of Sr across $La_{1-x}Sr_xMnO_3$ films grown on $SrTiO_3$ has been addressed in the literature, including studies reporting a non-uniform Sr distribution [222], which may be driven by the tendency for Sr and Ca to segregate to the $SrTiO_3$ surface [223, 224].

The Sr signal present in the $LaMnO_3$ films is significant and could represent a few % in content; one expects that its presence will impact the magnetic properties of the $LaMnO_3$ film, in particular, by adding hole carriers and driving it into the ferromagnetic insulating regime of $La_{1-x}Sr_xMnO_3$.

4.3.2 Magnetic, electric and spectroscopic characterization of ultrathin $La_{0.8}Sr_{0.2}MnO_3$ films

In this section, we discuss the results on the $La_{0.8}Sr_{0.2}MnO_3/LaMnO_3$ and $La_{0.8}Sr_{0.2}MnO_3/La_{0.45}Sr_{0.55}MnO_3$ heterostructures. To determine the strain state of the heterostructures, we carried out x-ray diffraction measurements on the two 10 uc $La_{0.8}Sr_{0.2}MnO_3$ films. The θ-2θ scans around the (002) $SrTiO_3$ peak are shown in Fig. 4.7(a,b) for the $LaMnO_3$ and $La_{0.45}Sr_{0.55}MnO_3$ buffer layers, respectively. In both cases, broad peaks to the right of the (002) $SrTiO_3$ line are observed, corresponding to the pseudo-cubic (002) planes of the manganite films; in the case of the $LaMnO_3$ buffer layer, only one peak can be distinguished; by fitting the peak with three Gaussian components [Fig. 4.7(a)], one for the $SrTiO_3$ peak together with a diffused scattering component and a third for the $LaMnO_3/La_{0.8}Sr_{0.2}MnO_3$ bilayer, we obtain for the latter an out of plane lattice parameters of 3.87 Å, which is below both $LaMnO_3$ and $La_{0.8}Sr_{0.2}MnO_3$ pseudocubic bulk values of $a/\sqrt{2} = 3.89$ Å [121]. For the case of the film with $La_{0.45}Sr_{0.55}MnO_3$ buffer layer, we observe the presence of clear Laue oscillations, indicative of high quality interfaces and that the manganite peak is composed of two overlapping components [Fig 4.7(b)], which we ascribe to the $La_{0.8}Sr_{0.2}MnO_3$ and $La_{0.45}Sr_{0.55}MnO_3$ films. By fitting this peak to two Gaussian components together with the $SrTiO_3$ peak with a diffused scattering component, we obtain out of plane lattice parameters of 3.84 Å and 3.81 Å, which we assign to the $La_{0.8}Sr_{0.2}MnO_3$ and $La_{0.45}Sr_{0.55}MnO_3$ films, respectively. These values are considerably smaller than the respective pseudocubic bulk lattice parameters of 3.89 Å and 3.84 Å, [94, 95, 121] as expected for tensile strain induced by the $SrTiO_3$ substrate. Reciprocal space mapping (RSM) around the asymmetric (103) plane of $SrTiO_3$ are shown in Fig. 4.7(c,d) for the $La_{0.8}Sr_{0.2}MnO_3/LaMnO_3$ and $La_{0.8}Sr_{0.2}MnO_3/La_{0.45}Sr_{0.55}MnO_3$, respectively. One finds that the Bragg reflection corresponding to the film bilayer lies at the same Q_x value for both heterostructures, which directly shows that the manganite films grow coherently to the $SrTiO_3$ substrate and are fully strained. We expect likewise that the thinner $La_{0.8}Sr_{0.2}MnO_3$ films to be also fully strained to the $SrTiO_3$ substrate.

The temperature dependence of the magnetization (M-T) of the ultrathin $La_{0.8}Sr_{0.2}MnO_3/LaMnO_3$ films as the function of $La_{0.8}Sr_{0.2}MnO_3$ thickness is shown in Fig. 4.8(a). For the $La_{0.8}Sr_{0.2}MnO_3$ films, the results show that starting from 1 uc $La_{0.8}Sr_{0.2}MnO_3$, the Curie temperature jumps to T_C=260 K (compared with 309 K for bulk $La_{0.8}Sr_{0.2}MnO_3$ and 305 K for thick $La_{0.8}Sr_{0.2}MnO_3$/STO(001), slightly reduced from the bulk value due to epitaxial tensile strain) [121, 209]; with increasing $La_{0.8}Sr_{0.2}MnO_3$ thickness, T_C is seen to oscillate around 250 K, as shown in inset I of Fig. 4.8(c), which resembles the oscillatory behavior of the critical temperature observed in ultrathin Fe and Co films as a function of the Cu capping layer thickness

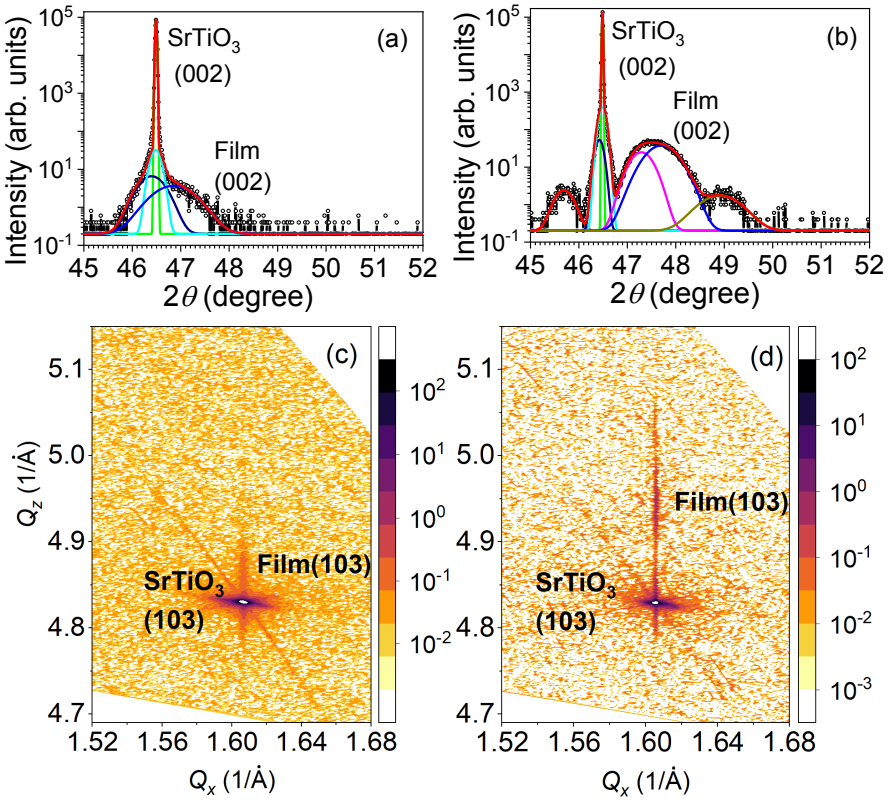

Figure 4.7: θ-2θ x-ray diffraction scans for (a) 10 uc $La_{0.8}Sr_{0.2}MnO_3/LaMnO_3$ and (b) 10 uc $La_{0.8}Sr_{0.2}MnO_3/La_{0.45}Sr_{0.55}MnO_3$ heterostructures. Reciprocal space mapping around the asymmetric (103) Bragg reflection of $SrTiO_3$ for (c) 10 uc $La_{0.8}Sr_{0.2}MnO_3/LaMnO_3$ and (d) 10 uc $La_{0.8}Sr_{0.2}MnO_3/La_{0.45}Sr_{0.55}MnO_3$. Vertical scale represents the scattering intensity, in arbitrary units. Figure taken from [203].

(attributed in this case to a contribution from a Ruderman-Kittel-Kasuya-Yoshida type of exchange coupling in itinerant ferromagnets) [207, 225, 226] and which could be a manifestation of finite-size effects. Notably, we find no independent contribution from the $LaMnO_3$ buffer layer in the M-T curves, indicating that the two layers are fully coupled magnetically. We observe as well a steady increase in the saturation magnetization with increasing thickness, which we quantify from magnetic hysteresis curves carried out at 20 K, shown in Fig. 4.8(b). These data show that the $La_{0.8}Sr_{0.2}MnO_3$ films have small coercive fields, of ∼50 Oe, except for the 2 and 10 uc $La_{0.8}Sr_{0.2}MnO_3$ films, which exhibit coercive fields of ∼300 Oe. By extrapolating from the high field region to zero field, we estimate the zero-field saturation magnetization as a function of thickness, shown in Fig. 4.8(c), to find that the saturation moment increases linearly with thickness, with a

slope of 3.8 μ_B/uc expected for bulk $La_{0.8}Sr_{0.2}MnO_3$, shown as a red line. This result demonstrates that the insertion of an $LaMnO_3$ buffer layer results in $La_{0.8}Sr_{0.2}MnO_3$ films that are fully spin-polarized down to 1 uc. The intercept at the origin gives the magnetization of $LaMnO_3$, of 20.7 μ_B/uc area, corresponding to an average magnetic moment of 1.7 μ_B/Mn, in agreement with previous findings in the literature [47,48]. Assuming the $LaMnO_3$ moment to be constant throughout the sample series, we can subtract its (constant) magnetic contribution to obtain the linear behavior shown in the inset II of Fig. 4.8(c). For the 3 uc $La_{0.8}Sr_{0.2}MnO_3$ thickness, we expect a slightly larger magnetic moment due to the thicker $LaMnO_3$ layer (14 uc) and in the inset II of Fig. 4.8(d) we show the magnetic moment after subtracting an additional moment of 3.4 μ_B corresponding to the extra 2 uc $LaMnO_3$. These results highlight the fact that the $La_{0.8}Sr_{0.2}MnO_3$ films develop a full magnetic moment starting from the first unit cell.

The transport properties are shown in Fig. 4.8(d). We find that the 12 uc thick $LaMnO_3$ film is insulating, consistent with previous reports and as expected for bulk $LaMnO_3$ [121,216]; importantly, starting from 1 uc thickness, the films exhibit a clear peak in the resistivity at a temperature near the magnetic critical temperature [inset I of Fig. 4.8(c)], typical of the mixed valence "colossal" magnetoresistance (CMR) manganites [227]; the 2 and 4 uc $La_{0.8}Sr_{0.2}MnO_3$ films show a second transition to insulating behavior at low temperature, which is often found in thin $La_{0.8}Sr_{0.2}MnO_3/SrTiO_3(001)$ films and attributed to A-site disorder-induced charge localization effects [228]. These results show that also the transport properties of the ultrathin $La_{0.8}Sr_{0.2}MnO_3$ films are similar to that of the bulk counterpart [121].

The results for the case of $La_{0.8}Sr_{0.2}MnO_3/La_{0.45}Sr_{0.55}MnO_3$ are markedly different. The magnetic hysteresis loops, presented in Fig. 4.9(a), show that the $La_{0.45}Sr_{0.55}MnO_3/SrTiO_3(001)$ film exhibit no magnetic hysteresis, consistent with the expected antiferromagnetic state reported earlier [95]. Also, the $La_{0.8}Sr_{0.2}MnO_3$ films up to 3 uc thickness show a negligible magnetic response to the applied magnetic field, while for thicknesses above 4 uc, magnetic hysteresis is present with coercive fields in the range from 50-100 Oe. The magnetic behavior is also confirmed by temperature dependent magnetization measurements shown in Fig. 4.9(b) for the 4, 5, 8 and 10 uc films, where the onset of magnetization in the system is observed at 250 K (with the 4 uc film showing an uptick in the magnetization at around 100 K). Remarkably, the 10 uc $La_{0.8}Sr_{0.2}MnO_3$ film reaches a critical temperature of about 300 K, close to the bulk value. The saturation magnetic moment extracted from the *M-H* curves is presented in Fig. 4.9(c) and shows an approximately linear increase in the magnetization for thicknesses above 3 uc with a slope of about 3.8 μ_B/uc.

The resistivity of the $La_{0.8}Sr_{0.2}MnO_3$ series grown on $La_{0.45}Sr_{0.55}MnO_3$ as a function of temperature is shown in Fig. 4.9(d). Since in this case the buffer layer brings a non-negligible contribution to the total resistivity, the

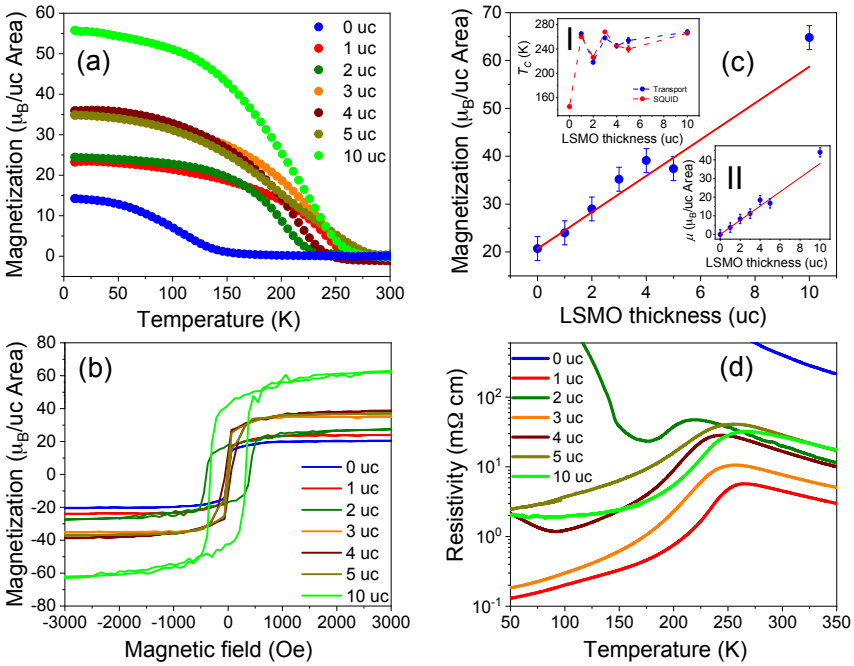

Figure 4.8: (a) Field-cooled magnetization variation with temperature of the $La_{0.8}Sr_{0.2}MnO_3/LaMnO_3$ films taken during heating (applied magnetic field of 1 kOe). (b) Magnetic hysteresis curves at 20 K. (c) Magnetization per unit cell area versus $La_{0.8}Sr_{0.2}MnO_3$ film thickness extrapolated at zero-field from the *M-H* loops (symbols); the red line has a slope of 3.8 μ_B/uc. Inset (I) shows the variation of the critical temperature (SQUID) and of the peak in resistivity as a function of $La_{0.8}Sr_{0.2}MnO_3$ film thickness (dashed lines are guides to the eye); inset (II) shows the magnetic moment (μ) variation without the $LaMnO_3$ moment contribution. The error bars in the magnetization are related to the experimental uncertainty due to the $LaMnO_3$ thickness. (d) Resistivity versus temperature for the $La_{0.8}Sr_{0.2}MnO_3/LaMnO_3$ sample series. Figure taken from [203].

latter is calculated using the bilayer film thickness. The 0 uc sample shows a metal to insulator transition (MIT) at $T_{MIT} = 287$ K, in agreement with previous reports [95]. The reduced resistivity and increased MIT temperature (T_{MIT}) of the 1, 2 and 3 uc samples show that the $La_{0.8}Sr_{0.2}MnO_3$ layers have lower resistivity compared to the buffer layer. The 4 uc thick $La_{0.8}Sr_{0.2}MnO_3$ on $La_{0.45}Sr_{0.55}MnO_3$ buffer layer shows instead a drop in T_{MIT}, as also shown in the figure inset. A further increase in T_{MIT} is observed for the 5 and 10 uc samples, saturating at $\sim$ 300 K. The critical temperature estimated from the peak resistivity is found to be significantly different from that estimated from the *M-T* curves, a discrepancy that is much larger than for the

$La_{0.8}Sr_{0.2}MnO_3/LaMnO_3$ series. For example, for the 5 u.c. film, the critical temperature obtained from the magnetization curve is about 260 K, while the peak in the resistivity remains close to that of the 3 uc $La_{0.8}Sr_{0.2}MnO_3$, of about 290 K. This fact implies that at and above 5 uc thickness, the ferromagnetic component of the $La_{0.8}Sr_{0.2}MnO_3$ film is magnetically decoupled from the manganite layers underneath. The kink at around 100 K observed for the 1-4 uc films is due to the $SrTiO_3$ cubic to tetragonal phase transition, which affects particularly strongly $La_{1-x}Sr_xMnO_3$ films at near the 0.5 doping [95, 229].

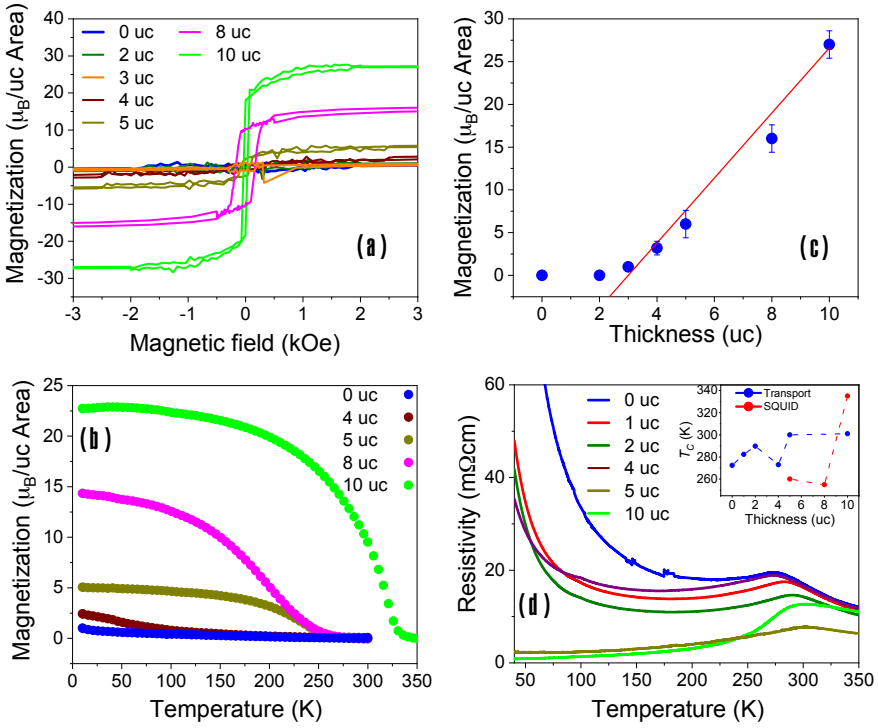

Figure 4.9: (a) Magnetization hysteresis curves at T=20 K of the $La_{0.8}Sr_{0.2}MnO_3/La_{0.45}Sr_{0.55}MnO_3$ sample series and (b) magnetization temperature dependence of the 0, 4, 5, 8 and 10 uc $La_{0.8}Sr_{0.2}MnO_3$ films. (c) Zero-field saturation moments extrapolated from the M-H loops. The red line has a slope of 3.8 μ_B/uc crossing the abscissa at 3 uc. (d) Transport measurements showing the evolution of the temperature dependent resistivity with thickness. The metal to insulator transition variation with thickness, identified as T_C, is shown in the figure inset together with the Curie temperature, obtained as linear extrapolation to zero from the M-T curves. Figure taken from [203].

We interpret the results for the $La_{0.8}Sr_{0.2}MnO_3/La_{0.45}Sr_{0.55}MnO_3$ as

showing that the 1-3 uc $La_{0.8}Sr_{0.2}MnO_3$ films couple antiferromagnetically to the $La_{0.45}Sr_{0.55}MnO_3$ buffer layer, while for larger thicknesses the additional layer change abruptly to a ferromagnetic state. The increase in the Néel temperature (corresponding to T_{MIT} in these films) for 1-3 uc indicates an increase of the magnetic exchange interaction, while the large difference between T_C and T_{MIT} shows that the ferromagnetic layers are magnetically decoupled from the antiferromagnetic layer underneath. Starting from 4 uc thickness, the magnetic moment increases linearly with a slope of $3.8\mu_B$/Mn, indicated by the red line in Fig. 4.9(c), similar to the $LaMnO_3$ buffer layer case, but shifted by 3 uc.

In order to understand better the magnetic and electronic properties of the $La_{0.8}Sr_{0.2}MnO_3$ films, we carried out x-ray magnetic spectroscopy measurements. In Fig. 4.10(a) and (b) we show the evolution of the non-polarized XAS spectra with thickness for the films grown on the $LaMnO_3$ and $La_{0.45}Sr_{0.55}MnO_3$ buffer layers, respectively. For the case of the films grown on $LaMnO_3$, we find no significant changes in the spectra across the sample series, which show features characteristic of fully oxidized $La_{0.8}Sr_{0.2}MnO_3$ [230, 231]. The spectra corresponding to the 0 and 10 uc samples were collected at the X-Treme beamline and show a different peak amplitude, attributed to different background and measurement conditions between the two endstations. The corresponding normalized XMCD spectra are shown in Fig. 4.10(c). Similar to the XAS, we find no significant changes in the shape and amplitude of the XMCD spectra; the 0 and 10 uc samples show a reduced and enhanced XMCD signal, respectively. These results confirm that the magnetic moment originates from the Mn cations and are in agreement with the bulk magnetometry results showing full magnetic moment of the $La_{0.8}Sr_{0.2}MnO_3$ film: since the spectra are collected in TEY, which has a sensitivity of around 3-5 nm due to the limited electron mean free path [171], a constant XMCD signal with thickness confirms that each added layer is magnetic. The $La_{0.45}Sr_{0.55}MnO_3$ sample series was measured at the SIM beamline, with the exception of the 5 uc, measured at X-Treme. The shape of the main peak at 642 eV is an indication that the films are stoichiometric and fully oxidized, with Mn present in a mixed 3+/4+ valence state [232]. Figure 4.10(d) shows the corresponding XMCD spectra. Consistent with the magnetometry results, the 0, 1 and 2 uc samples show no XMCD signal, while the 5 uc sample displays a strong magnetic dichroic response, but with an amplitude that is lower than the case of the $LaMnO_3$ series. These results support the conclusion that the magnetic signal arises from the top two unit cells and is slightly reduced by the zero XMCD signal contribution from the antiferromagnetic $La_{0.8}Sr_{0.2}MnO_3/La_{0.45}Sr_{0.55}MnO_3$ films underneath.

Magnetic exchange in these materials is generally understood in terms of orbital occupancy, according to the Goodenough-Kanamori rules [89, 90, 233]. In particular, doping and strain play fundamental roles in determining which of the spin exchange mechanisms, double exchange or superexchange, domi-

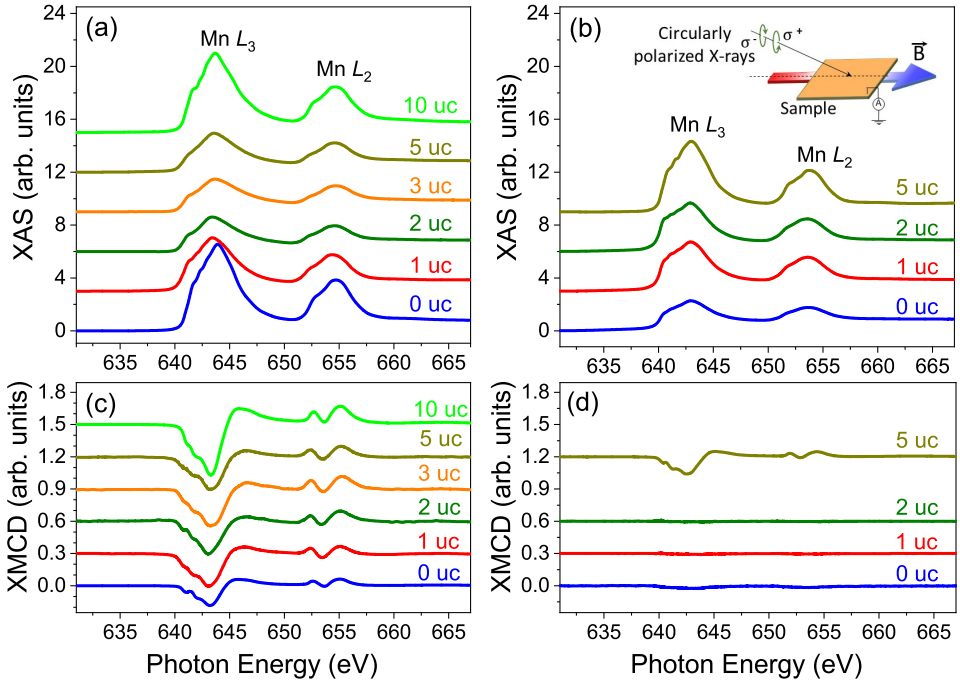

Figure 4.10: XAS spectra collected on $La_{0.8}Sr_{0.2}MnO_3$ films grown on (a) $LaMnO_3$ and (b) $La_{0.45}Sr_{0.55}MnO_3$ buffer layer. The corresponding XMCD spectra, normalized to the respective XAS peak value, are shown in (c) and (d). All spectra are shifted vertically for clarity of display. Figure taken from [203].

nates the magnetic interaction, since the orbital structure depends strongly on these degrees of freedom. Hence, in order to probe the orbital character of the heterostructures studied here, we have carried out x-ray absorption measurements with linearly polarized light, which probes the available density of states along the electric field direction [80]. The XAS spectra measured at 300 K, above the Curie temperature to avoid the magnetic contribution, are shown in Fig. 4.11(a) and (d) for the O K-edge and Mn L-edge, respectively.

The O K-edge shows the general shape typical for $La_{0.8}Sr_{0.2}MnO_3$, with pre-edge peaks (A, B) associated to O $2p$ orbitals hybridized with Mn $3d$, and higher energy peaks, C, D, associated with O $2p$ orbitals hybridized with La and Sr orbitals, respectively [232]. Of interest here are the pre-edge peaks, in the range 527-533 eV, which are argued to reflect more directly the unoccupied density of states of the Mn $3d$ states, since the excitation occurs at the oxygen site [234]. Two different assignments of these peaks to the Mn orbitals states have been presented in the literature, in one case where peak A is assigned to the partially filled $e_g^{\uparrow}$ band and peak B to transitions into empty $t_{2g}^{\downarrow}$ and $e_g^{\downarrow}$ states [119, 232, 235]; one other assignment ascribes peak A

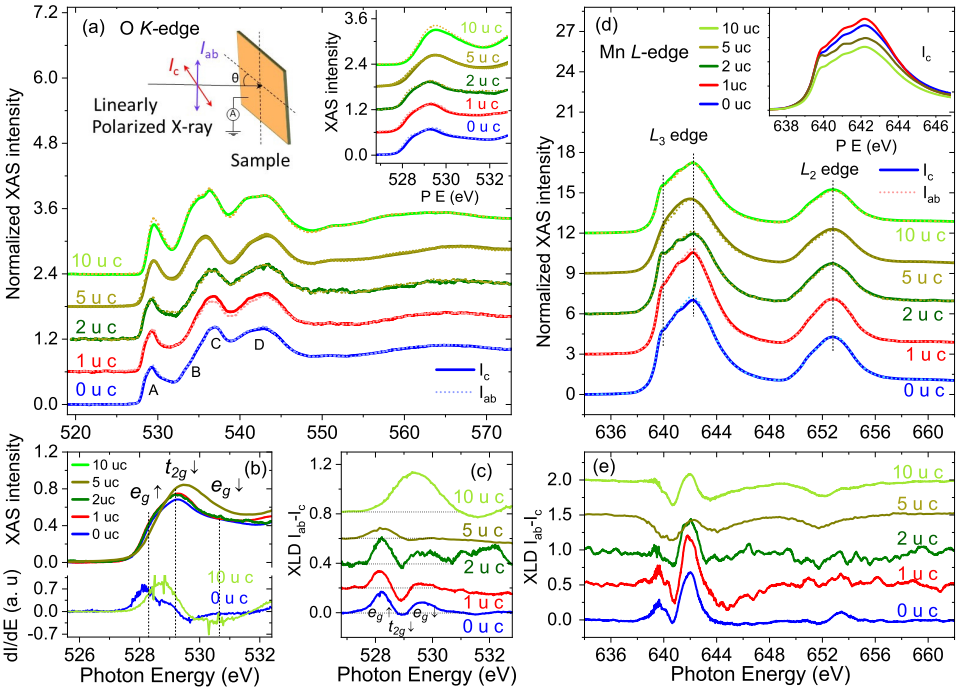

Figure 4.11: (a) Room temperature XAS spectra at O K-edge obtained with linearly polarized light for $La_{0.8}Sr_{0.2}MnO_3/La_{0.45}Sr_{0.55}MnO_3$. (b) Detail of the pre-edge feature of the O spectra highlighting the transition associated with the O 2p-Mn 3d hybridized states. The derivatives of the 1, 10 uc spectra are also shown to highlight the peak position. (c) O K-edge XLD spectra of the $La_{0.8}Sr_{0.2}MnO_3$ films. (d) XAS spectra at the Mn L-edge collected with vertical (I_{ab}) and horizontal (I_c) light polarization. Inset shows a plot of all spectra at the L_3 edge. (e) Mn L-edge XLD spectra. Figure taken from [203].

to the partially filled $e_g^{\uparrow}$ band and empty $t_{2g}^{\downarrow}$ and peak B to transitions into $e_g^{\downarrow}$ states [236]. Our results are not able to address this controversy, however, we can extract the following conclusions from our data:

(i) One finds a shift to higher energies of the O pre-edge features associated with the $e_g^{\uparrow}$ band when going from the $La_{0.45}Sr_{0.55}MnO_3$ buffer layer to $La_{0.8}Sr_{0.2}MnO_3$ [Fig. 4.11(b)]; this is expected based on band filling, since with decreasing hole doping the electron occupation of the $e_g^{\uparrow}$ band increases, resulting in a decrease in the unoccupied density of states.

(ii) One finds that the leading edge of the x-ray absorption spectra occurs at lower energies for the in-plane polarized light, while the difference is significantly reduced for the 5 and 10 uc films; this can be more easily seen as a shift to higher energies of the spectral weight of the linear dichroic signal at the $e_g^{\uparrow}$ band, Fig. 4.11(c). This behavior indicates a re-

duction in the asymmetry of the occupancy of in-plane and out of plane orbitals at larger $La_{0.8}Sr_{0.2}MnO_3$ thicknesses, consistent with what is expected for the ferromagnetic state [237]. We note that, given that both layers have the same in-plane lattice parameter and given that the lattice parameter of $La_{1-x}Sr_xMnO_3$ changes with Sr doping, the $La_{0.45}Sr_{0.55}MnO_3$ buffer layer and the $La_{0.8}Sr_{0.2}MnO_3$ top layer are subjected to different in-plane strains. Taking the pseudo-cubic lattice parameter for $La_{0.45}Sr_{0.55}MnO_3$ and $La_{0.8}Sr_{0.2}MnO_3$ as 3.84 Å and 3.89 Å, respectively [94, 95, 121], one obtains in-plane strains of –1.69% and –0.39%, respectively. The role of strain is that of shifting the relative energy position of the two $e_g^{\uparrow}$ orbitals, z^2 and x^2-y^2, with compressive (negative) strain favouring the x^2-y^2 orbitals, in agreement with the experimental observations and consistent with the magnetic behavior, i.e., an antiferromagnetic in-plane metallic A-type state for $La_{0.45}Sr_{0.55}MnO_3$ and a ferromagnetic isotropic state for $La_{0.8}Sr_{0.2}MnO_3$.

(iii) One finds that up to 2 uc $La_{0.8}Sr_{0.2}MnO_3$ the XAS spectra remains essentially unchanged (although in these cases, a significant signal contribution from the underlying $La_{0.45}Sr_{0.55}MnO_3$ layer should be present), while for 5 uc, which is expected to have a strongly reduced $La_{0.45}Sr_{0.55}MnO_3$ signal contribution due to limited electron escape depth, a strong modification in the XAS spectra is observed, starting to resemble the 10 uc $La_{0.8}Sr_{0.2}MnO_3$ spectra.

(iv) The integral of the linear dichroism over the Mn $L_{2,3}$ edge, Fig. 4.11 (e), gives the preferred orbital orientation according to the linear dichroism sum rule $D_L = \int_{L_2+L_3}(\mu_{ab}-\mu_c)dE / \int_{L_2+L_3}(2\mu_{ab}+\mu_c)dE = \langle\sum(l_z^2-2)\rangle_i/4$, where μ_{ab} and μ_c are the x-ray absorption along the in-plane and out of plane directions, respectively, $l_z = 0$ is the quantum orbital number for the $3d_{3z^2-r^2}$ orbital, and $l_z = 2$ for $3d_{x^2-y^2}$ [238]. A positive value for D_L indicates a preferential occupation of the x^2-y^2 orbitals. Based on this sum rule, one finds, qualitatively, that for 0-2 uc $La_{0.8}Sr_{0.2}MnO_3$ the in-plane x^2-y^2 orbitals are preferentially occupied, while for the 5, 10 uc, there is a change in orbital character to a predominant occupation of the out of plane orbitals. The changes in orbital character are in general qualitative agreement with the O pre-edge spectral features.

These observations, in combination with the magnetic behavior, suggest that $La_{0.8}Sr_{0.2}MnO_3$ films up to 3 uc thickness have a similar electronic and magnetic structure as the $La_{0.45}Sr_{0.55}MnO_3$ buffer layer, characterized by a preferential occupation of the x^2-y^2 orbitals, large in-plane conductivity, and an A-type antiferromagnetic ordering. At larger thicknesses, a transition to a preferential occupation of out of plane orbitals occurs, where a spectrum similar to that reported for the fully polarized ferromagnetic state is observed [239], even if an equal population of both in-plane and out of plane orbitals were expected [240].

4.3.3 Magnetic domains in $La_{0.8}Sr_{0.2}MnO_3/La_{0.45}Sr_{0.55}MnO_3$ bilayers

It remains still an open question whether the $La_{0.8}Sr_{0.2}MnO_3$ films with thickness below 4 uc couples antiferromagnetically to the $La_{0.45}Sr_{0.55}MnO_3$ buffer layer or not, although the results presented in the previous section seem to suggest an antiferromagnetic coupling to the buffer layer. To address this question, we have measured the local magnetic state across the sample series using XPEEM with linear (circular) polarised light to probe antiferromagnetic (ferromagnetic) order in the system. To ensure that the image contrast was magnetic, we present the difference of magnetic images taken at two energies where the magnetic contrast has opposite signs.

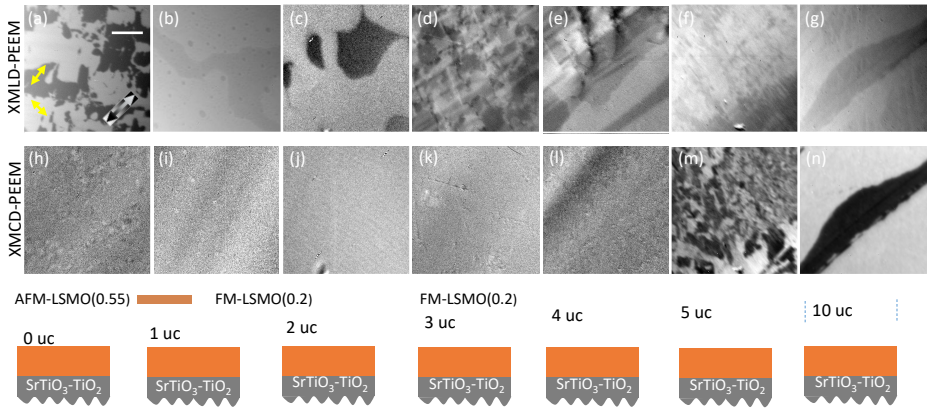

Figure 4.12: XMLD contrast $[(I_{ab}\text{-}I_c)/(I_{ab}+I_c)]$ of (a) 15 uc $La_{0.45}Sr_{0.55}MnO_3$ buffer layer and as a function of thickness of $La_{0.8}Sr_{0.2}MnO_3$ layer (b-g). XMCD contrast $[(C^+\text{-}C^-)/(C^++C^-)]$ of (h) 15 uc $La_{0.45}Sr_{0.55}MnO_3$ buffer layer and as a function of thickness of $La_{0.8}Sr_{0.2}MnO_3$ layer (i-n). Schematic show the variation in the exchange coupling and spin configuration of $La_{0.8}Sr_{0.2}MnO_3$ layer as the function of thickness. The arrow in (a) indicates the direction of the incoming x-rays and of the magnetic contrast. Figure taken from [205].

In Fig. 4.12 we show the local magnetic structure across the sample series measured at ≈80 K, specifically, XMLD and XMCD images taken at the same exact sample position as a function of the $La_{0.8}Sr_{0.2}MnO_3$ thickness. The results show for all samples the presence of XMLD contrast, while XMCD contrast is observed only for thicknesses above 3 uc. This result directly demonstrates that samples 1 to 3 uc exhibit no local ferromagnetic domains and that therefore they are in an antiferromagnetic state. As ferromagnetic state starts establishing into the heterostructure, these antiferromagnetic domain states are transforming to a complex irregular domain state as shown in Fig. 4.12 for 3 to 5 uc. For 10 uc thickness, the signal

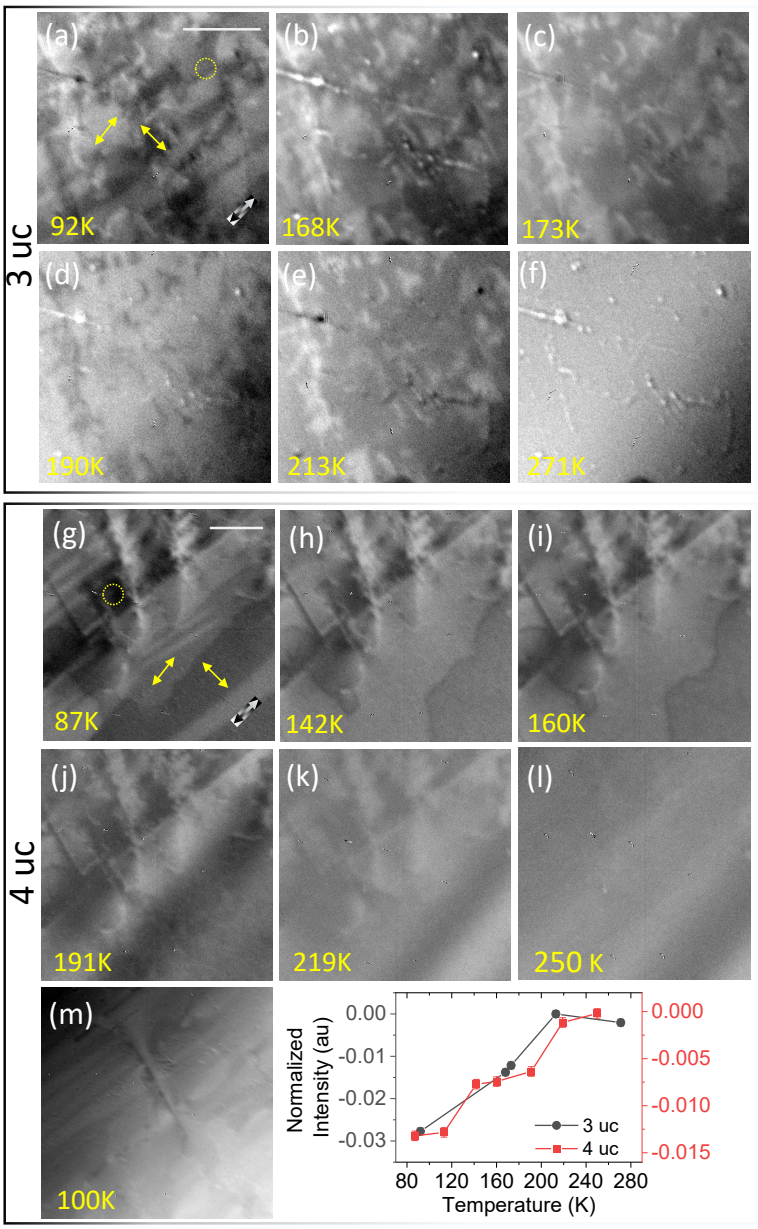

Figure 4.13: Variation of the normalized XMLD PEEM contrast at E_1 = 643.35 eV as a function of temperature for 3 uc $La_{0.8}Sr_{0.2}MnO_3$ grown on 15 uc $La_{0.45}Sr_{0.55}MnO_3$ (a-f), image in (d) recorded at energy 642.0 eV just to represents the XMLD contrast reversal. Variation of the normalized XMLD PEEM contrast for 4 uc (g-n) at E_1 = 642.35 eV, which is background corrected by image recorded at E_2 = 641.0 eV. (o) represent the normalized intensity (calculated from the region marked by yellow circle) as function of temperature for 3 and 4 uc. Scale bar in the images is equivalent to 5 μm. Figure adapted from [205].

arising from the bottom antiferromagnetic layers is expected to be weak due to the limited escape depth of the secondary photoelectrons and the XMLD image, which matches the XMCD image, in fact originates from the ferromagnetic domain structure (the XMLD signal being sensitive to the square of the magnetization).

To further confirm that the XMLD contrast is due to antiferromagnetic domains, we carried out measurements as a function of temperature for 3 and 4 uc. Variation of the normalized XMLD PEEM contrast $[(I_{ab}\text{-}I_c)/(I_{ab}+I_c)]$ with temperature for 3 (V/H at 643.35 eV) and 4 uc (V/H at 641.0 eV - H/V at 642.35 eV) are presented in Fig. 4.13. One observes that with increasing temperature the domains with white contrast decrease in size, until the magnetic contrast vanishes at 271 K for 3 uc and 250 K for 4 uc [Fig. 4.13(o)]; given the systematic temperature error of about 20 K between sensor and sample surface, this value agrees well with the critical value estimated from the resistivity peak in Fig. 4.9(d) at 290 K and 270 K respectively demonstrating that the XMLD originates from the antiferromagnetic domain structure [203].

4.4 Discussion

The two different buffer layers lead therefore to two distinct magnetic behaviors for the top $La_{0.8}Sr_{0.2}MnO_3$ films. In the case of $LaMnO_3$, the $La_{0.8}Sr_{0.2}MnO_3$ films are fully spin polarized starting from 1 uc, with a magnetic critical temperature that is much higher than that of the single buffer layer, indicating the presence of a strong magnetic coupling dominated by the top $La_{0.8}Sr_{0.2}MnO_3$. Since the $LaMnO_3$ film is insulating, we attribute the magnetic coupling with the buffer layer to be dominated by spin exchange at the interface between the two systems. In the case of the $La_{0.45}Sr_{0.55}MnO_3$ buffer layer, we find that the $La_{0.8}Sr_{0.2}MnO_3$ film adopts the metallic antiferromagnetic state of the buffer layer up to a thickness of 3-4 uc and a sudden transition to a ferromagnetic state above this thickness, manifest in the linear dichroic data by a sudden modification of the electronic structure from 2 to 5 uc films and by the XPEEM results, showing antiferromagnetic domains for all the sample series. The magnetic nature of the contrast is confirmed through the temperature dependent study. We conclude that the $La_{0.8}Sr_{0.2}MnO_3$ follows the A-type antiferromagnetic order of the buffer layer up to 4 uc, where a net magnetic moment is observed by the SQUID measurements. We explain the interfacial antiferromagnetic metallic state as driven by extended delocalized charge transfer between the $La_{0.45}Sr_{0.55}MnO_3$ and the $La_{0.8}Sr_{0.2}MnO_3$, which operates up to three unit cells beyond the interface. At larger thicknesses, the $La_{0.8}Sr_{0.2}MnO_3$ adopts its ferromagnetic ground state, with a full bulk moment and critical temperature independent of the underlying manganite film. In both instances,

the $La_{0.8}Sr_{0.2}MnO_3$ films are fully magnetically polarized starting from the single unit cell. One possible common mechanism driving the magnetic behavior of the top $La_{0.8}Sr_{0.2}MnO_3$ films toward bulk behavior may be the onset of oxygen octahedral rotations promoted by the $LaMnO_3$ buffer layer and the first 3-4 unit cells $La_{0.8}Sr_{0.2}MnO_3/La_{0.45}Sr_{0.55}MnO_3$, which agrees with the lengthscale for bond angle relaxation of the oxygen octahedral tilt of 4 unit cells found for $LaMnO_3/SrTiO_3$ superlattices [241].

4.5 Conclusions

In conclusion, we have studied the evolution of the magnetic moment of ultrathin $La_{0.8}Sr_{0.2}MnO_3$ films grown on insulating $LaMnO_3$ and conducting $La_{0.45}Sr_{0.55}MnO_3$ buffer layers. Although both systems are nominally antiferromagnetic, we find a significant magnetic moment in the $LaMnO_3$ buffer layer, a result similar to that reported before in the literature. We proved that Sr interdiffusion from the substrate, as well as Ca and Si impurities, is responsible for a slight hole doping of the $LaMnO_3$ films which brings the system in an insulating ferromagnetic state. For the $La_{0.8}Sr_{0.2}MnO_3/LaMnO_3$ series, a metallic state and bulk-like magnetic moment are observed for $La_{0.8}Sr_{0.2}MnO_3$ thicknesses down to 1 uc. The two layers are magnetically coupled, but the magnetic properties are dominated by the top layer, including bulk-like magnetic moments and high critical temperature that do not correspond to those of the bare $LaMnO_3$ film. For the case of $La_{0.8}Sr_{0.2}MnO_3/La_{0.45}Sr_{0.55}MnO_3$, we observe an antiferromagnetic ground state up to 3 uc, above which a ferromagnetic ground state for the subsequent $La_{0.8}Sr_{0.2}MnO_3$ layers emerges. The x-ray absorption spectroscopy results show a sudden change in the electronic structure from 2 to 5 uc consistent with the observed change in the magnetic properties. The antiferromagnetic coupling to the buffer layer is confirmed by our XPEEM measurements, showing antiferromagnetic domains up to 4 uc thick $La_{0.8}Sr_{0.2}MnO_3$; the temperature dependence study confirms that the XLD contrast observed in the 3 and 4 uc samples is magnetic. We have shown that the properties of ultrathin $La_{0.8}Sr_{0.2}MnO_3$ films can be tailored by a suitable choice of buffer layers to yield bulk-like magnetic polarization and high critical temperatures, down to the unit cell thickness range. Our results are highly relevant for device applications, since they provide an approach to using the same material platform to create $La_{0.8}Sr_{0.2}MnO_3$ films that are fully spin polarized down to 1 uc either on conducting buffer layers ($La_{0.45}Sr_{0.55}MnO_3$) or on magnetic but insulating layers ($LaMnO_3$). We anticipate as well that the results found here may be applicable to the wider doping range where $La_{1-x}Sr_xMnO_3$ is in a ferromagnetic state, including for optimally doped $La_{1-x}Sr_xMnO_3$, and to the wider manganite perovskite family.

5

Direct Imaging of the Magnetoelectric Coupling in $BaTiO_3/La_{0.9}Ba_{0.1}MnO_3$ Multiferroic Heterostructures[1]

5.1 Introduction

Among the complex oxides, the doped manganites have been extensively studied due to the wide range of functional properties that they exhibit as a function of doping, temperature, pressure, and magnetic and electric fields [243]. One of the most studied manganites is the Sr-doped $LaMnO_3$ due to its high Curie temperature (above room temperature at 30% Sr doping) [121, 244]. One challenge is that its magnetic and electrical properties tend to degrade when grown as thin film, although strategies for circumventing this issue have been proposed in chapter 4. The Ba-doped compound has been less extensively studied; however, it has been shown that the Curie temperature in this system increases with decreasing thickness under tensile strain [18, 56], which makes it a promising candidate for ultrathin device

[1] This chapter is derived from the paper submitted for publication in Journal of vacuum science and technology A [242]. My contribution to this study was the growth and SQUID and AFM characterization of the sample and the writing of the ferroelectric domains. The PFM characterization was performed by Dr. C. Lichtensteiger and L. Tovaglieri at the university of Geneva. The e-beam lithography was carried out by Dr. Carlos A. F. Vaz, while the transport measurements were done by Dr. G. Panchal. The XPEEM data collection, process and analysis were performed by me and Dr. Carlos A. F. Vaz.

applications. Furthermore, the few studies on ferroelectric field effect devices involving this material that have been carried out [71, 72, 245, 246] show a behavior as a function of the ferroelectric polarization direction that is opposite to the $La_{0.8}Sr_{0.2}MnO_3$ case [60], where an increase of the magnetic moment is observed by switching the system from a hole depletion to hole accumulation state [246].

In this chapter we address a related aspect, namely, we image the magnetic state of a manganite-ferroelectric system, $BaTiO_3/La_{0.9}Ba_{0.1}MnO_3$, for different local states of the ferroelectric polarization using x-ray photoemission electron microscopy (XPEEM). The approach is to consider a chemical doping near the boundary separating different magnetic ground states of the system to achieve high susceptibility to external applied fields. We locally write micrometer-sized ferroelectric domains by applying different voltage amplitudes to follow the evolution of the magnetic and electronic state with the ferroelectric polarization direction. The aim is to create ferroelectric domains with the polarization pointing up or down, where charge screening from the $La_{0.9}Ba_{0.1}MnO_3$ results, respectively, in the accumulation or depletion of hole carriers at the interface. We find a decrease in the magnetic contrast when going from negative to positive writing voltages, consistent with the presence of a magnetoelectric effect through changes in the hole carrier density and in the equilibrium spin configuration.

5.2 Experimental details and sample characterization

In Fig. 5.1(a)-(c) we show the RHEED patterns of the $SrTiO_3$ substrate, $La_{0.9}Ba_{0.1}MnO_3$ and $BaTiO_3$ film surfaces after growth, respectively. The presence of sharp diffraction spots lying on an arc and of Kikuchi lines demonstrates that the films are epitaxial and have smooth, well ordered surfaces. In Fig. 5.1(d) we plot the RHEED intensity variation during the deposition of the $La_{0.9}Ba_{0.1}MnO_3$ layer; one finds a first regime where no clear oscillations are observed (associated with an overall decrease in the RHEED pattern intensity), followed by a second regime where oscillations associated with the successive completion of a unit cell layer are observed, indicating that the growth process proceeds layer-by-layer, which we use to monitor the film thickness in real time. For the $BaTiO_3$ layer we did not observe RHEED intensity oscillations during the film growth and the film thickness is estimated from the film evaporation rate measured immediately before growth. The thickness of the $BaTiO_3$ layer was chosen to still allow detection of the $La_{0.9}Ba_{0.1}MnO_3$ layer underneath with XPEEM, which has a probing depth of the order of 3-5 nm. The sample is then post-annealed *ex situ* in a tube furnace in air at 600 ^{o}C for 6 hours to fully oxygenate the films. Atomic force microscopy shows that the surface is flat, but exhibit small features of

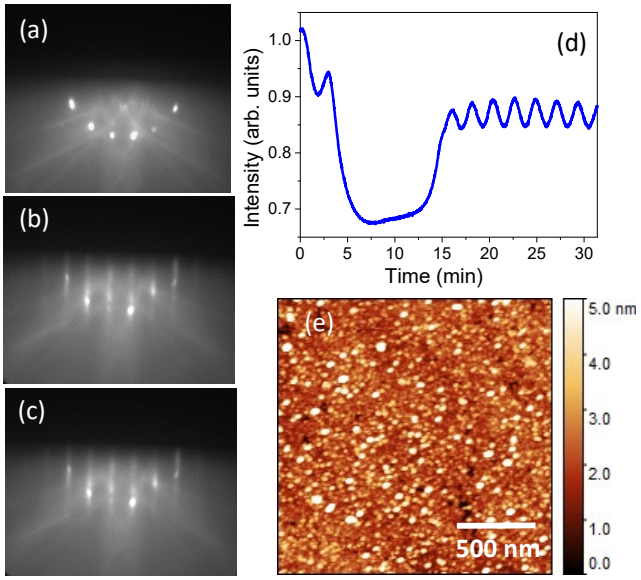

Figure 5.1: (a)-(c) RHEED pattern of the $SrTiO_3$ substrate, $La_{0.9}Ba_{0.1}MnO_3$ and $BaTiO_3$ layers, respectively. (d) RHEED intensity oscillations during the deposition of the first 10 uc of the $La_{0.9}Ba_{0.1}MnO_3$ layer. (e) Atomic force micrograph of the sample surface. Figure taken from [242].

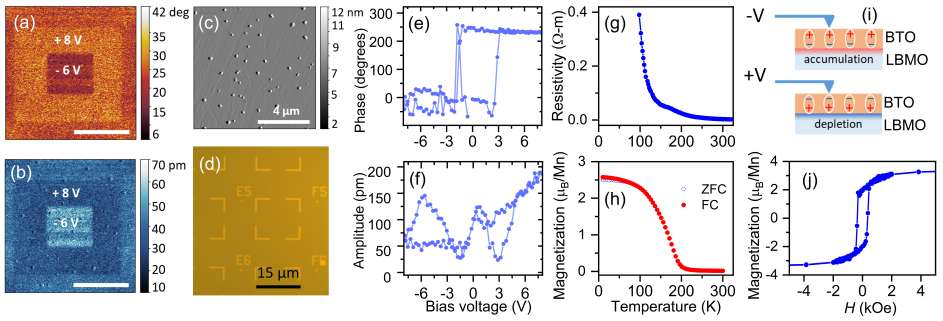

Figure 5.2: (a) PFM measurements showing the phase and (b) amplitude response of the $BaTiO_3$ layer after writing a larger square with +8 V and a smaller with –6 V. (c) AFM image of the sample surface. (d) Optical image of the sample showing the gold marker structures used to locate the areas written by PFM. (e,f) Local *P-E* loops showing the local ferroelectric response of the $BaTiO_3$ film. (g) Resistivity as a function of temperature showing a metal to insulator transition at around 170 K. (h) FC and ZFC magnetization curves measured under a magnetic field of 1 kOe. (i) Schematic representation of the depletion and accumulation states corresponding to the two directions of the ferroelectric polarization. (j) Magnetic hysteresis curve at 20 K. Figure taken from [242].

up to a few 10s of nm in height, resulting in a mean square roughness of 1 nm, see Fig.5.1(e).

In order to easily locate specific regions in the sample, we have deposited gold markers on the $BaTiO_3$ top layer using a one step e-beam lithography procedure. Specifically, a negative photoresist mask was prepared by exposure of a polymethylmethacrylate (PMMA) film to a 100 keV focused electron beam (Vistec EBPG5000Plus), development in a 7:3 isopropanol:water solution and thermal evaporation of 13 nm Au/3 nm Cr bilayer followed by metal lift-off in acetone. An optical image of the fabricated structures is presented in Fig. 5.2(d). On several such areas of the sample, we wrote ferroelectric patterns using the conducting tip of an atomic force microscope operating in piezoresponse force microscopy (PFM) mode (Veeco Dimensions 3100), as schematically shown in Fig. 5.2(i). Subsequent ferroelectric characterization was performed at room temperature with an Oxford Instruments MFP-3D atomic force microscope at the University of Geneva. For these measurements, the piezoresponse force phase and amplitude signals were recorded in a single frequency vertical PFM mode using Bruker MESP-V2 tips with an excitation voltage of 500 mV and drive frequencies in the range from 300-400 kHz. For these measurements, we wrote a sequence of square-in-a-square pattern using opposite voltages in order to determine the default polarization state of the $BaTiO_3$ film and to confirm that the voltages used to write the patterns were sufficient to switch the ferroelectric polarization. These results are presented in Fig. 5.2(a,b) for two voltages of opposite sign, –6 V and +8 V, together with the local *P-E* response of the $BaTiO_3$ film in Fig. 5.2(e,f). A first observation is that these voltages correspond to nominally very large electric fields, however, we expect that only a small fraction of the field is applied to the $BaTiO_3$ film due to tip-sample and lead contact losses and to tunneling and capacitive currents that prevent the electric field from building up at the dielectric layer. The PFM phase signal for the –6 V has a response closer to that outside the written area, indicating that the as-grown polarisation state of the $BaTiO_3$ points towards out of the plane. However, we find a slight variation in the signal amplitude for the areas written with +8 V and –6 V, which may point to the presence of injected charges. The change in phase, of about 30°, is much smaller than the expected 180°. We interpret these results as indicating that the 12 uc $BaTiO_3$ film is a defective ferroelectric, whereby the $BaTiO_3$ polarization either does not completely switch or immediately back-switches after application of the positive bias voltage, resulting in a mixed domain state where only a small fraction of the written area remains in the switched down state [247, 248]. Despite this, local *P-E* loops show a response characteristic of a ferroelectric system, Fig. 5.2(e,f), confirming that locally the 12 u.c. $BaTiO_3$ is ferroelectric.

The sample resistivity was measured in a two-contact geometry in a home-built setup, using spring contacts. Since the current-voltage (*I-V*)

characteristics were non-linear at low bias (possibly due to tunneling across the ferroelectric layer), we took *I-V* measurements as a function of temperature and fitted the *I-V* curve between –18 and –2 V, where the variation is linear, to a linear curve and obtained the resistance from the slope. The resistivity ρ is estimated according to the relation $\rho = R\pi t/\ln(2s/a)$ [249], where R is the resistance, t the film thickness and $a \sim 10$ μm and $s = 3$ mm the contact separation and contact radius, respectively. A metal-to-insulator transition is observed at around 170 K and a strong insulating behavior at low temperatures [Fig. 5.2(g)], typical of thin manganite films and generally attributed to charge localization effects [228].

Bulk magnetometry measurements, shown in Fig. 5.2(h,j), include temperature dependent zero field-cooled (ZFC) and field-cooled (FC) magnetization (*M-T*) and magnetic hysteresis (*M-H*). The *M-T* curve shows that the critical temperature of the $La_{0.9}Ba_{0.1}MnO_3$ film is at around 200 K (compared to 162-185 K for the bulk) [18, 250, 251], while the *M-H* characteristic at 20 K shows that the magnetic film has a relatively small coercive field (350 Oe) and a zero-field extrapolated saturation moment of 3.2 μ_B/Mn, slightly smaller than the spin moment value of 3.9 μ_B/Mn.

X-ray photoemission electron microscopy (XPEEM) measurements were carried out at the SIM beamline of the Swiss light source (SLS), Paul Scherrer Institut (PSI), Switzerland, in two independent runs. We note that, given the limited probing depth of the secondary photoemitted electrons, in the range from 3-5 nm, and given the presence of about 4.8 nm $BaTiO_3$ top layer, the XPEEM measurements are sensitive to the topmost $La_{0.9}Ba_{0.1}MnO_3$ atomic layers in contact with the $BaTiO_3$ film. For the temperature dependent measurements, we calibrate the temperature scale in XPEEM using the value for the critical temperature obtained from SQUID magnetometry.

5.3 Results and discussion

An XPEEM image of the secondary electron photoemission yield of the area of interest, taken at the Mn L_3 peak (642 eV), is shown in Fig. 5.3(a). In this image, one can see the Au frame and next to it the areas where the electric field has been written as labeled. The lateral size of the written squares shown here is 2 μm and the voltage ranges from $\pm$2 V to $\pm$8 V; these are distinguished from the rest of the film due to slight changes in the photoemission yield, likely induced by modifications in the surface potential caused by the electric voltage writing process. The spatial resolution provided by XPEEM allow us to compare the local spectroscopy response at the O K-edge at different regions of the sample as shown in Fig. 5.3(c) for a pristine $BaTiO_3$ region, the areas written with +8 and –8 V, and at the small black dots visible in the image (averaged over three such dots). One sees that, while the spectra of the regions written with +8 V and the

pristine $BaTiO_3$ are similar, the spectrum of the region written with –8 V has a strongly reduced signal at the leading edge and an enhanced feature that matches that appearing at the black dots. The Mn L-edge signal in the –8 V region shows also that the oxidation state of $La_{0.9}Ba_{0.1}MnO_3$ is strongly reduced, pointing to the presence of oxygen vacancies induced by the large negative electric field. Hence, we conclude that the areas written with –7 V (in part) and –8 V corresponding to damaged areas due to electrical breakdown, where the photoelectron emission yield is strongly suppressed due to local charging and will be discussed in less detail (this local charging becomes less significant at the L_2 edge, where the photoemission intensity is lower, and at higher temperatures, where the sample conductivity increases).

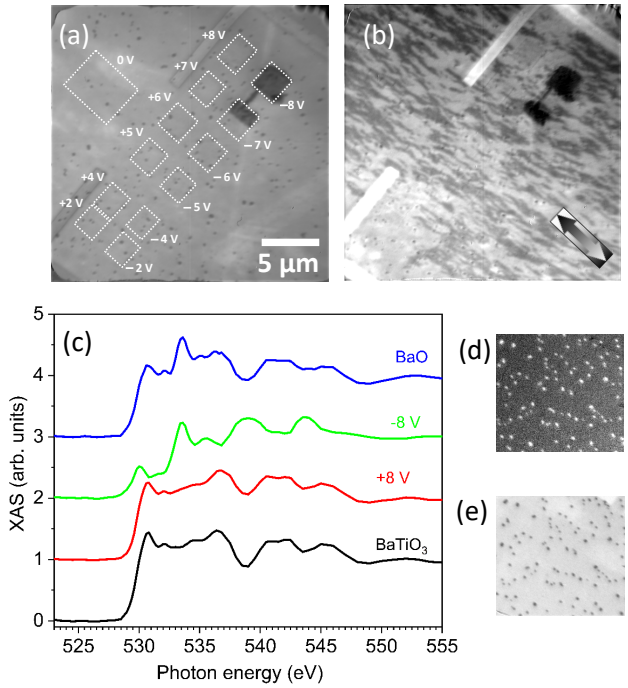

Figure 5.3: (a) Unpolarized XPEEM image showing the PFM-written patterns with the corresponding applied voltages (642 eV, 100 K). The dashed squares highlight the regions where the ferroelectric patterns have been written. The larger square corresponds to the area used for extracting the zero applied voltage spectra. (b) Magnetic contrast image of the sample in a multidomain state (642 eV, 100 K). The arrow shows the magnetic contrast direction. (c) O K-edge spectra taken at different areas of interest of the image shown in (a). (d) Ba contrast image obtained by division of two images acquired at the Ba M_5-edge and at the pre-edge. (e) Corresponding Mn elemental contrast image (division of L_3 edge and pre-edge images). The scale bar for the XPEEM images is given in (a). Figure taken from [242].

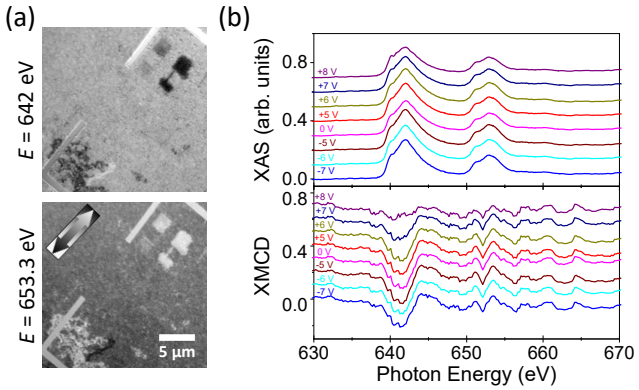

Figure 5.4: (a) Magnetic contrast image at 100 K taken at the L_3 (642 eV) and L_2 (653.3 eV) Mn edges. The arrow indicates the direction of the incoming x-rays and of the magnetic contrast. The XMCD contrast range is set to ±0.04. (b) polarization-averaged XAS and XMCD (normalized with respect to the XAS peak) spectra taken at 100 K for the different applied voltages, as labeled. Figure taken from [242].

The small dark dots appearing on the surface, also visible in the AFM image shown in Fig. 5.1(e), are Ba-rich as confirmed from a Ba elemental contrast image [Fig. 5.3(d)] and are explained to arise from Ba outdiffusion from the $BaTiO_3$ to the surface, also reported in literature [252]. Its oxygen spectrum is similar to that of $BaTiO_3$ except for the presence of a strong line at 533.6 eV [Fig. 5.3(c)]; we identify these features as BaO, although the spectra differs from that published in the literature [253], possibly due to a contribution from the $BaTiO_3$ background signal. We note that these topological features cancel out when dividing images taken with different circular light polarizations, where only differences due to magnetic contrast persist. Figure 5.3(e) shows an elemental contrast image at the Mn L_3 edge, showing that the Ba-rich islands are thick enough to strongly reduce the Mn signal underneath.

In Fig. 5.3(b) we present a magnetic XPEEM image of the sample in a multidomain state at 100 K, showing the presence of regions with white, dark and grey contrast. One observes a complex magnetic state characterized by many irregular, micrometer-sized striated domains. Although suggesting the presence of strong pinning sites for the magnetization, the magnetic hysteresis curve is square with a small coercive field [Fig. 5.2(f)], indicating that the magnetic anisotropy is weak.

To achieve a uniformly magnetized stated, the sample was cooled from room temperature down to the measurement base temperature of 100 K under a constant in-plane magnetic field of 300 ± 50 Oe set along the beam direction, generated by a permanent magnet placed next to the sample.

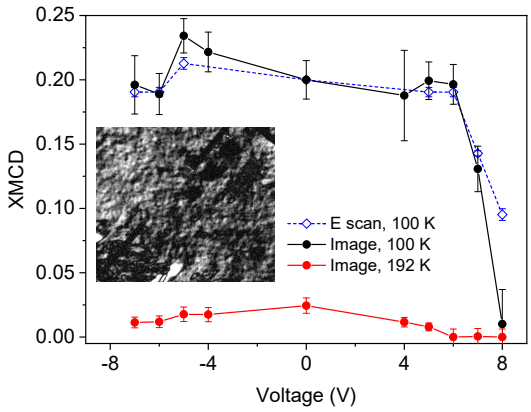

Figure 5.5: XMCD variation as a function of the writing voltage obtained from the amplitude of the XMCD spectrum signal (XMCD E scan) and from integrating the magnetic contrast over the written areas at 100 K and 192 K (average of the XMCD images at 642 eV and 653 eV after normalising each to the 0 V XMCD amplitude). Inset: Image of the absolute contrast used to extract the data at 192 K. Figure taken from [242].

The corresponding magnetic contrast images taken at the Mn L_3 and L_2 edges at energies where the XMCD values have opposite signs, are shown in Fig. 5.4(a). The image contrast is inverted between the two energies, confirming that the observed contrast is magnetic.

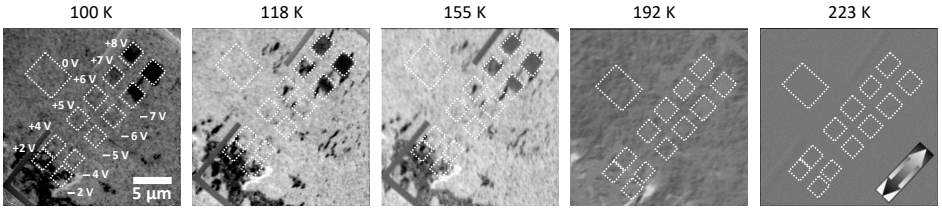

Figure 5.6: Magnetic contrast as a function of temperature. The images shown here are the difference between images taken at the Mn L_3 (642 eV) and L_2 (653.3 eV) edges. The arrow on the top right image indicates the direction of the incoming x-rays and of the magnetic contrast. The XMCD contrast range is set to ±0.04 for all images. Figure taken from [242].

To quantify the magnetic changes of the written areas we extract the local x-ray absorption and XMCD spectra integrated over the area where the electric field was applied to the $BaTiO_3$ layer, presented in Fig. 5.4(b) (100 K), where the –7 V spectra is extracted from the undamaged (stoichiometric) region and the 0 V spectra corresponds to the area of the sample where no voltage was applied, marked in Fig. 5.3(a). The XMCD spectra are normalized to the respective x-ray absorption peak maximum. The XAS

at 0 V shows the characteristic shape of stoichiometric $La_{0.9}Ba_{0.1}MnO_3$, with Mn present in mixed 3+/4+ state as found in $La_{1-x}Sr_xMnO_3$ [232]. Furthermore, we find no significant modifications of the spectral shape for the applied voltages in the range from –7 V to +7 V, indicating that the $La_{0.9}Ba_{0.1}MnO_3$ maintains its stoichiometry upon application of the electric field. Only in the +8 V case, we observe a slight increase in intensity at the spectral component at 640 eV. Interestingly, the amplitude of the XMCD is constant throughout the voltages applied, with the exception of +7 and +8 V, where it is strongly reduced, indicating a marked modification of the magnetic properties of the $La_{0.9}Ba_{0.1}MnO_3$ at +7 V and above (hole depletion state). In Fig. 5.5 we show the magnetic contrast variation as a function of the writing voltage obtained from the XMCD data shown in Fig. 5.4(a,b), in one case from integrating the magnetic contrast over the written areas excluding the regions containing BaO dots (labelled "Image, 100 K") and in the other case from the amplitude on the XMCD signal (labelled "E scan, 100 K"). One observes a sharp change in the magnetic contrast amplitude at +7 V, which we identify as the switching voltage for the ferroelectric polarization. For negative voltages the magnetic contrast is similar to that of the unwritten area, indicating that the pristine $BaTiO_3$ ferroelectric polarization points up (away from the $La_{0.9}Ba_{0.1}MnO_3$ interface), corresponding to the accumulation state at the $La_{0.9}Ba_{0.1}MnO_3$ interface. One also concludes that the ferroelectric polarization switches direction only at relatively large positive applied voltages, as is also confirmed by the results of the PFM measurements presented in Fig. 5.2(a,b).

In Fig. 5.6 we show magnetic contrast images at increasing temperature values, consisting of the difference between the images taken at the L_3 (642 eV) and L_2 (653.3 eV) Mn edges where the XMCD values have opposite signs. At 100 K, we find that the magnetic contrast is almost uniform over the probed area, except for a region showing smaller domains with opposite magnetic contrast on the bottom left of the images and for the two top left written areas (+7, +8 V), which exhibit a lower magnetic contrast. One observes, however, local fluctuations in the magnetic contrast within submicrometer length scales. Compared to the magnetic image at 118 K, the contrast in this image seems to be inverted; this is however an artifact due to the fact that the photoemission yield is slightly reduced at the L_3 edge due to surface charging effects: Fig. 5.4(a) shows that the contrast at the L_3 edge is larger than at the L_2 edge. At 118 K we start to see small reversed magnetization domains, including in the region written with +6 V. With increasing temperature there is a decrease in the magnetic contrast, while at 192 K, the magnetic contrast reverses, indicating a switching of the magnetization from the original orientation, which could originate from a simple demagnetization process or due to small mangetic stray fields. At this temperature, the squares written with voltages between +6 and +8 V appear non-magnetic (i.e., have the same contrast as the non-magnetic gold marker)

indicating a reduced T_C for the down polarization state (hole depletion at the $BaTiO_3$ interface). This behavior is more clearly seen by looking at the absolute value of the magnetic contrast at this temperature, shown as inset to Fig. 5.5, showing more clearly the non-magnetic contrast against the magnetic background. The magnetic contrast voltage dependence is shown as red symbols, showing a drop to zero between +6 and +8 V. These results are the manifestation of a magnetoelectric coupling between the $BaTiO_3$ and $La_{0.9}Ba_{0.1}MnO_3$. Finally, at 223 K the magnetic contrast vanishes, corresponding to the onset of the paramagnetic state.

Hence, our results show that for voltages up to +6 V, the ferroelectric polarization is in the as-grown up state, corresponding to the accumulation of hole carriers at the $BaTiO_3/La_{0.9}Ba_{0.1}MnO_3$ interface, while for voltages above +6 V the ferroelectric polarization points down, resulting in the depletion of hole carriers from the interface, leading to a reduced magnetization and critical temperature compared to the accumulation state. This behavior is distinct to that found for $PZT/La_{0.8}Sr_{0.2}MnO_3$, where the accumulation state has a reduced saturation magnetization but a higher critical temperature [8, 145]. The reduction in the magnetic moment agrees, however, with previous results reported for $PZT/La_{0.9}Ba_{0.1}MnO_3/SrTiO_3$ based on magneto-optic measurements [246]. According to the $La_{1-x}Ba_xMnO_3$ phase diagram [18], the equilibrium state at low doping is that of a spin canted state, with a reduced net magnetic moment and a lower critical temperature [18, 250, 251]. Further, the role of tensile strain is to favour occupation of the x^2-y^2 orbitals and to enhance double-exchange and the ferromagnetic state [18]. In this scenario, the depletion of hole carriers reduces not only the critical temperature but would favour a spin-canted state with a reduced magnetization, while in contrast, the accumulation of hole carriers at the interface enhances double-exchange, favouring a ferromagnetic ground state.

5.4 Conclusions

We have observed, by directly imaging the local magnetic configuration using x-ray absorption microscopy, the changes in the magnetic state as a function of writing voltage in ultrathin $BaTiO_3/La_{0.9}Ba_{0.1}MnO_3$ multiferroic heterostructures. Local spectroscopy allow us to establish the voltage regime under which no damage to the structure occurs. Within this regime, we observe a drop in the magnetic contrast and increase in the magnetic critical temperature as the applied voltage exceeds a critical threshold, corresponding to the (partial) switching of the ferroelectric polarization of the $BaTiO_3$ layer to depletion state. The observed behavior contrasts with that observed in $Pb(Zr_{0.2}Ti_{0.8})O_3/La_{0.8}Sr_{0.2}MnO_3$, where an increase in the magnetic moment and decrease in the critical temperature are found, and suggests that the charge depletion state drives the system into a spin canted

magnetic configuration. The present works adds to our understanding of the mechanisms responsible for the strong magnetoelectric coupling in these types of complex oxide multiferroic heterostructures.

6

Interfacial Orbital and Spin Configuration in $BaTiO_3/La_{0.8}Sr_{0.2}MnO_3$ Heterostructures[1]

6.1 Introduction

The physical properties of the manganites are determined by the orbital occupancy and, in the specific, by the d orbitals: a preferential in-plane orbital occupation favours the hopping in the ab plane, favouring A-type antiferromagnetic spin alignment; in this configuration, the spins in the same ab plane are aligned parallel but they are antiparallel to the spins on the adjacent ab planes. When a transition to the ferromagnetic state occurs, the orbital occupation becomes more isotropic. As a consequence of the crystal field, in an octahedral environment the d orbitals are split in a triplet (t_{2g}) and a doublet (e_g) state; in thin films, the degeneracy is further broken by the strain induced by the substrate, which favours either in-plane or out-of-

[1]The samples deposition and the SQUID and transport characterization were performed by me. The AFM measurements were carried out at the university of Geneva by L. Tovaglieri and Dr. C. Lichtensteiger. The XAS measurements were performed at SIM beamline by me in collaboration with Dr. C. A. F. Vaz. The ARPES and XPS measurements were carried out at ADRESS beamline by me in collaboration with Dr. A. Husanu, who also trained me and supported me during the ARPES data analysis, Dr. F. Alarab and Dr. V. Strocov. The resonant reflectivity measurements were carried out at the RESOXS endstation at SIM beamline by me and Dr. C. A. F. Vaz with the support from Dr. U. Staub and Dr. E. Skoropata.

plane occupation for tensile and compressive strain, respectively [32,235,254]. In $LaMnO_3$, the Mn^{3+} ion is characterized by a half filled t_{2g} orbital and one electron in the e_g; the effect of hole doping is that of removing electrons from the outer e_g orbital. Hence, the electric and magnetic properties are strongly dependent on the e_g states. In $La_{0.8}Sr_{0.2}MnO_3/BaTiO_3$ heterostructures, the ferroelectric polarization of the $BaTiO_3$ results in the interfacial $La_{0.8}Sr_{0.2}MnO_3$ hole accumulation or depletion state according to the direction of the ferroelectric polarization. In the accumulation state, the displacement of the O anion towards the $La_{0.8}Sr_{0.2}MnO_3$ results in a compressive force acting out-of-plane and hence in a contraction of the c axis, favouring the occupation of the in-plane orbital and, consequently, interfacial A-type antiferromagnetism. In the depletion state instead, the oxygen in the BaO layer is pushed away from the interface, resulting in a preferential out-of-plane occupation [74,75]. The same mechanism was observed with soft x-ray angle resolved photoemission spectroscopy on 0.33 doped $La_{1-x}Sr_xMnO_3$ [77].

The understanding of the electronic properties, which are strongly correlated to the Fermi surface topology and to the band structure, has been fundamental to explain several phenomena in condensed matter physics. In this sense, angle-resolved photoemission spectroscopy (ARPES) is a unique tool capable to map the reciprocal space and to obtain the band structure. It allows one to probe selected orbitals and to extract information on the electronic density of states thanks to the ARPES selection rules [175,182–184], differently from other measurement techniques (such as Hall measurements) which probes the total number of carriers. Here, our goal is to link the band structure and the orbital state to the magnetic configuration of $La_{0.8}Sr_{0.2}MnO_3/BaTiO_3$ heterostructures for the two directions of the ferroelectric polarization of the $BaTiO_3$ layer. We take advantage of synchrotron-based soft x-ray ARPES (SX-ARPES) to probe the $e_{g(x^2-y^2)}$-derived hole and $e_{g(3z^2-r^2)}$ electron band structure, while the magnetic profile is studied with x-ray resonant reflectivity (XRR), which has the advantage of combining x-ray absorption spectroscopy and scattering techniques, allowing us to determine the magnetic moment profile across the film thickness.

6.2 Experimental details

The samples are grown on $SrTiO_3(001)$ substrates which were chemically treated with a $HCl:HNO_3$ solution and annealed to 1000 °C in air to obtain a single TiO_2-terminated surface [159,160]. Three different samples are studied here: a reference sample, consisting of 11 unit cell (uc) $La_{0.8}Sr_{0.2}MnO_3$ on TiO_2-terminated $SrTiO_3(001)$, and two $BaTiO_3/La_{0.8}Sr_{0.2}MnO_3$ heterostructures, the first deposited on the TiO_2-terminated substrate as obtained after the chemical etching and annealing, the other grown on a SrO-terminated

$SrTiO_3$ substrate. It was shown that the substrate termination propagates through the heterostructure, resulting in different terminations of the $BaTiO_3$ layer and hence opposite ferroelectric polarization [Fig. 6.1(c)] [76]. In order to obtain SrO termination, we simultaneously deposit Sr and Ti onto the $SrTiO_3$ substrate: the RHEED intensity of the secondary spots shows a maximum in the intensity when the surface is SrO-rich because of the higher form factor of Sr with respect to Ti [255]. The $SrTiO_3$ layer is deposited at 700 °C while the substrates are held at 720 °C during the $La_{0.8}Sr_{0.2}MnO_3$ deposition; the $BaTiO_3$ layers were grown at 680 °C. For each layer, the oxygen partial pressure was $4 \pm 1 \times 10^{-7}$ mbar. The samples in this study consist of heterostructures of 11 uc thick $La_{0.8}Sr_{0.2}MnO_3$ and a 4 uc $BaTiO_3$ on the top of it, as represented in the schematics in Figure 6.1(c). Two different samples grown on substrates with different terminations are investigated, namely, TiO_2 and SrO-terminated $SrTiO_3$, resulting in two opposite ferroelectric polarization of the $BaTiO_3$. In particular, TiO_2-terminated $SrTiO_3$ favours a ferroelectric polarization pointing towards the interface, resulting in the $La_{0.8}Sr_{0.2}MnO_3$ in hole depletion state at the interface; the opposite is expected for the SrO termination [76]. In the following, the two samples will also be referred to as accumulation and depletion state. In Fig. 6.1(a) we show the RHEED patterns for the $SrTiO_3$ substrates, after the deposition of the $La_{0.8}Sr_{0.2}MnO_3$ layer and after the $BaTiO_3$ layer is grown, demonstrating epitaxial growth and well ordered surfaces, as also shown by the observation of RHEED intensity oscillations during growth shown in Fig. 6.1(b) characteristic of layer-by-layer growth, and by the atomic force microscopy (AFM) measurements shown in Fig. 6.1(d,e). In particular, one observes the atomic steps from the substrate as a further confirmation of very smooth surfaces. The $SrTiO_3$ deposition induces a small roughness on the surface, as indicated by the appearance of elongated dots in the RHEED pattern. Nonetheless, the deposition of the $La_{0.8}Sr_{0.2}MnO_3$ layer improves the surface quality, resulting in a sharp interface with the $BaTiO_3$, as shown by the RHEED patterns. After the growth, the samples are annealed in air at 600 °C for 6 hours to fully oxygenate the films.

X-ray absorption spectroscopy (XAS) measurements were carried out at the SIM beamline with the signal collected in total electron yield (TEY) mode, which has a high surface sensitivity due to the limited mean free path of the electrons in solid materials. Before each magnetic XAS measurement, a saturation field of 1 kOe was applied to the sample and the measurements were performed under 200 Oe magnetic field. We have collected XAS spectra with circularly left and right polarized light, from which we obtain the unpolarized (average) spectra and the x-ray magnetic circular dichroism (XMCD) spectra (difference). The latter are normalized by dividing it by the L_3 peak intensity of the respective average XAS spectrum to give the dichroic signal as percentage of the average XAS spectrum. The SX-ARPES measurements were performed at the ARPES endstation of the advanced resonant spec-

troscopies (ADRESS) beamline at SLS [202], which exploits soft x-rays to probe the band structure of the materials, with the advantage of enhancing the photoemission from the selected element by a factor 2 or 3 when tuned to an absorption edge. XRR measurements were carried out at SIM beamline using the resonant x-ray scattering (RESOXS) endstation. The reflectivity scans are obtained by tuning the photon energy to the Mn L_3 edge, i.e., at 642 eV, and collecting the reflected signal as a function of the angle of incidence θ varying between 0 and 80 degrees; the asymmetries are obtained by calculating the normalized difference of the reflectivity scans carried out with circular positive (C^+) and negative (C^-) polarizations [(C^+-C^-)/(C^++C^-)]. Two different energy scans are collected by fixing the angle at 5 and 40 degrees with two opposite light polarizations and varying the energy across the $L_{2,3}$ edges; the x-ray magnetic circular dichroism (XMCD) is calculated as the normalized difference between the spectra obtained with the two light polarizations. The scans are simulated using the Dyna software [195], which requires as input the real and imaginary parts of the scattering factors as well as the magnetic scattering factor of the magnetic layer, as mentioned in section 6.3.2. The non resonant parts of the scattering factors are extracted by the NIST tabulated values [196], while the magnetic part and resonant part is obtained by the unpolarized XAS spectra and the XMCD.

6.3 Results

Figure 6.2(a) shows the transport properties of the two samples with different terminations. The peak in resistivity corresponds to the metal-to-insulator transition typical of colossal magnetoresistance manganites, occurring in proximity to the magnetic critical temperature and generally attributed to the onset of extended electron hopping due to the spin alignment below T_C. As expected, the resistivities are quite different for the two samples, with a higher (lower) value for the sample in depletion (accumulation) state. The metal-to-insulator temperature (T_{MIT}) shows also the expected behavior, with a lower transition temperature in the accumulation state, in agreement with the literature [8]. In Fig. 6.2(b) and (c) we show the bulk magnetometry measurements for the two samples. The *M-T* overall behavior agrees well with the expected interfacial magnetic state: the Curie temperature follows the behavior observed with transport properties, showing a lower T_C and higher magnetization for the sample in depletion state; the saturation moment, extrapolated at zero field from the *M-H* hysteresis loops, is higher in interfacial depletion than in accumulation of holes by about 15%, in agreement with previous results [8]. Specifically, a saturation moment of $m_{TiO_2} = 2.6\ \mu_B/Mn$ and $m_{SrO} = 2.3\ \mu_B/Mn$ are found for the depletion and accumulation state, respectively, while the coercive fields are about 100 and 200 Oe. The magnetic properties are also characterized with soft x-ray

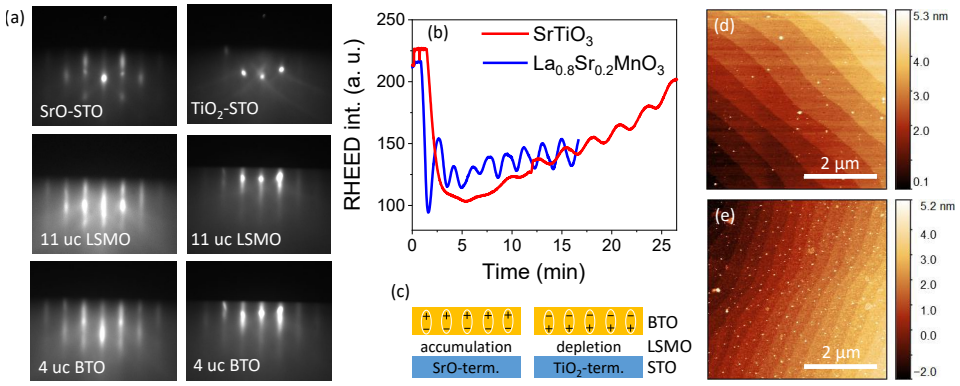

Figure 6.1: (a) RHEED patterns after the deposition of the $La_{0.8}Sr_{0.2}MnO_3$ and $BaTiO_3$ layers on SrO (left) and TiO_2 (right) terminated $SrTiO_3$(001). The energy of the electron beam was set to 15 keV. (b) RHEED intensity oscillations for the $SrTiO_3$ homoepitaxial growth, used to control the termination of the substrate, and during the deposition of the first 9 uc of the $La_{0.8}Sr_{0.2}MnO_3$ layer. (c) Sketch of the samples' structure showing the expected polarization according to the substrate termination and the interfacial electronic state of the $La_{0.8}Sr_{0.2}MnO_3$ layer. (d) and (e) AFM measurements after the deposition of $BaTiO_3/La_{0.8}Sr_{0.2}MnO_3$ heterostructures on TiO_2 and SrO-terminated $SrTiO_3$, respectively.

absorption spectroscopy, which, considering the 4 uc thick $BaTiO_3$ layer on the top of the $La_{0.8}Sr_{0.2}MnO_3$, is very sensitive to the interfacial magnetic state because of the small escape depth of the electrons, when the spectra are collected in TEY mode. Figure 6.2(d) shows the XAS spectra for the two samples, which are characteristic of Mn in a mixed 3+/4+ valence state and of fully oxidized and stoichiometric $La_{0.8}Sr_{0.2}MnO_3$ [232]. Because of experimental problems during the acquisition of the data, the SrO-terminated spectra does not exhibit the typical steps between the two edges and cannot be used to perform a quantitative analysis; however, these results confirm that the magnetic moments are due to the interfacial Mn atoms and not to impurities in the samples.

6.3.1 XPS and ARPES results

In Fig. 6.3 we show the XPS overview scan on the two samples with opposite ferroelectric polarizations. One can recognize the peaks corresponding to the elements present in the samples, i.e., Sr ($\sim$ 132 eV), Mn ($\sim$ 640 eV), Ba ($\sim$ 780 eV) and Ti ($\sim$ 460 eV). Furthermore, an adventitious C contribution appears at the typical energy of 284 eV. The presence of adsorbates such as C is expected when a sample is exposed to x-ray light, but in the case of ferroelectric materials it brings an important information on the polarization

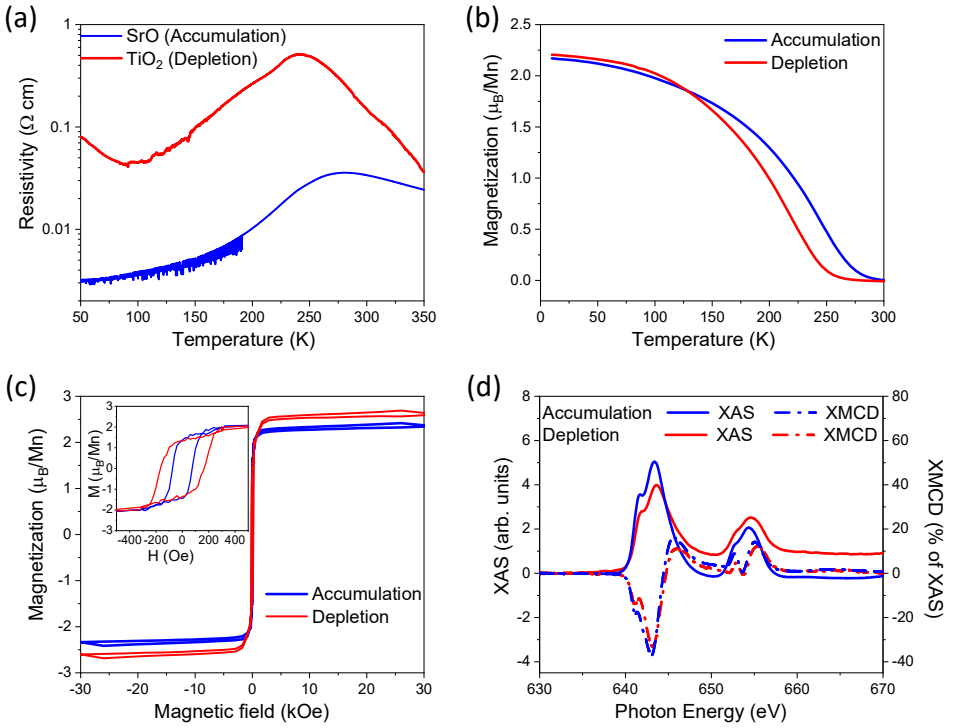

Figure 6.2: (a) Resistivity of the two samples as a function of temperature, showing a metal-to-insulator transition in proximity of the Curie temperature. (b) Magnetization as a function of temperature indicative of two opposite polarization states of the $BaTiO_3$ layer. (c) *M-H* hysteresis loops from which the saturation moments are extracted. Inset: Zoomed *M-H* to highlight the coercive field. (d) XAS and XMCD characterization of the two heterostructures at 20 K. The XMCD spectra are multiplied by a factor 10 for easy of display.

state. In Fig. 6.4 we show the XPS signal focused on the C energy for the two samples; interestingly, the signal is twice as large in the SrO-terminated sample. This is an indication of the opposite ferroelectric polarization state of the two samples: if the polarization is pointing away from the interface (P^+), the concentration of adsorbates on the surface is higher than if the polarization points towards the interface (P^-) [256]. The XPS signal at the C line is consistent with the expected ferroelectric polarization, indicating a P^+ ferroelectric polarization for the SrO-terminated sample. Figure 6.5(a-d) shows the XPS signal at the Mn 2*p*, Sr 3*d*, Ba 2*p* and Ti 2*p* emission edges, respectively. The Gaussian curves in the Mn spectra represent the different oxidation states of the elements resulting from the multiple peak fit: a negligible amount of Mn^{2+} (red curve) is detected, while the ratio between the 3+ and 4+ oxidation state is smaller for the SrO-terminated sample by a factor

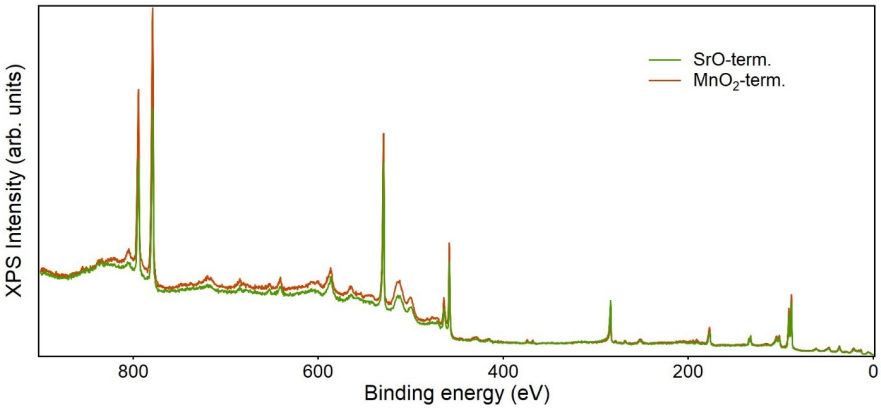

Figure 6.3: XPS overview scan, displaying the features from the elements present in the heterostructures.

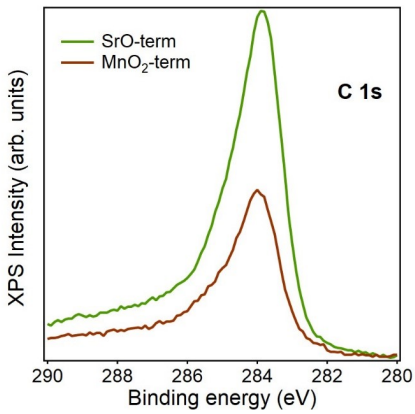

Figure 6.4: XPS view of the C peak.

of 10%, in agreement with interfacial accumulation of holes. Tellingly, the Ba and Ti signals show a shift in energy between the two samples which is not observed in the Mn and Sr signal. This shift is generally associated with the different electrostatic potentials through the $BaTiO_3$ layer due to the different ferroelectric polarizations. Figure 6.5(e) is a sketch of the variation of the electrostatic potential V(z) as a function of the $BaTiO_3$ thickness: in the ideal case (dotted line), where there are no intrinsic compensation mechanisms from contaminants on the surface, we would expect a shift to higher binding energies for P^+ polarization. Nonetheless, the presence of adsorbates has the effect of screening the ferroelectric polarization and bending V(z) (solid lines), resulting in the opposite shift: the Ba and Ti spectra relative to the sample with P^+ polarization are shifted towards lower binding energies with respect to the sample with P^- polarization.

The ARPES measurements were performed after the alignment of the

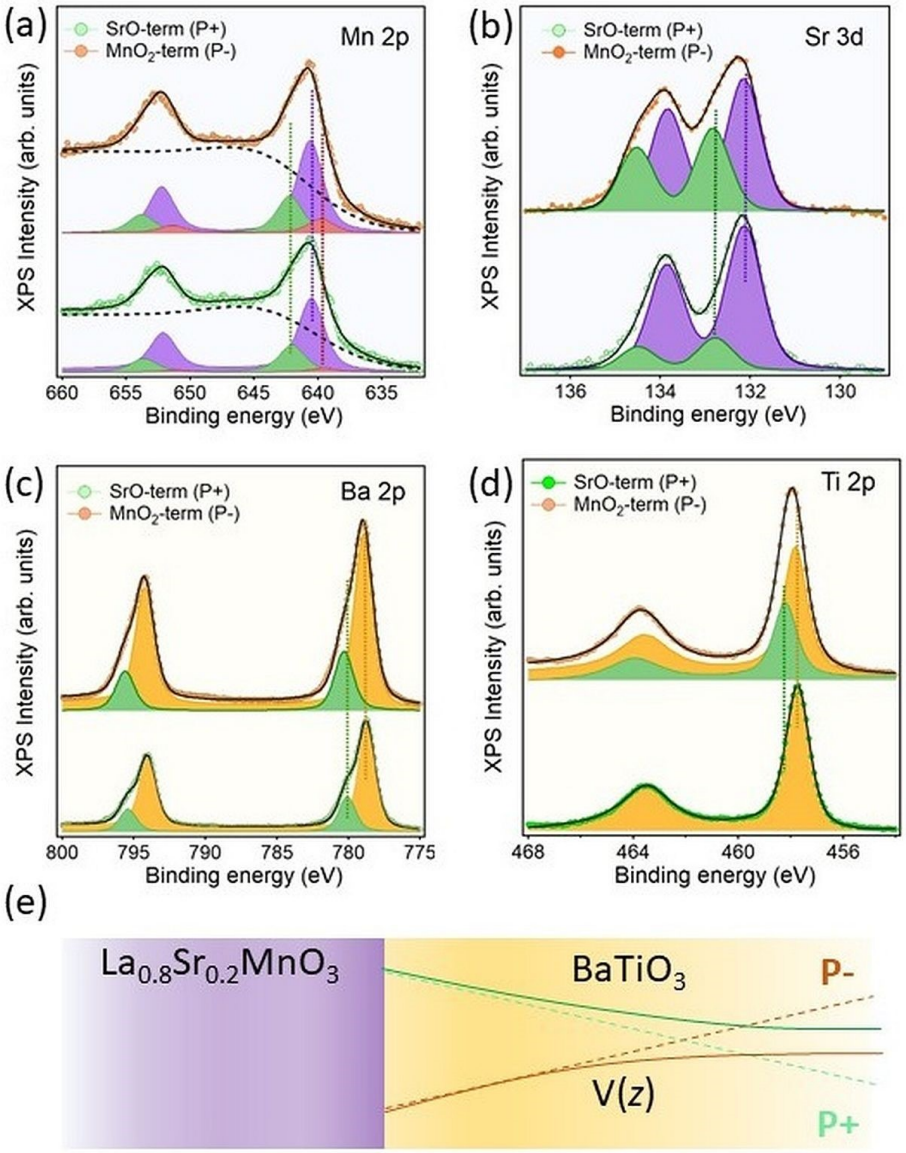

Figure 6.5: (a-d) XPS of the Mn $2p$, Sr $3d$, Ba $2p$ and Ti $2p$ states and Gaussian functions used for the multiple peak analysis. In particular, for the Mn spectra, Mn 2+ (red), 3+ (purple) and 4+ (green) is considered, while for the other elements the two peaks represent the bulk (lower binding energy) and the interface (higher binding energy) components. (e) Schematic representation of the electrostatic potential through the $BaTiO_3$ layer.

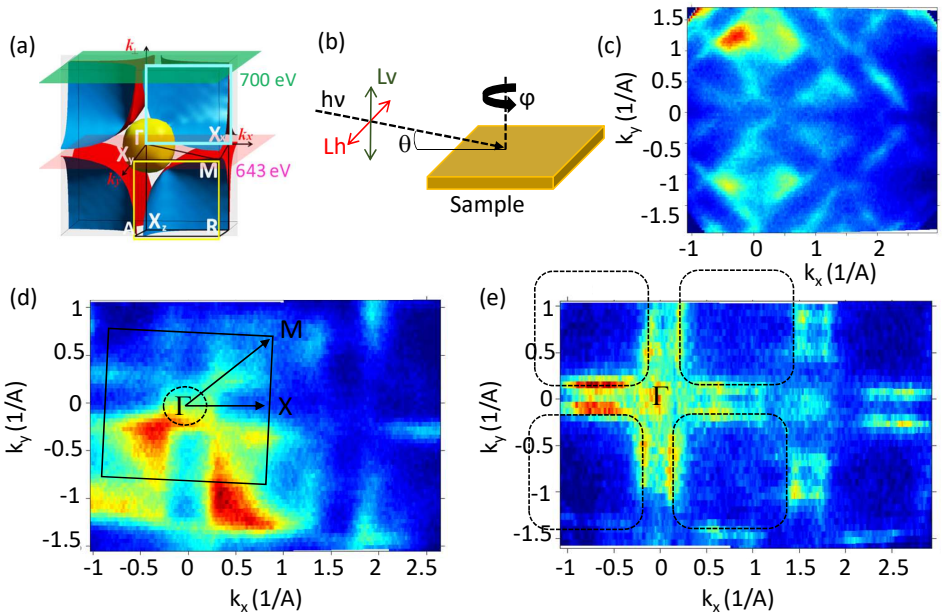

Figure 6.6: (a) Calculated Fermi surface for a 0.3-doped $La_{1-x}Sr_xMnO_3$ [77]. (b) Experimental geometry used for the ARPES data collection at the ADRESS beamline. (c) Fermi surface of a $La_{0.8}Sr_{0.2}MnO_3$ thin film on $SrTiO_3$(001) substrate in the ΓM geometry. (d) Fermi surface for a 12 uc $La_{0.8}Sr_{0.2}MnO_3$ thin films collected at 643 eV, showing the electronic sphere in the Γ point of the Brillouin zone; the M and X points are also defined. (e) Fermi surface at 700 eV, representing the hole pockets highlighted by the dashed squares.

Fermi surface using a 12 uc $La_{0.8}Sr_{0.2}MnO_3$ reference sample without the $BaTiO_3$ layer. In particular, the azimuth and polar angles are set such that two consecutive Γ points lie at the same tilt value. The electron-like band structure is collected with a photon energy of E=643 eV, i.e., in resonance with the Mn L_3-edge. After scanning the perpendicular direction of the Fermi surface, which is performed by varying the energy of the photon beam, we identify the hole cuboid structures at E=700 eV. Figure 6.6(a) shows a calculated Fermi surface for manganites, consisting of an electron-like spheroid in the center (Γ) of the Brilloun zone (BZ) and hole-like pockets at the corners (R) [258]. The ΓX and ΓM alignment corresponds to aligning the light propagation vector along the [100] and [110] direction, respectively. With reference to the experimental geometry shown in Figure 6.6(b), the $d_{(3z^2-r^2)}$ orbitals are probed with linear vertical light polarization in the ΓX alignment, while the $d_{(x^2-y^2)}$-derived band structure is probed with linear horizontal light polarization in the ΓM alignment, according to the ARPES sum rules [175, 182–184]. In Figure 6.6(c-e) we show the Fermi surface for

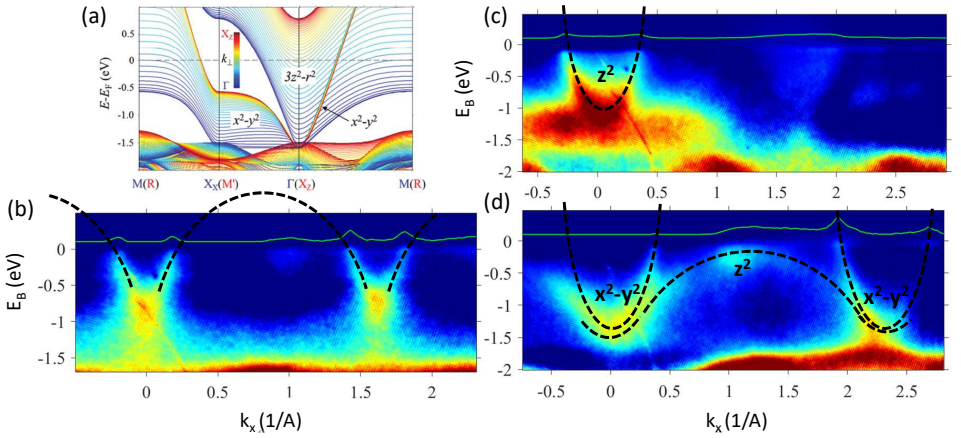

Figure 6.7: (a) Theoretical calculation of the band structure of 0.33 doped $La_{1-x}Sr_xMnO_3$ (from [257]) (b) Hole-like band structure collected with incoming photon energy E=700 eV (c)-(d) Electronic band structure collected at 643 eV (i.e., in resonance with Mn L-edge) in the ΓX geometry and p-polarized light (c) and ΓM geometry and s-polarized light (d), probing the $e_{g(3z^2-r^2)}$ and $e_{g(x^2-y^2)}$ orbital characters, respectively. The dashed lines are a guide to the eye.

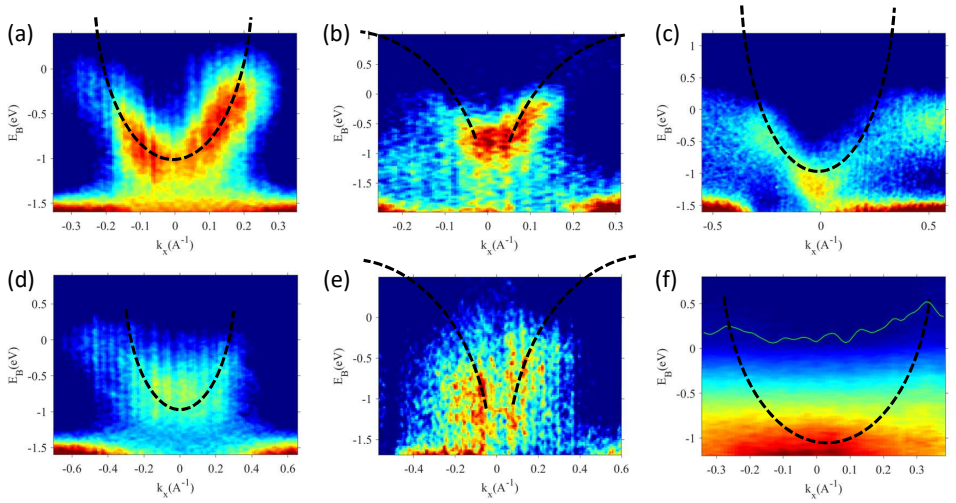

Figure 6.8: (a)-(c) Band structures for the sample in hole depletion state relative to the electronic z^2 orbital, hole-derived x^2-y^2 orbital and electronic x^2-y^2 orbital, the latter collected in ΓM geometry with s-polarized light. (d)-(f) Same band structures for the sample in hole accumulation state. In the ΓM geometry the x^2-y^2 orbital is zoomed in (g) in order to extract the MDC. The dashed parabola are a guide to the eye.

a 12 uc $La_{0.8}Sr_{0.2}MnO_3$ film grown on SrO-terminated $SrTiO_3$, showing the typical features expected for this system: in the ΓM [Fig. 6.6(c)] and ΓX [Fig. 6.6(d)] alignment the Γ points is surrounded by cuboids which were observed in other manganite systems and associated to $d_{(x^2-y^2)}$-derived orbitals [259,260]; in $La_{1-x}Sr_xMnO_3$ thin films they are generally a signature of the rombohedral distortion occurring at low temperatures [258]. Figure 6.6(e) shows the cut of the Fermi surface collected with E=700 eV, where the hole cuboids typical of manganites are visible. After the Fermi surface is aligned, the band structures are collected for the $La_{0.8}Sr_{0.2}MnO_3$ film and the two heterostructures in accumulation and depletion states. Figure 6.7(a) shows the calculated band structure for $La_{0.8}Sr_{0.2}MnO_3$ along different directions of the BZ [257] as a reference, while in Figure 6.7(b-d) we show the band structure for $La_{0.8}Sr_{0.2}MnO_3$ thin film without the $BaTiO_3$ layer; by integrating the intensity at the Fermi energy with an integration window of 0.1 eV we get the momentum distribution curves (MDC) shown as a green line close to the Fermi level. The peaks are fitted with two Gaussian functions, giving the k_x value in which the parabola crosses the Fermi level, i.e., the Fermi wavevector k_F which, in the free electron gas approximation and for a spin polarized metal, is related to the electronic density n_e by the relation $n_e = k_F^3/6\pi^2$. The $d_{(3z^2-r^2)}$ and $d_{(x^2-y^2)}$-derived bands [Fig. 6.7(c) and (d)] allow one to extract k_F and n for the out-of-plane and in-plane orbital, respectively, given in Table 6.1. The hole bands in Fig. 6.7(b) are collected using a photon beam with energy of 700 eV and linear vertical light; the MDC and the Fermi wavevector are extracted as in the previous case, but the density of holes is calculated assuming a cubic Fermi surface according to the Luttinger formula $n_h = \frac{(2\pi/a-k_F)^3}{(2\pi)^3}$ [261], where a is the lattice parameter of the cubic unit cell. Generally speaking, the effect of the tensile strain induced by the $SrTiO_3$ substrate is that of stabilizing the in-plane orbitals, which are preferentially occupied due to a lower Coulomb repulsion among electrons. Our results are in agreement with these expectations and with previous reports in the literature [30,32,235,254,262], showing a higher electron density in the $d_{(x^2-y^2)}$ orbital, consistent with a larger in-plane orbital occupation due to the tensile strain induced by the substrate. In order to determine the effect of the ferroelectric polarization on the electronic properties of the $La_{0.8}Sr_{0.2}MnO_3$ layer, we collected the $d_{(3z^2-r^2)}$ and $d_{(x^2-y^2)}$-derived electronic band structure and the $d_{(x^2-y^2)}$-derived hole band structures in $BaTiO_3/La_{0.8}Sr_{0.2}MnO_3$ heterostructures, shown in Fig. 6.8. In order to illustrate the significant changes in the band structures, only the features of interest are shown here. By comparing the TiO_2-terminated (a-c) and the SrO-terminated (d-f) samples, one observes that the band structure extracted from the former sample shows broader dispersion bands: although generally this is not expected (the two samples were grown at the same time), some small differences in the surface quality as well as the different ferro-

Table 6.1: Fermi wavevectors (k_F) and charge densities (n) extrapolated for the three samples from the ARPES study.

Sample	Hole bands		$d_{(3z^2-r^2)}$		$d_{(x^2-y^2)}$	
	k_F (Å)	n (cm^{-3})	k_F (Å)	n (cm^{-3})	k_F (Å)	n (cm^{-3})
Film	0.186	7.63×10^{21}	0.298	0.45×10^{21}	0.390	1.00×10^{21}
Acc.	0.14	9.46×10^{21}	0.294	0.43×10^{21}	0.3	0.46×10^{21}
Depl.	0.201	7.09×10^{21}	0.33	0.61×10^{21}	0.43	1.34×10^{21}

electric polarization may result in a broadening of the features. Nonetheless, using the same procedure described for the $La_{0.8}Sr_{0.2}MnO_3$ film, the Fermi wavevector and the density of holes and electrons are extrapolated and listed in Table 6.1. The data relative to the hole-band occupation agree with the expectations: a higher density of holes in accumulation state and lower for the depletion one, with the uncapped $La_{0.8}Sr_{0.2}MnO_3$ hole density in between these two values. The change in hole density is 24% in the case of hole accumulation, about half of that predicted by previous calculations [61]; this suggests that the $BaTiO_3$ is not fully electrically polarized. The electron density changes in a more complex way. Let us first focus on the SrO-terminated sample (interfacial hole accumulation): the main characteristic that one observes is the strong electron depletion in the $d_{(x^2-y^2)}$ orbital, with a negligible variation of the density of electrons in the out-of-plane orbital, indicating that the main contribution to the magnetic behavior comes from the occupation of the in-plane orbital. Differently, in the TiO_2-terminated sample (hole depletion) both $d_{(x^2-y^2)}$ and $d_{(3z^2-r^2)}$ densities change by a significant amount. This behavior is in agreement with previous ARPES studies on $La_{0.7}Sr_{0.3}MnO_3/BaTiO_3$ heterostructures in depletion state [77]: although, based on the displacement of the O anion, the out-of-plane orbital is predicted to be favoured [74], the in-plane orbital is predominantly occupied due to the reduced ferroelectric polarization of the $BaTiO_3$ and the tensile strain induced by the substrate.

6.3.2 Resonant reflectivity results

We now study the magnetic depth profile of the $La_{0.8}Sr_{0.2}MnO_3$ layer for the two polarization states of $BaTiO_3$. We exploit x-ray resonant reflectivity (XRR) to probe the two samples by tuning the polarization of the photon beam at the Mn L-edge; this allows us to be sensitive both to the structural and magnetic degrees of freedom. The data are fit using the DYNA software [195], which requires as input the magnetic and resonant scattering factors, as already mentioned in section 6.3.2. To this goal, we use the spectroscopy results obtained on the TiO_2-terminated sample. As magnetic parameter, DYNA gives the magnetic moment in units of the moment per atom extracted from the magnetic scattering constant; therefore, one needs to cal-

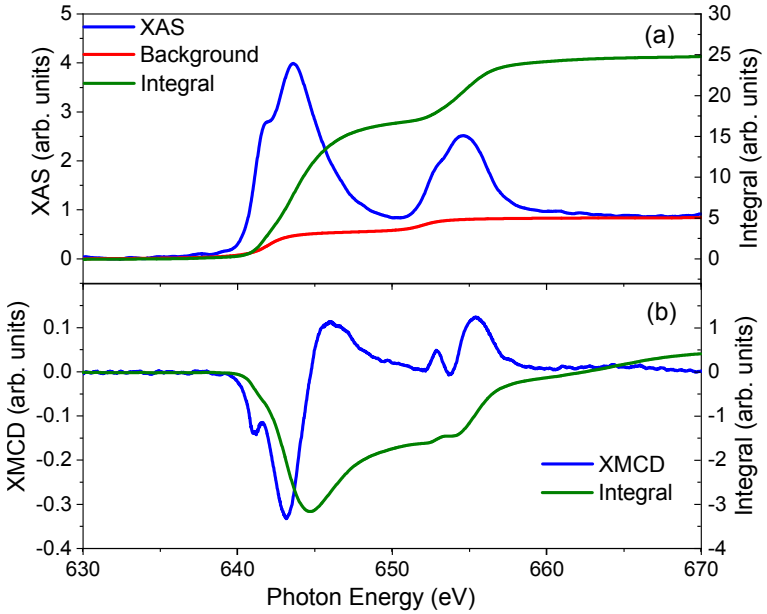

Figure 6.9: (a) XAS spectra and background function. The integral is performed over the background-subtracted XAS spectra. (b) XMCD obtained as the difference between C+ and C- polarization and integral used to calculate the magnetic moments according to the sum rules.

culate the magnetic moment in μ_B units from the XMCD results. In Fig. 6.9 we show the XAS spectra after removing the atomic background and the integrated area of the XAS(a) and the XMCD(b). The magnetic moment is calculated according to the sum rules defined in equation 3.18 [164,165,263]. The number of holes $(10 - n_{3d})$ is calculated following [264]. The spin part of the magnetic moment is multiplied by 1.5 in order to take into account the overlap of the L_3 and L_2 edges [167]. The extracted spin and orbital moment are 4.00 μ_B/Mn and -0.14 μ_B/Mn, respectively. The two values show opposite sign due to the third Hund's rules, requiring the minimization of the total angular moment, and the orbital moment is one order of magnitude smaller than the spin one, as expected because of the low magnetic anisotropy in these systems. One finds a total magnetic moment of $m_{tot} = m_{spin} + m_{orb} = 4.00 - 0.14 = 3.86$ μ_B/Mn, slightly higher than the value expected for bulk $La_{0.8}Sr_{0.2}MnO_3$ of 3.8 μ_B/Mn and almost double the one found by SQUID; since the result obtained by XMCD is relative to the surface of the sample, given the limited mean free path of the electrons in a the solid, the high magnetic moment found by the sum rules is in strong agreement with the expectations, specially considering that the sample is in the hole depletion state and is expected to show an enhanced magnetic moment at the interface. In the following, the values of the magnetic moment

are expressed in μ_B/Mn and are obtained by multiplying the parameter given by DYNA as output by 3.86.

The simulations are performed by simultaneously fitting the reflectivity and asymmetry at 642 eV and the energy scans and XMCD at 5 and 40 degrees of incidence. In order to elaborate the model, DYNA fits the thickness, roughness, density and the magnetic moments for each layer. As a starting point, we consider a model with four layers, i.e., C, $BaTiO_3$, $La_{0.8}Sr_{0.2}MnO_3$ and $SrTiO_3$. If the model does not correctly represent the asymmetry scans, the magnetic layer needs to be split in more parts in order to consider the different magnetization across the sample profile. In our case, three different $La_{0.8}Sr_{0.2}MnO_3$ layers are considered in order to correctly fit the data. Figure 6.10(a-d) and 6.11(a-d) show the reflectivity, the asymmetry, the energy scan at an angle of incidence of 40° with C+ and C- polarization and the XMCD signal at 40° incidence for the TiO_2 and SrO-terminated sample. We first discuss the structural parameters, i.e., the density, roughness and thickness of each layer. DYNA works with the density in units of mol/cm^3, which is obtained by dividing the mass density in g/cm^3 with the atomic mass in g/mol (which is, by definition, equivalent to the atomic mass in amu). The bulk density values of the $SrTiO_3$ and $BaTiO_3$ films is 0.026 g/mol while for $La_{0.8}Sr_{0.2}MnO_3$ is 0.028 g/mol, although in thin films slight changes in the densities may occur. In Fig. 6.10(a) and Fig. 6.11(a) we show the resonant reflectivity data collected at 642 eV with circular plus and minus light polarization and the simulations obtained with the parameters in Table 6.2 and 6.3 for the TiO_2 and SrO-terminated samples, respectively. The results are in very good agreement with the expectations: a thickness of 11 uc and 4 uc for the $La_{0.8}Sr_{0.2}MnO_3$ and $BaTiO_3$ layer, respectively, and roughnesses between 0.2 and 0.5 nm, confirming the thickness obtained by observing the RHEED oscillations and very smooth surfaces. Also the thickness of the C layer, which we introduce to simulate the presence of the contaminants on the surface, is larger in the SrO-terminated sample, as also observed by the XPS measurements. We now look at the magnetic profile, introducing first the results on the TiO_2-terminated sample, i.e., where the $La_{0.8}Sr_{0.2}MnO_3$ is in hole depletion state. Three different $La_{0.8}Sr_{0.2}MnO_3$ layers are considered with different magnetic moments: at the interface with the $SrTiO_3$ we obtain 6 uc of $La_{0.8}Sr_{0.2}MnO_3$ with a reduced moment of $\sim$ 2.08 μ_B/Mn, which is expected because of the reduced magnetization that the $La_{0.8}Sr_{0.2}MnO_3$ exhibits when directly grown on $SrTiO_3$. The rest of the film has a magnetization of $\sim$ 3.01 μ_B/Mn, except for the last 3.8 Å, where an enhanced moment of 4.05 μ_B/Mn is reported, in agreement with the behavior of $La_{0.8}Sr_{0.2}MnO_3$ in hole depletion state. Interestingly, if one calculates the average magnetic moment from the values obtained with the fit, the result m_{tot} = 2.57 μ_B/Mn is consistent with the SQUID result (2.6 μ_B/Mn). We now describe the results for the SrO-terminated sample (hole accumulation). Before going into the details it is important to point out

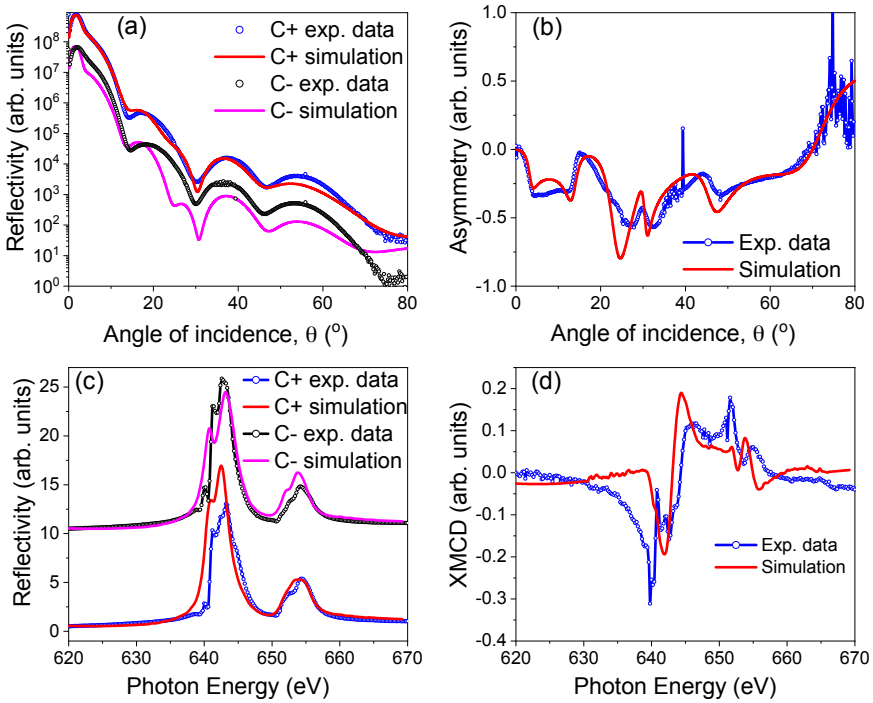

Figure 6.10: Resonant reflectivity data and simulations for the TiO_2-terminated sample. (a) Reflectivity as a function of the angle of incidence in resonance with the Mn L_3 edge (photon beam with energy 642 eV) with C+ and C- light polarization. (b) Asymmetry obtained as the normalized difference between the two reflectivity collected with opposite polarization. (c) Energy spectra at 40° incidence with circular positive and negative polarization. (d) XMCD signal at 40° of incidence. The red curves are the fit to the data. All the measurements are performed at 10 K.

that the used scattering factors are extracted from the spectroscopic data of the TiO_2-terminated sample and hence may not be fully representative of this system. Also in this case, the $La_{0.8}Sr_{0.2}MnO_3$ layer is split in three parts, but the relative thicknesses are different. At the interface with the $SrTiO_3$, the thickness of the layer with reduced moment is lower than for the TiO_2 sample and the magnetic moment of the layer in the middle is slightly reduced. Interestingly, the interfacial layer of 6.8 Å thickness exhibits a reduced magnetic moment of 2.16 μ_B/Mn.

Table 6.2: Fitting parameters of the RXRR data for the TiO_2-terminated sample.

Layer	Density (g/cm^3)	Thickness (Å)	Roughness (Å)	MMS (μ_B/Mn)
C	0.7	5.9	3.9	0
$BaTiO_3$	6.3	16.5	3.1	0
$La_{0.8}Sr_{0.2}MnO_3$	7.6	3.8	2.2	4.05
$La_{0.8}Sr_{0.2}MnO_3$	7.6	12	0	3.01
$La_{0.8}Sr_{0.2}MnO_3$	7.6	24.4	0	2.08
$SrTiO_3$	4.8	10^5	3.2	0

Table 6.3: Fitting parameters of the RXRR data for the SrO-terminated sample.

Layer	Density (g/cm^3)	Thickness (Å)	Roughness (Å)	MMS (μ_B/Mn)
C	0.7	10	2.2	0
$BaTiO_3$	6.3	16.5	5.2	0
$La_{0.8}Sr_{0.2}MnO_3$	7.6	6.8	2.3	2.16
$La_{0.8}Sr_{0.2}MnO_3$	7.6	17.6	0	2.86
$La_{0.8}Sr_{0.2}MnO_3$	7.6	15.4	0	2.43
$SrTiO_3$	4.8	10^5	4.5	0

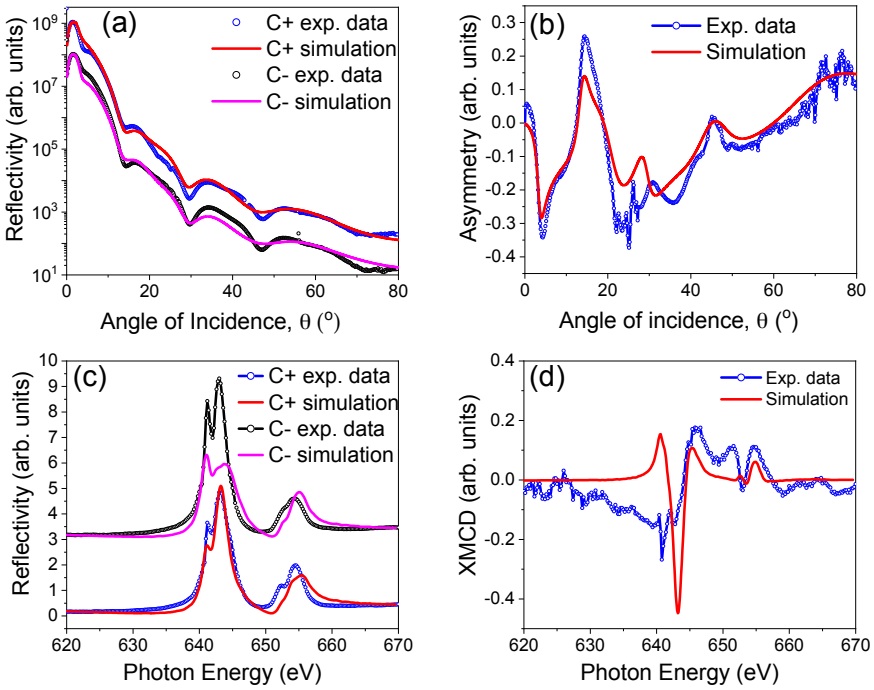

Figure 6.11: Resonant reflectivity data and simulations relative to the SrO-terminated sample. (a) Reflectivity as a function of the angle of incidence in resonance with the Mn L_3 edge (photon beam with energy 642 eV) with C+ and C- light polarization. (b) Asymmetry obtained as the normalized difference between the two reflectivity collected with opposite polarizations. (c) Energy spectra at 40° incidence with circular positive and negative polarization. (d) XMCD signal at 40° of incidence. The red curves are the fit to the data. All the measurements are performed at 10 K.

6.4 Discussion

As we have seen from the ARPES results, the accumulation and depletion states exhibit different in-plane and out-of-plane orbital occupations. In particular, the density of holes increases (decreases) when the ferroelectric polarization points away from (towards) the interface, as expected for a film in accumulation (depletion) state. The electron densities change in a complex way. In order to understand the behavior, we compare the densities in accumulation and depletion state with the ones obtained for the $La_{0.8}Sr_{0.2}MnO_3$ film without the $BaTiO_3$ layer. In the depletion state, both in-plane and out-of-plane orbitals experience a change with respect to the bare $La_{0.8}Sr_{0.2}MnO_3$ film; in particular, a change of 35% and 34% is observed for the two orbitals, indicating that the ferroelectric polarization influences both the in-plane and

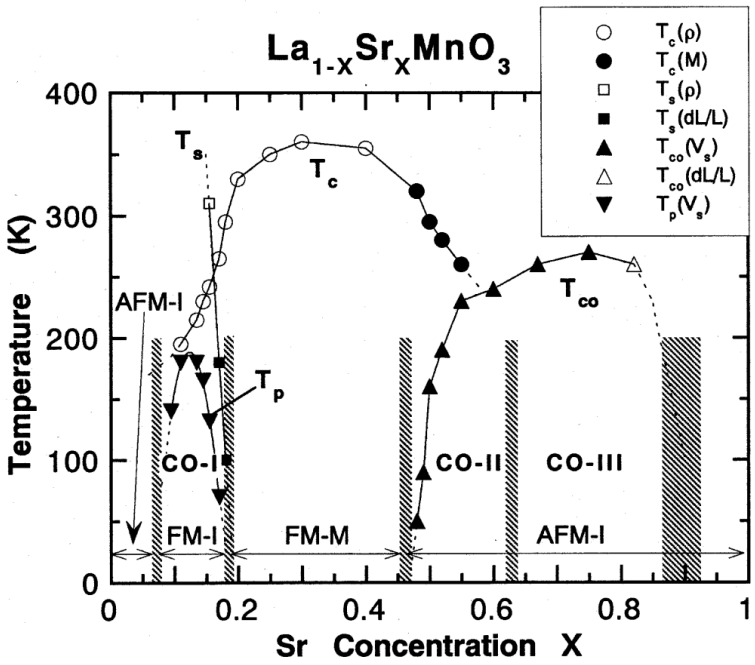

Figure 6.12: Magnetic phase diagram for hole-doped manganites. Figure taken from [10].

out-of-plane orbitals in the same way. On the other hand, the sample in accumulation state shows no significant differences in the out-of-plane orbital occupation, which remains unchanged when the $BaTiO_3$ is introduced, while the in-plane orbital occupation changes by 54%, almost twice that observed in the depletion state. Interestingly, the electron densities for the $d_{(x^2-y^2)}$ and $d_{(3z^2-r^2)}$ orbitals for this state are very close, indicating no preferential orbital occupation: the preferred in-plane orbital occupation due to the tensile strain from the substrate is suppressed by the ferroelectric polarization which induces an isotropic occupation of the Mn d orbitals.

One can estimate the ferroelectric polarization of the $BaTiO_3$ film based on the modulation of the densities of electrons found for the heterostructures in the accumulation and depletion states: the difference between the total densities in the two samples in $\Delta\rho$=1.06×10^{21}cm^{-3}. Assuming a probing depth d in the $La_{0.8}Sr_{0.2}MnO_3$ layer (attenuated by the $BaTiO_3$) of 2 uc, one gets

$$P = \frac{[\Delta\rho \times d \times \mathrm{e}]}{2} = \frac{\left[(1.06\times10^{21})\times(8\times10^{-8})\times(1.6\times10^{-19})\right]}{2} = 6\ \frac{\mu\mathrm{C}}{\mathrm{cm}^2}$$

which represents the ferroelectric polarization of the $BaTiO_3$ film. A comparison with the bulk value of the $BaTiO_3$ ferroelectric polarization (about 20 μC/cm^2 [124, 128]) indicates that the $BaTiO_3$ thin film exhibits reduced

polarization, as expected for a 4 uc thick film [127,128]. This is also consistent with the behavior that we observe with SQUID: although a difference in the saturation moment of about 25% is expected for this system, we see only a reduced difference which we attribute to the fact that the $BaTiO_3$ ferroelectic polarization is attenuated with respect to that of thicker films. Based on the difference in the orbital occupation from the ARPES results, one can estimate the hole doping at the interface with the $BaTiO_3$ layer, resulting in $x \sim 0.1$ and $x \sim 0.3$ in the depletion and accumulation state, respectively. By comparing these number to the phase diagram in Figure 6.12 one finds that the TiO_2-terminated sample is, at the interface with the $BaTiO_3$, in a ferromagnetic insulating state. The result is consistent with the transport measurements, showing a higher resistivity and lower metal-to-insulator transition temperature for this sample. In the case of SrO-termination, the interfacial state is in the optimally doped regime, exhibiting a higher Curie temperature and a ferromagnetic conducting behavior, as confirmed by the transport measurements. Furthermore, the orbital occupation is more isotropic, with a ratio between in-plane and out-of-plane orbital occupation close to 1, as expected for a ferromagnetic conducting system. The observation reported here reflects in the magnetic depth profile extracted from the reflectivity data: in the hole depletion state, the $La_{0.8}Sr_{0.2}MnO_3$ exhibits an increased interfacial magnetic moment due to the charge modulation at the interface; consistently, the interfacial magnetization of the sample in the accumulation state is reduced, as expected by charge modulation. The magnetoelectric coupling between the $BaTiO_3$ and the $La_{0.8}Sr_{0.2}MnO_3$ layer is such to steer through the phase diagram of manganites, resulting in ferromagnetic insulating and ferromagnetic metallic state for the TiO_2 and SrO-terminated sample, respectively. The weak ferroelectric polarization due to the low thickness of the $BaTiO_3$ does not allow to flip the interfacial magnetic state into an A-type antiferromagnetic spin order, as observed in previous reports. Nonetheless, we anticipate that, by depositing a thicker $BaTiO_3$ film, the effect of interfacial hole depletion and accumulation would be stronger, leading the system in the antiferromagnetic part of the $La_{0.8}Sr_{0.2}MnO_3$ phase diagram.

6.5 Conclusions

We have studied the interfacial electronic and magnetic properties of $BaTiO_3$/$La_{0.8}Sr_{0.2}MnO_3$ multiferroic heterostructures as we switch the ferroelectric polarization of the $BaTiO_3$ layer. Our results show a preferential in-plane orbital occupation for the uncapped $La_{0.8}Sr_{0.2}MnO_3$ film and for the $BaTiO_3$/$La_{0.8}Sr_{0.2}MnO_3$ in the hole depletion state, in agreement with previous reports in the literature. In the accumulation state, the $La_{0.8}Sr_{0.2}MnO_3$ shows a strong electron depletion in the in-plane orbitals, while the out-of-plane

shows no changes, indicating that the main contribution to the variation of the magnetic properties is brought by the in-plane orbital occupation. Resonant x-ray reflectivity measurements confirm an enhanced intefacial magnetic moment for the TiO_2-terminated sample, while highlighting a reduced interfacial moment for the SrO-terminated one. Nonetheless, the spin flip expected in the accumulation state was not observed because of the reduced ferroelectric polarization of the $BaTiO_3$ layer. Our results elucidate the impact of the orbital occupation on the interfacial magnetic moment and, in particular, the impact of the direction of the ferroelectric polarization on the orbital occupations.

7

Conclusions and Outlook

The main goal of this work was to study the interfacial magnetic and electric properties of manganite thin films and to control the correlated state by exploiting several effects, including charge and spin exchange and charge mediated magnetoelectric coupling; in particular, three main different systems were investigated.

In the first study, we focused on the problem of the magnetic dead layer appearing in $La_{0.8}Sr_{0.2}MnO_3$ thin films when directly deposited on the $SrTiO_3$ substrate. A solution was proposed by engineering the interface with a differently doped manganite film, in order to exploit charge and spin exchange to fully magnetize the $La_{0.8}Sr_{0.2}MnO_3$ film down to 1 uc thickness. The introduction of an insulating ferromagnetic $LaMnO_3$ and a conducting antiferromagnetic $La_{0.45}Sr_{0.55}MnO_3$ buffer layer results in different interfacial spin configuration, as deduced from SQUID magnetometry and XMCD measurements. We observed a ferromagnetic alignment of the $La_{0.8}Sr_{0.2}MnO_3$ from the first unit cell in the former case and an antiferromagnetic alignment of the first 4 uc in the latter, as inferred by the systematic increase of the magnetization observed with bulk magnetometry and confirmed by the spectroscopic measurements. In order to understand the physical mechanisms behind the antiferromagnetic spin alignment, XLD and XPEEM measurements were performed on the $La_{0.45}Sr_{0.55}MnO_3$ series. An orbital reconstruction and a more isotropic orbital occupation occurs for thicknesses above 4 uc, concomitantly with the appearance of a net ferromagnetic moment, while the antiferromagnetic coupling to the buffer layer for thicknesses between 1 and 4 uc was confirmed by the observation of antiferromagnetic domains by x-ray photoemission electron microscopy. The properties of the $LaMnO_3$ buffer layer were also investigated; in particu-

lar, the effect of interdiffusion from the substrate was studied with x-ray photoemission spectroscopy, revealing interdiffusion of Sr already during the deposition, occurring at 720 °C, while the post-annealing step enhances the Sr interdiffusion. We conclude that the effect of interdiffusion is that of slightly doping the $LaMnO_3$ film driving it into the spin-canting region of the phase diagram. The importance of developing ultrathin full magnetic polarized $La_{0.8}Sr_{0.2}MnO_3$ films is important for applications in field-effect devices and technological applications, where, given the interfacial nature of the effect, the magnetoelectric coupling is expected to be strongly enhanced.

The magnetoelectric coupling of $BaTiO_3/La_{0.9}Ba_{0.1}MnO_3$ multiferroic heterostructures was investigated. In particular, ferroelectric square patterns were written on the $BaTiO_3$ layer using an atomic force microscopy with a conducting tip in contact mode, applying voltages ranging between ± 8 V, and the magnetic response of the $La_{0.9}Ba_{0.1}MnO_3$ layer was imaged with x-ray photoemission microscopy. We find a strong drop in the magnetic contrast where $+7$ and $+8$ V were applied to the $BaTiO_3$, indicating that the hole depletion leads the $La_{0.9}Ba_{0.1}MnO_3$ into an antiferromagnetic configuration, as opposed to what is reported in the literature for the $La_{1-x}Sr_xMnO_3$ system but in agreement with previous reports on $La_{0.9}Ba_{0.1}MnO_3$, indicating that the magnetoelectric coupling in the latter acts differently from the more studied $La_{1-x}Sr_xMnO_3$.

Finally, we focused on $BaTiO_3/La_{0.8}Sr_{0.2}MnO_3$ heterostructures, where the orbital and magnetic order were studied as a function of the ferroelectric polarization direction of the $BaTiO_3$ layer. The ferroelectric state is controlled by changing the $SrTiO_3$ termination and the ferroelectric properties are deduced indirectly by characterizing the magnetic behavior of the $La_{0.8}Sr_{0.2}MnO_3$ layer. Indeed, the challenge for such a thin ferroelectric is the direct characterization of the ferroelectric properties, due to the large leakage current. From SQUID magnetometry and transport measurements, we conclude that the SrO-terminated $SrTiO_3$ results in the $La_{0.8}Sr_{0.2}MnO_3$ in hole accumulation state, the opposite is found for the TiO_2 termination, in agreement with previous reports in the literature. The electronic properties were studied with soft x-ray ARPES, which allows one to probe the different Mn d orbitals according to the ARPES selection rules. We found a change in the hole density consistent with the accumulation and depletion scenarios, i.e., a higher hole concentration in the sample in the accumulation state. The $d_{(x^2-y^2)}$ and $d_{(3z^2-r^2)}$ orbitals are probed separately and the electronic density is extracted; we observe a different behavior between the two samples. The TiO_2-terminated samples shows an overall higher electron density, which agrees with the hole depletion at the interface, with both in-plane and out-of-plane orbitals changing by a similar amount. The SrO-terminated sample, instead, behave in a more complex way: a decrease of the total electron density is observed, but the in-plane and out-of-plane orbitals behave differently, with the former changing by 50% with respect to

the $La_{0.8}Sr_{0.2}MnO_3$ film without the $BaTiO_3$ layer, while the latter remains unchanged. Interestingly, the electron density for the two orbitals is the same, which is expected to favour ferromagnetic alignment. By studying the magnetic profile with x-ray resonant reflectivity, one finds for the TiO_2 sample an enhanced magnetic moment at the interface with the $BaTiO_3$ layer and a reduced moment at the interface with the $SrTiO_3$, as expected because of the magnetic dead layer. For the SrO-terminated sample, instead, a reduced magnetic moment is found, with no changes at the interface with the $BaTiO_3$. We conclude that the thin $BaTiO_3$ layer exhibits a reduced ferroelectric polarization and is not capable of switching the magnetic interfacial $La_{0.8}Sr_{0.2}MnO_3$ state to the antiferromagnetic state, but is strong enough to modify the in-plane orbital occupancy, resulting in a decreased interfacial magnetic moment.

The results in this thesis shed light on some aspects which were not fully understood, providing further insights to the physics of manganites. The experimental findings are important for further progresses of the field: a natural next step is the development and the study of the interfacial properties of field-effect devices involving the ultrathin manganite films studied in chapter 4, where, given the interfacial nature of the effect, the magnetoelectric coupling is expected to be strongly enhanced. Other interesting systems to be considered for future investigations are $La_{1-x}Sr_xMnO_3$ films lying at different boundaries in the phase diagram (for example, 0.5 doping). Also, the control of the antiferromagnetic state is an interesting topic developing quickly under the name of antiferromagnetic spintronics, and the control of the interfacial antiferromagnetic spin alignment through the application of electric fields would be an important development in this context. A starting point in this sense is the $La_{0.8}Sr_{0.2}MnO_3/La_{0.45}Sr_{0.55}MnO_3$ system investigated in chapter 4, where we observed an antiferromagnetic spin alignment at low $La_{0.8}Sr_{0.2}MnO_3$ thicknesses. We also anticipate that our approach to enhancing the magnetic properties in ultrathin manganite films could be applied to differently doped systems.

The variety of the manganite phase diagram allows one to tune the magnetic properties of the system by varying the doping, giving the chance to investigate different mechanisms. The work presented in this thesis improves our current understanding of the magnetoelectric coupling mechanism, adding important insights towards a comprehensive understanding of these complex systems and opening the path for future developments.

Acknowledgements

The work presented in this thesis is the result of the collaboration with many scientists and valuable collaborators. The peculiar environment of PSI, with its open-door policy and interdisciplinary and multicultural nature, contributed to shape my work and myself. I would like to thank the Swiss National Science Foundation (SNSF, grant No. 200021_184684) for supporting financially my PhD.

First of all, I would like to acknowledge my supervisor and main collaborator Dr. Carlos A. F. Vaz. With his constant guidance and supervision, he gave me the opportunity to grow as a scientist. The discussions and debates that we had during these four years helped me to develop my critical thinking and problem solving skills; I have learnt that every problem is a challenge and that one can always extract the best out of it. His enthusiastic approach to the science has been my bench mark during my whole PhD.

I am grateful to my first supervisor Prof. Dr. Frithjof Nolting for his help and guidance during my PhD and for being always ready to offer his help. I have always appreciated our meetings and data discussion and I was always looking forward to the next meeting. I would also like to acknowledge Prof. Dr. Christian Schönenberger for his supervision during my PhD.

I cannot express how grateful I am to the microscopy and magnetism group, for the meetings where debate and discussions were always stimulated. It contributed to shape the nice working environment where I had the chance to work. I have learnt that there are not good or bad ideas, but just ideas that can be discussed.

I would like to acknowledge the collaborators at PSI who helped me with the measurements and data analysis. In particular, I am grateful to Dr. Dario F. Sanchez for the fluorescence measurements at the microXAS beamline, that helped me to calibrate the MBE that I have used for the sample growth. I thank the mesoscopic system group (in particular, Dr. Jamie Massey) for the training and support during the SQUID-VSM measurements. I acknowledge Dr. Christof Schneider for the help with the XRD measurements and the scanning probe microscopy userlab for the access to the AFM. I am grateful to Dr. Urs Staub and Dr. Elizabeth Skoropata for the help with the RESOXS measurements, Dr. Cinthia Piamonteze and Dr.

Diana Vaclavkova for the help at the X-Treme beamline and Dr. Vladimir Strocov and Dr. Fatima Alarab for supporting me during the data collection at the ADRESS beamline. I thank Dr. Armin Kleibert for his training to the XPEEM and support during beamtimes at SIM and Pascal Schifferle for the support with the MBE and technical problem at SIM beamline. Last, a special thank to Dr. Gyanendra Panchal for the fruitful discussion and the help in analyzing and collecting data.

A special thank goes also to Dr. Adrian M. Husanu, for the enthusiastic approach to the beamtimes and data analysis. He taught me all I know about ARPES with passion and patience, it has been a big pleasure collaborating with him.

I would like to acknowledge Ludovica Tovaglieri and Dr. Celine Lichtensteiger from the university of Geneva for the AFM and PFM measurements.

Finally, I would like to thank my family for the constant support and for always believing in me. A special thanks to Consiglia, for always pushing me and supporting me, for the kind words in the difficult moments. Andiamo, sempre.

Bibliography

[1] Claudine Noguera. Polar oxide surfaces. *Journal of Physics: Condensed Matter*, 12(31):R367, aug 2000.

[2] Jacek Goniakowski, Fabio Finocchi, and Claudine Noguera. Polarity of oxide surfaces and nanostructures. *Reports on Progress in Physics*, 71(1):016501, dec 2007.

[3] A. Ohtomo and H. Y. Hwang. A high-mobility electron gas at the LaAlO3/SrTiO3 heterointerface. *Nature*, 427(6973):423–426, Jan 2004.

[4] A. D. Caviglia, S. Gariglio, N. Reyren, D. Jaccard, T. Schneider, M. Gabay, S. Thiel, G. Hammerl, J. Mannhart, and J.-M. Triscone. Electric field control of the LaAlO3/SrTiO3 interface ground state. *Nature*, 456(7222):624–627, Dec 2008.

[5] K. Zou, Sohrab Ismail-Beigi, Kim Kisslinger, Xuan Shen, Dong Su, F. J. Walker, and C. H. Ahn. $LaTiO_3/KTaO_3$ interfaces: A new two-dimensional electron gas system. *APL Materials*, 3(3):036104, 03 2015.

[6] C. H. Ahn, S. Gariglio, P. Paruch, T. Tybell, L. Antognazza, and J.-M. Triscone. Electrostatic modulation of superconductivity in ultrathin $GdBa_2Cu_3O_{7-x}$ films. *Science*, 284(5417):1152–1155, 1999.

[7] Kevin A. Parendo, K. H. Sarwa B. Tan, A. Bhattacharya, M. Eblen-Zayas, N. E. Staley, and A. M. Goldman. Electrostatic tuning of the superconductor-insulator transition in two dimensions. *Phys. Rev. Lett.*, 94:197004, May 2005.

[8] C. A. F. Vaz, J. Hoffman, Y. Segal, J. W. Reiner, R. D. Grober, Z. Zhang, C. H. Ahn, and F. J. Walker. Origin of the magnetoelectric coupling effect in $Pb(Zr_{0.2}Ti_{0.8})O_3/La_{0.8}Sr_{0.2}MnO_3$ multiferroic heterostructures. *Phys. Rev. Lett.*, 104:127202, 03 2010.

[9] Carlos A. F. Vaz, Jason Hoffman, Charles H. Ahn, and Ramamoorthy Ramesh. Magnetoelectric coupling effects in multiferroic complex oxide composite structures. *Advanced Materials*, 22(26-27):2900–2918, 2010.

[10] Hiroyuki Fujishiro, Tetsuo Fukase, and Manabu Ikebe. Charge ordering and sound velocity anomaly in $La_{1-x}Sr_xMnO_3$ ($x \geq 0.5$). *Journal of the Physical Society of Japan*, 67(8):2582–2585, 1998.

[11] Sayani Majumdar and Sebastiaan van Dijken. Pulsed laser deposition of $La_{1-x}Sr_xMnO_3$: thin-film properties and spintronic applications. *Journal of Physics D: Applied Physics*, 47(3):034010, dec 2013.

[12] J. Hemberger, A. Krimmel, T. Kurz, H.-A. Krug von Nidda, V. Yu. Ivanov, A. A. Mukhin, A. M. Balbashov, and A. Loidl. Structural, magnetic, and electrical properties of single-crystalline $La_{1-x}Sr_xMnO_3$ ($0.4 < x < 0.85$). *Phys. Rev. B*, 66:094410, Sep 2002.

[13] B.I. Min, Yookyung Jo, and Minsu Kim. Phase diagram of perovskite manganites. *Physica B: Condensed Matter*, 312-313:723–725, 2002. The International Conference on Strongly Correlated Electron Systems.

[14] Hiroyuki Fujishiro, Tetsuo Fukase, and Manabu Ikebe. Anomalous lattice softening at $x = 0.19$ and 0.82 in $La_{1-x}Ca_xMnO_3$. *Journal of the Physical Society of Japan*, 70(3):628–631, 2001.

[15] P. Schiffer, A. P. Ramirez, W. Bao, and S-W. Cheong. Low temperature magnetoresistance and the magnetic phase diagram of $La_{1-x}Ca_xMnO_3$. *Phys. Rev. Lett.*, 75:3336–3339, Oct 1995.

[16] G. Venkataiah, Y. Kalyana Lakshmi, and P. Venugopal Reddy. Influence of sintering temperature on magnetotransport behavior of some nanocrystalline manganites. In Volodymyr Shatokha, editor, *Sintering*, chapter 13. IntechOpen, Rijeka, 2012.

[17] A-M Haghiri-Gosnet and J-P Renard. Cmr manganites: physics, thin films and devices. *Journal of Physics D: Applied Physics*, 36(8):R127, apr 2003.

[18] Jun Zhang, Hidekazu Tanaka, Teruo Kanki, Jae-Hyoung Choi, and Tomoji Kawai. Strain effect and the phase diagram of $La_{1-x}Ba_xMnO_3$ thin films. *Phys. Rev. B*, 64:184404, 10 2001.

[19] Eun-Mi Choi, Josée E. Kleibeuker, and Judith L. MacManus-Driscoll. Strain-tuned enhancement of ferromagnetic T_C to 176 K in Sm-doped $BiMnO_3$ thin films and determination of magnetic phase diagram. *Scientific Reports*, 7(1):43799, Mar 2017.

[20] M. Izumi, Y. Ogimoto, Y. Okimoto, T. Manako, P. Ahmet, K. Nakajima, T. Chikyow, M. Kawasaki, and Y. Tokura. Insulator-metal transition induced by interlayer coupling in $La_{0.6}Sr_{0.4}MnO_3/SrTiO_3$ superlattices. *Phys. Rev. B*, 64:064429, Jul 2001.

[21] Makoto Izumi, Yasushi Ogimoto, Takashi Manako, Masashi Kawasaki, and Yoshinori Tokura. Interface effect and its doping dependence in $La_{1-x}Sr_xMnO_3/SrTiO_3$ superlattices. *Journal of the Physical Society of Japan*, 71(11):2621–2624, 2002.

[22] Hiroyuki Yamada, Yoshihiro Ogawa, Yuji Ishii, Hiroshi Sato, Masashi Kawasaki, Hiroshi Akoh, and Yoshinori Tokura. Engineered interface of magnetic oxides. *Science*, 305(5684):646–648, 2004.

[23] Y. Ishii, H. Yamada, H. Sato, H. Akoh, Y. Ogawa, M. Kawasaki, and Y. Tokura. Improved tunneling magnetoresistance in interface engineered (La,Sr)MnO_3 junctions. *Applied Physics Letters*, 89(4):042509, 2006.

[24] Julia A. Mundy, Yasuyuki Hikita, Takeaki Hidaka, Takeaki Yajima, Takuya Higuchi, Harold Y. Hwang, David A. Muller, and Lena F. Kourkoutis. Visualizing the interfacial evolution from charge compensation to metallic screening across the manganite metal–insulator transition. *Nature Communications*, Mar 2014.

[25] R. Peng, H. C. Xu, M. Xia, J. F. Zhao, X. Xie, D. F. Xu, B. P. Xie, and D. L. Feng. Tuning the dead-layer behavior of $La_{0.67}Sr_{0.33}MnO_3/SrTiO_3$ via interfacial engineering. *Applied Physics Letters*, 104(8):081606, 2014.

[26] Åsmund Monsen, Jos E. Boschker, Ferran Macià, Justin W. Wells, Per Nordblad, Andrew D. Kent, Roland Mathieu, Thomas Tybell, and Erik Wahlström. Thickness dependence of dynamic and static magnetic properties of pulsed laser deposited $La_{0.7}Sr_{0.3}MnO_3$ films on $SrTiO_3$(001). *Journal of Magnetism and Magnetic Materials*, 369:197–204, 2014.

[27] F. Y. Bruno, J. Garcia-Barriocanal, M. Varela, N. M. Nemes, P. Thakur, J. C. Cezar, N. B. Brookes, A. Rivera-Calzada, M. Garcia-Hernandez, C. Leon, S. Okamoto, S. J. Pennycook, and J. Santamaria. Electronic and magnetic reconstructions in $La_{1-x}Sr_xMnO_3/SrTiO_3$ heterostructures: A case of enhanced interlayer coupling controlled by the interface. *Phys. Rev. Lett.*, 106:147205, Apr 2011.

[28] J.-S. Lee, D. A. Arena, P. Yu, C. S. Nelson, R. Fan, C. J. Kinane, S. Langridge, M. D. Rossell, R. Ramesh, and C.-C. Kao. Hidden magnetic configuration in epitaxial $La_{1-x}Sr_xMnO_3$ films. *Phys. Rev. Lett.*, 105:257204, Dec 2010.

[29] A. Tebano, A. Orsini, P. G. Medaglia, D. Di Castro, G. Balestrino, B. Freelon, A. Bostwick, Young Jun Chang, G. Gaines, E. Rotenberg, and N. L. Saini. Preferential occupation of interface bands in

$La_{2/3}Sr_{1/3}MnO_3$ films as seen via angle-resolved photoemission. *Phys. Rev. B*, 82:214407, Dec 2010.

[30] A. Tebano, C. Aruta, S. Sanna, P. G. Medaglia, G. Balestrino, A. A. Sidorenko, R. De Renzi, G. Ghiringhelli, L. Braicovich, V. Bisogni, and N. B. Brookes. Evidence of orbital reconstruction at interfaces in ultrathin $La_{0.67}Sr_{0.33}MnO_3$ films. *Phys. Rev. Lett.*, 100:137401, Apr 2008.

[31] H. Boschker, J. Verbeeck, R. Egoavil, S. Bals, G. van Tendeloo, M. Huijben, E. P. Houwman, G. Koster, D. H. A. Blank, and G. Rijnders. Preventing the reconstruction of the polar discontinuity at oxide heterointerfaces. *Advanced Functional Materials*, 22(11):2235–2240, 2012.

[32] M. Huijben, L. W. Martin, Y.-H. Chu, M. B. Holcomb, P. Yu, G. Rijnders, D. H. A. Blank, and R. Ramesh. Critical thickness and orbital ordering in ultrathin $La_{0.7}Sr_{0.3}MnO_3$ films. *Phys. Rev. B*, 78:094413, Sep 2008.

[33] W. W. Gao, W. M. Lü, A. D. Wei, J. Wang, J. Shen, B. G. Shen, and J. R. Sun. Buffer layer-induced positive magnetoresistance in manganite-based heterojunctions. *Journal of Applied Physics*, 111(7):07D711, 2012.

[34] W. W. Gao, F. X. Hu, B. G. Shen, and J. R. Sun. Modulation of the magnetic/conductive dead layer at the manganites-$SrTiO_3$ interface. *Journal of Applied Physics*, 117(17):17C733, 2015.

[35] Cinthia Piamonteze, Francis Bern, Sridhar Reddy Venkata Avula, Michał Studniarek, Carmine Autieri, Michael Ziese, and Ionela Lindfors-Vrejoiu. Ferromagnetic order of ultra-thin $La_{0.7}Ba_{0.3}MnO_3$ sandwiched between $SrRuO_3$ layers. *Applied Physics Letters*, 118(15):152408, 2021.

[36] Binbin Chen, Haoran Xu, Chao Ma, Stefan Mattauch, Da Lan, Feng Jin, Zhuang Guo, Siyuan Wan, Pingfan Chen, Guanyin Gao, Feng Chen, Yixi Su, and Wenbin Wu. All-oxide-based synthetic antiferromagnets exhibiting layer-resolved magnetization reversal. *Science*, 357(6347):191–194, 2017.

[37] C. Ritter, M. R. Ibarra, J. M. De Teresa, P. A. Algarabel, C. Marquina, J. Blasco, J. García, S. Oseroff, and S-W. Cheong. Influence of oxygen content on the structural, magnetotransport, and magnetic properties of $LaMnO_{3+\delta}$. *Phys. Rev. B*, 56:8902–8911, Oct 1997.

[38] J. Töpfer and J. B. Goodenough. Transport and magnetic properties of the perovskites $La_{1-y}MnO_3$ and $LaMn_{1-z}O_3$. *Chemistry of Materials*, 9(6):1467–1474, 1997.

[39] J. Töpfer and J.B. Goodenough. Charge transport and magnetic properties in perovskites of the system La-Mn-O. *Solid State Ionics*, 101-103:1215–1220, 1997. International Symposium on the Reactivity of Solids.

[40] J. Töpfer and J.B. Goodenough. $LaMnO_{3+\delta}$ revisited. *Journal of Solid State Chemistry*, 130(1):117–128, 1997.

[41] L. Ghivelder, I. Abrego Castillo, M. A. Gusmão, J. A. Alonso, and L. F. Cohen. Specific heat and magnetic order in $LaMnO_{3+\delta}$. *Phys. Rev. B*, 60:12184–12190, Nov 1999.

[42] Lorenzo Malavasi, Clemens Ritter, Maria Cristina Mozzati, Cristina Tealdi, M. Saiful Islam, Carlo Bruno Azzoni, and Giorgio Flor. Effects of cation vacancy distribution in doped $LaMnO_{3+\delta}$ perovskites. *Journal of Solid State Chemistry*, 178(6):2042–2049, 2005.

[43] F. J. Palomares, F. Pigazo, J. J. Romero, R. Cuadrado, A. Arroyo, M. A. García, A. Hernando, R. Cortés-Gil, J. M. González-Calbet, M. Vallet-Regí, J. M. González, and J. M. Alonso. Temperature dependence of the magnetic properties in $LaMnO_{3+\delta}$. *Journal of Applied Physics*, 99(8):08A702, 04 2006.

[44] V. S. Zakhvalinskiĭ, R. Laiho, K. G. Lisunov, E. Lähderanta, P. A. Petrenko, Yu. P. tepanov, J. Salminen, and V. N. Stamov. Preparation and magnetic properties of $LaMnO_{3+\delta}$ ($0 \leq \delta \leq 0.154$). *Physics of the Solid State*, 48(12):2300–2309, Dec 2006.

[45] H S Kim and H M Christen. Controlling the magnetic properties of $LaMnO_3$ thin films on $SrTiO_3(100)$ by deposition in a O_2/Ar gas mixture. *Journal of Physics: Condensed Matter*, 22(14):146007, mar 2010.

[46] Zsolt Marton, Sung Seok A. Seo, Takeshi Egami, and Ho Nyung Lee. Growth control of stoichiometry in $LaMnO_3$ epitaxial thin films by pulsed laser deposition. *Journal of Crystal Growth*, 312(20):2923–2927, 2010.

[47] Wei Niu, Wenqing Liu, Min Gu, Yongda Chen, Xiaoqian Zhang, Minhao Zhang, Yequan Chen, Ji Wang, Jun Du, Fengqi Song, Xiaoqing Pan, Nini Pryds, Xuefeng Wang, Peng Wang, Yongbing Xu, Yunzhong Chen, and Rong Zhang. Direct demonstration of the emergent magnetism resulting from the multivalence Mn in a $LaMnO_3$ epitaxial thin film system. *Advanced Electronic Materials*, 4(6):1800055, 2018.

[48] Jaume Roqueta, Alberto Pomar, Lluis Balcells, Carlos Frontera, Sergio Valencia, Radu Abrudan, Bernat Bozzo, Zorica Konstantinović, José

Santiso, and Benjamín Martínez. Strain-engineered ferromagnetism in $LaMnO_3$ thin films. *Crystal Growth & Design*, 15(11):5332–5337, Nov 2015.

[49] Liang Wu, Changjian Li, Mingfeng Chen, Yujun Zhang, Kun Han, Shengwei Zeng, Xin Liu, Ji Ma, Chen Liu, Jiahui Chen, Jinxing Zhang, Ariando, T. Venky Venkatesan, Stephen J. Pennycook, J. M. D. Coey, Lei Shen, Jing Ma, X. Renshaw Wang, and Ce-Wen Nan. Interface-induced enhancement of ferromagnetism in insulating $LaMnO_3$ ultra-thin films. *ACS Applied Materials & Interfaces*, 9(51):44931–44937, 2017. PMID: 29236463.

[50] R. Cortés-Gil, A. Arroyo, L. Ruiz-González, J.M. Alonso, A. Hernando, J.M. González-Calbet, and M. Vallet-Regí. Evolution of magnetic behaviour in oxygen deficient $LaMnO_{3-\delta}$. *Journal of Physics and Chemistry of Solids*, 67(1):579–582, 2006. Spectroscopies in Novel Superconductors 2004.

[51] Hrishit Banerjee and Markus Aichhorn. Emergence of a ferromagnetic insulating state in $LaMnO_3/SrTiO_3$ heterostructures: Role of strong electronic correlations and strain. *Phys. Rev. B*, 101:241112, Jun 2020.

[52] M. Izumi, Y. Konishi, T. Nishihara, S. Hayashi, M. Shinohara, M. Kawasaki, and Y. Tokura. Atomically defined epitaxy and physical properties of strained $La_{0.6}Sr_{0.4}MnO_3$ films. *Applied Physics Letters*, 73(17):2497–2499, 1998.

[53] F. S. Razavi, G. Gross, H.-U. Habermeier, O. Lebedev, S. Amelinckx, G. Van Tendeloo, and A. Vigliante. Epitaxial strain induced metal insulator transition in $La_{0.9}Sr_{0.1}MnO_3$ and $La_{0.88}Sr_{0.1}MnO_3$ thin films. *Applied Physics Letters*, 76(2):155–157, 2000.

[54] S. I. Khartsev, P. Johnsson, and A. M. Grishin. Colossal magnetoresistance in ultrathin epitaxial $La_{0.75}Sr_{0.25}MnO_3$ films. *Journal of Applied Physics*, 87(5):2394–2399, 2000.

[55] Zhaoliang Liao, Nicolas Gauquelin, Robert J. Green, Sebastian Macke, Julie Gonnissen, Sean Thomas, Zhicheng Zhong, Lin Li, Liang Si, Sandra Van Aert, Philipp Hansmann, Karsten Held, Jing Xia, Johan Verbeeck, Gustaaf Van Tendeloo, George A. Sawatzky, Gertjan Koster, Mark Huijben, and Guus Rijnders. Thickness dependent properties in oxide heterostructures driven by structurally induced metal–oxygen hybridization variations. *Advanced Functional Materials*, 27(17):1606717, 2017.

[56] Teruo Kanki, Hidekazu Tanaka, and Tomoji Kawai. Anomalous strain effect in $La_{0.8}Ba_{0.2}MnO_3$ epitaxial thin film: Role of the orbital degree

of freedom in stabilizing ferromagnetism. *Phys. Rev. B*, 64:224418, Nov 2001.

[57] Qingshan Yuan. Comment on "strain effect and the phase diagram of $La_{1-x}Ba_xMnO_3$ thin films". *Phys. Rev. B*, 70:066401, Aug 2004.

[58] C. H. Ahn, J.-M. Triscone, and J. Mannhart. Electric field effect in correlated oxide systems. *Nature*, 424:1015, 2003.

[59] C. H. Ahn, A. Bhattacharya, M. Di Ventra, J. N. Eckstein, C. Daniel Frisbie, M. E. Gershenson, A. M. Goldman, I. H. Inoue, J. Mannhart, Andrew J. Millis, Alberto F. Morpurgo, Douglas Natelson, and Jean-Marc Triscone. Electrostatic modification of novel materials. *Rev. Mod. Phys.*, 78:1185–1212, Nov 2006.

[60] C. A. F. Vaz, Y. J. Shin, M. Bibes, K. M. Rabe, F. J. Walker, and C. H. Ahn. Epitaxial ferroelectric interfacial devices. *Appl. Phys. Rev.*, 8:041308, 2021.

[61] J. D. Burton and E. Y. Tsymbal. Prediction of electrically induced magnetic reconstruction at the manganite/ferroelectric interface. *Phys. Rev. B*, 80:174406, 11 2009.

[62] X. Hong, A. Posadas, and C. H. Ahn. Examining the screening limit of field effect devices via the metal-insulator transition. *Applied Physics Letters*, 86(14):142501, 03 2005.

[63] Lu Jiang, Woo Seok Choi, Hyoungjeen Jeen, Shuai Dong, Yunseok Kim, Myung-Geun Han, Yimei Zhu, Sergei V. Kalinin, Elbio Dagotto, Takeshi Egami, and Ho Nyung Lee. Tunneling electroresistance induced by interfacial phase transitions in ultrathin oxide heterostructures. *Nano Letters*, 13(12):5837–5843, 2013. PMID: 24205817.

[64] X. Ma, A. Kumar, S. Dussan, H. Zhai, F. Fang, H. B. Zhao, J. F. Scott, R. S. Katiyar, and G. Lüpke. Charge control of antiferromagnetism at $PbZr_{0.52}Ti_{0.48}O_3/La_{0.67}Sr_{0.33}MnO_3$ interface. *Applied Physics Letters*, 104(13):132905, 04 2014.

[65] Steven R. Spurgeon, Prasanna V. Balachandran, Despoina M. Kepaptsoglou, Anoop R. Damodaran, J. Karthik, Siamak Nejati, Lewys Jones, Haile Ambaye, Valeria Lauter, Quentin M. Ramasse, Kenneth K. S. Lau, Lane W. Martin, James M. Rondinelli, and Mitra L. Taheri. Polarization screening-induced magnetic phase gradients at complex oxide interfaces. *Nature Communications*, 6(1):6735, Apr 2015.

[66] Jinling Zhou, Vu Thanh Tra, Shuai Dong, Robbyn Trappen, Matthew A. Marcus, Catherine Jenkins, Charles Frye, Evan Wolfe,

Ryan White, Srinivas Polisetty, Jiunn-Yuan Lin, James M. LeBeau, Ying-Hao Chu, and Mikel Barry Holcomb. Thickness dependence of $La_{0.7}Sr_{0.3}MnO_3/Pb(Zr_{0.2}Ti_{0.8})O_3$ magnetoelectric interfaces. *Applied Physics Letters*, 107(14):141603, 2015.

[67] Weichuan Huang, Yuewei Yin, and Xiaoguang Li. Atomic-scale mapping of interface reconstructions in multiferroic heterostructures. *Applied Physics Reviews*, 5(4):041110, 12 2018.

[68] Binod Paudel, Igor Vasiliev, Mahmoud Hammouri, Dmitry Karpov, Aiping Chen, Valeria Lauter, and Edwin Fohtung. Strain vs. charge mediated magnetoelectric coupling across the magnetic oxide/ferroelectric interfaces. *RSC Adv.*, 9:13033–13041, 2019.

[69] A. Rajapitamahuni, L. L. Tao, Y. Hao, J. Song, X. Xu, E. Y. Tsymbal, and X. Hong. Ferroelectric polarization control of magnetic anisotropy in $PbZr_{0.2}Ti_{0.8}o_3/La_{0.8}Sr_{0.2}Mno_3$ heterostructures. *Phys. Rev. Mater.*, 3:021401, Feb 2019.

[70] Hidekazu Tanaka, Jun Zhang, and Tomoji Kawai. Giant electric field modulation of double exchange ferromagnetism at room temperature in the perovskite manganite/titanate $p-n$ junction. *Phys. Rev. Lett.*, 88:027204, Dec 2001.

[71] Teruo Kanki, Young-Geun Park, Hidekazu Tanaka, and Tomoji Kawai. Electrical-field control of metal–insulator transition at room temperature in $Pb(Zr_{0.2}Ti_{0.8})O_3/La_{1-x}Ba_xMnO_3$ field-effect transistor. *Applied Physics Letters*, 83(23):4860–4862, 2003.

[72] F. X. Hu and J. Gao. Investigations on electroresistance effect in epitaxial manganite films using field effect configurations. *Applied Physics Letters*, 88(13):132502, 2006.

[73] Hanghui Chen and Sohrab Ismail-Beigi. Ferroelectric control of magnetization in $La_{1-x}Sr_xMnO_3$ manganites: A first-principles study. *Phys. Rev. B*, 86:024433, Jul 2012.

[74] Hanghui Chen, Qiao Qiao, Matthew S. J. Marshall, Alexandru B. Georgescu, Ahmet Gulec, Patrick J. Phillips, Robert F. Klie, Frederick J. Walker, Charles H. Ahn, and Sohrab Ismail-Beigi. Reversible modulation of orbital occupations via an interface-induced polar state in metallic manganites. *Nano Letters*, 14(9):4965–4970, 2014. PMID: 25140410.

[75] Daniele Preziosi, Marin Alexe, Dietrich Hesse, and Marco Salluzzo. Electric-field control of the orbital occupancy and magnetic moment of a transition-metal oxide. *Phys. Rev. Lett.*, 115:157401, Oct 2015.

[76] Han Wang, Xiao Chi, ZhongRan Liu, HerngYau Yoong, LingLing Tao, JuanXiu Xiao, Rui Guo, JingXian Wang, ZhiLi Dong, Ping Yang, Cheng-Jun Sun, ChangJian Li, XiaoBing Yan, John Wang, Gan Moog Chow, Evgeny Y. Tsymbal, He Tian, and Jingsheng Chen. Atomic-scale control of magnetism at the titanite-manganite interfaces. *Nano Letters*, 19(5):3057–3065, 2019. PMID: 30964306.

[77] Marius Adrian Husanu, Dana Georgeta Popescu, Federico Bisti, Luminita Mirela Hrib, Lucian Dragos Filip, Iuliana Pasuk, Raluca Negrea, Marian Cosmin Istrate, Leonid Lev, Thorsten Schmitt, Lucian Pintilie, Andrey Mishchenko, Cristian Mihail Teodorescu, and Vladimir N. Strocov. Ferroelectricity modulates polaronic coupling at multiferroic interfaces. *Communications Physics*, 5(1):209, Aug 2022.

[78] Tricia L. Meyer, Andreas Herklotz, Valeria Lauter, John W. Freeland, John Nichols, Er-Jia Guo, Shinbuhm Lee, T. Zac Ward, Nina Balke, Sergei V. Kalinin, Michael R. Fitzsimmons, and Ho Nyung Lee. Enhancing interfacial magnetization with a ferroelectric. *Phys. Rev. B*, 94:174432, 11 2016.

[79] Chao Liu, Yaohua Liu, Bangmin Zhang, Cheng-Jun Sun, Da Lan, Pingfan Chen, Xiaohan Wu, Ping Yang, Xiaojiang Yu, Timothy Charlton, Michael R. Fitzsimmons, Jun Ding, Jingsheng Chen, and Gan Moog Chow. Ferroelectric self-polarization controlled magnetic stratification and magnetic coupling in ultrathin $La_{0.67}Sr_{0.33}MnO_3$ films. *ACS Applied Materials & Interfaces*, 13(25):30137–30145, 2021. PMID: 34137601.

[80] J. Stöhr and H. C. Siegmann. *Magnetism*. Springer-Verlag, Berlin, 2006.

[81] Wolfgang Nolting and Anupuru Ramakanth. *Quantum Theory of Magnetism*. Springer Berlin, Heidelberg, 2009.

[82] Clarence Zener. Interaction between the d-shells in the transition metals. ii. ferromagnetic compounds of manganese with perovskite structure. *Phys. Rev.*, 82:403–405, 05 1951.

[83] P. W. Anderson and H. Hasegawa. Considerations on double exchange. *Phys. Rev.*, 100:675–681, Oct 1955.

[84] P. G. de Gennes. Effects of double exchange in magnetic crystals. *Phys. Rev.*, 118:141–154, Apr 1960.

[85] Tapan Chatterji. *Colossal Magnetoresistive Manganites*. Springer Dordrecht, 2004.

[86] H.A Kramers. L'interaction entre les atomes magnétogènes dans un cristal paramagnétique. *Physica*, 1(1):182–192, 1934.

[87] P. W. Anderson. Antiferromagnetism. theory of superexchange interaction. *Phys. Rev.*, 79:350–356, Jul 1950.

[88] P. W. Anderson. New approach to the theory of superexchange interactions. *Phys. Rev.*, 115:2–13, Jul 1959.

[89] J. B. Goodenough and A. L. Loeb. Theory of ionic ordering, crystal distortion, and magnetic exchange due to covalent forces in spinels. *Phys. Rev.*, 98:391–408, Apr 1955.

[90] Junjiro Kanamori. Superexchange interaction and symmetry properties of electron orbitals. *Journal of Physics and Chemistry of Solids*, 10(2):87–98, 1959.

[91] E. O. Wollan and W. C. Koehler. Neutron diffraction study of the magnetic properties of the series of perovskite-type compounds $[(1-x)\mathrm{La}, x\mathrm{Ca}]\mathrm{Mno}_3$. *Phys. Rev.*, 100:545–563, Oct 1955.

[92] Sumio Ishihara and Sadamichi Maekawa. Theory of orbital excitation and resonant inelastic x-ray scattering in manganites. *Phys. Rev. B*, 62:2338–2345, Jul 2000.

[93] R. Kajimoto, T. Kakeshita, H. Yoshizawa, T. Tanabe, T. Katsufuji, and Y. Tokura. Hole concentration dependence of the ordering process of the stripe order in $\mathrm{La}_{2-x}\mathrm{Sr}_x\mathrm{NiO}_4$. *Phys. Rev. B*, 64:144432, Sep 2001.

[94] O. Chmaissem, B. Dabrowski, S. Kolesnik, J. Mais, J. D. Jorgensen, and S. Short. Structural and magnetic phase diagrams of $\mathrm{La}_{1-x}\mathrm{Sr}_x\mathrm{MnO}_3$ and $\mathrm{Pr}_{1-y}\mathrm{Sr}_y\mathrm{MnO}_3$. *Phys. Rev. B*, 67:094431, 03 2003.

[95] C. A. F. Vaz, J. A. Moyer, D. A. Arena, C. H. Ahn, and V. E. Henrich. Magnetic and electronic structure of ultrathin $\mathrm{La}_{1-x}\mathrm{Sr}_x\mathrm{MnO}_3$ films at half doping. *Phys. Rev. B*, 90:024414, Jul 2014.

[96] C. A. F. Vaz, C. H. Ahn, and V. E. Henrich. Spin-polarisation effects in oxide materials. In A. Hirohata and Y. Otani, editors, *Epitaxial ferromagnetic films and spintronic applications*. Research Signpost, 2009.

[97] J. M. D. Coey, M. Viret, and S. von Molnár. Mixed-valence manganites. *Advances in Physics*, 48(2):167–293, 1999.

[98] Kei Yoshida, Hiroyuki Shiba, Kosaku Yamada, and Akio Sakurai. *Theory of magnetism*. Springer Berlin, Berlin, 1996.

[99] S. Jin, T. H. Tiefel, M. McCormack, R. A. Fastnacht, R. Ramesh, and L. H. Chen. Thousandfold change in resistivity in magnetoresistive La-Ca-Mn-O films. *Science*, 264(5157):413–415, 1994.

[100] A P Ramirez. Colossal magnetoresistance. *Journal of Physics: Condensed Matter*, 9(39):8171, sep 1997.

[101] A. J. Millis, P. B. Littlewood, and B. I. Shraiman. Double exchange alone does not explain the resistivity of $La_{1-x}Sr_xMnO_3$. *Phys. Rev. Lett.*, 74:5144–5147, Jun 1995.

[102] A. J. Millis, Boris I. Shraiman, and R. Mueller. Dynamic jahn-teller effect and colossal magnetoresistance in $La_{1-x}Sr_xMnO_3$. *Phys. Rev. Lett.*, 77:175–178, Jul 1996.

[103] H. Röder, Jun Zang, and A. R. Bishop. Lattice effects in the colossal-magnetoresistance manganites. *Phys. Rev. Lett.*, 76:1356–1359, Feb 1996.

[104] H. Röder, R. R. P. Singh, and J. Zang. High-temperature thermodynamics of the ferromagnetic kondo-lattice model. *Phys. Rev. B*, 56:5084–5087, Sep 1997.

[105] D.S Dessau, Y.D Chuang, A Gromko, T Saitoh, T Kimura, and Y Tokura. Electronic structure of cmr oxides: high resolution electron-spectroscopic studies and a pseudogap. *Journal of Electron Spectroscopy and Related Phenomena*, 117-118:265–276, 2001. Strongly correlated systems.

[106] A J Millis, R Mueller, and B I Shraiman. Fermi-liquid-to-polaron crossover. II. double exchange and the physics of colossal magnetoresistance. *Phys. Rev. B Condens. Matter*, 54(8):5405–5417, August 1996.

[107] A. J. Millis. Lattice effects in magnetoresistive manganese perovskites. *Nature*, 392(6672):147–150, Mar 1998.

[108] A. J. Millis. Comment on "antiferromagnetic short range order in a two-dimensional manganite exhibiting giant magnetoresistance". *Phys. Rev. Lett.*, 80:4358–4358, May 1998.

[109] Takashi Hotta, Seiji Yunoki, Matthias Mayr, and Elbio Dagotto. A-type antiferromagnetic and C-type orbital-ordered states in $LaMnO_3$ using cooperative Jahn-Teller phonons. *Phys. Rev. B*, 60:R15009–R15012, Dec 1999.

[110] Takashi Hotta and Elbio Dagotto. *Theory of Manganites*, pages 207–262. Springer Netherlands, Dordrecht, 2004.

[111] J Park, C T Chen, S W Cheong, W Bao, G Meigs, V Chakarian, V, and Y U Idzerda. Electronic aspects of the ferromagnetic transition in manganese perovskites. *Phys. Rev. Lett.*, 76(22):4215–4218, May 1996.

[112] Y. Tokura. *Colossal magnetoresistive oxides*. CRC Press, 2000.

[113] Y. Okimoto, T. Katsufuji, T. Ishikawa, A. Urushibara, T. Arima, and Y. Tokura. Anomalous variation of optical spectra with spin polarization in double-exchange ferromagnet: $La_{1-x}Sr_xMnO_3$. *Phys. Rev. Lett.*, 75:109–112, Jul 1995.

[114] M. Quijada, J. Černe, J. R. Simpson, H. D. Drew, K. H. Ahn, A. J. Millis, R. Shreekala, R. Ramesh, M. Rajeswari, and T. Venkatesan. Optical conductivity of manganites: Crossover from jahn-teller small polaron to coherent transport in the ferromagnetic state. *Phys. Rev. B*, 58:16093–16102, Dec 1998.

[115] A. Machida, Y. Moritomo, and A. Nakamura. Spectroscopic evidence for formation of small polarons in doped manganites. *Phys. Rev. B*, 58:R4281–R4284, Aug 1998.

[116] S. Satpathy, Zoran S. Popović, and Filip R. Vukajlović. Electronic structure of the perovskite oxides: $La_{1-x}Ca_xMnO_3$. *Phys. Rev. Lett.*, 76:960–963, Feb 1996.

[117] A. E. Bocquet, T. Mizokawa, T. Saitoh, H. Namatame, and A. Fujimori. Electronic structure of 3d-transition-metal compounds by analysis of the 2p core-level photoemission spectra. *Phys. Rev. B*, 46:3771–3784, Aug 1992.

[118] T. Arima, Y. Tokura, and J. B. Torrance. Variation of optical gaps in perovskite-type 3d transition-metal oxides. *Phys. Rev. B*, 48:17006–17009, Dec 1993.

[119] T. Saitoh, A. E. Bocquet, T. Mizokawa, H. Namatame, A. Fujimori, M. Abbate, Y. Takeda, and M. Takano. Electronic structure of $La_{1-x}Sr_xMnO_3$ studied by photoemission and x-ray-absorption spectroscopy. *Phys. Rev. B*, 51:13942–13951, May 1995.

[120] S. Yunoki, A. Moreo, and E. Dagotto. Phase separation induced by orbital degrees of freedom in models for manganites with jahn-teller phonons. *Phys. Rev. Lett.*, 81:5612–5615, Dec 1998.

[121] A. Urushibara, Y. Moritomo, T. Arima, A. Asamitsu, G. Kido, and Y. Tokura. Insulator-metal transition and giant magnetoresistance in $La_{1-x}Sr_xMnO_3$. *Phys. Rev. B*, 51:14103–14109, May 1995.

[122] Masahito Mochizuki and Masatoshi Imada. Orbital physics in the perovskite ti oxides. *New Journal of Physics*, 6(1):154, nov 2004.

[123] Karin M. Rabe, Matthew Dawber, Céline Lichtensteiger, Charles H. Ahn, and Jean-Marc Triscone. *Modern Physics of Ferroelectrics:Essential Background*, pages 1–30. Springer Berlin Heidelberg, Berlin, Heidelberg, 2007.

[124] Vincenzo Buscaglia and Clive A. Randall. Size and scaling effects in barium titanate. an overview. *Journal of the European Ceramic Society*, 40(11):3744–3758, 2020. 16th European Inter-Regional Conference on Ceramics (CIEC16).

[125] Jonathan E. Spanier, Alexie M. Kolpak, Jeffrey J. Urban, Ilya Grinberg, Lian Ouyang, Wan Soo Yun, Andrew M. Rappe, and Hongkun Park. Ferroelectric phase transition in individual single-crystalline $BaTiO_3$ nanowires. *Nano Letters*, 6(4):735–739, 2006. PMID: 16608274.

[126] L. W. Chang, M. McMillen, F. D. Morrison, J. F. Scott, and J. M. Gregg. Size effects on thin film ferroelectrics: Experiments on isolated single crystal sheets. *Applied Physics Letters*, 93(13):132904, 10 2008.

[127] Javier Junquera and Philippe Ghosez. Critical thickness for ferroelectricity in perovskite ultrathin films. *Nature*, 422(6931):506–509, Apr 2003.

[128] Y. S. Kim, D. H. Kim, J. D. Kim, Y. J. Chang, T. W. Noh, J. H. Kong, K. Char, Y. D. Park, S. D. Bu, J.-G. Yoon, and J.-S. Chung. Critical thickness of ultrathin ferroelectric $BaTiO_3$ films. *Applied Physics Letters*, 86(10):102907, 03 2005.

[129] C A F Vaz. Electric field control of magnetism in multiferroic heterostructures. *Journal of Physics: Condensed Matter*, 24(33):333201, jul 2012.

[130] George T. Rado. Statistical theory of magnetoelectric effects in antiferromagnetics. *Phys. Rev.*, 128:2546–2556, Dec 1962.

[131] W. F. Brown, R. M. Hornreich, and S. Shtrikman. Upper bound on the magnetoelectric susceptibility. *Phys. Rev.*, 168:574–577, Apr 1968.

[132] C A F Vaz, F J Walker, C H Ahn, and S Ismail-Beigi. Intrinsic interfacial phenomena in manganite heterostructures. *Journal of Physics: Condensed Matter*, 27(12):123001, feb 2015.

[133] G. Srinivasan. Magnetoelectric composites. *Annual Review of Materials Research*, 40(1):153–178, 2010.

[134] K.F. Wang, J.-M. Liu, and Z.F. Ren. Multiferroicity: the coupling between magnetic and polarization orders. *Advances in Physics*, 58(4):321–448, 2009.

[135] Ce-Wen Nan, M. I. Bichurin, Shuxiang Dong, D. Viehland, and G. Srinivasan. Multiferroic magnetoelectric composites: Historical perspective, status, and future directions. *Journal of Applied Physics*, 103(3):031101, 02 2008.

[136] Shashank Priya, Rashed Islam, Shuxiang Dong, and D. Viehland. Recent advancements in magnetoelectric particulate and laminate composites. *Journal of Electroceramics*, 19(1):149–166, Sep 2007.

[137] Ramamoorthy Ramesh and Sasikanth Manipatruni. Electric field control of magnetism. *Proceedings of the Royal Society A: Mathematical, Physical and Engineering Sciences*, 477(2251):20200942, 2021.

[138] V. Novosad, Y. Otani, A. Ohsawa, S. G. Kim, K. Fukamichi, J. Koike, K. Maruyama, O. Kitakami, and Y. Shimada. Novel magnetostrictive memory device. *Journal of Applied Physics*, 87(9):6400–6402, 05 2000.

[139] N A Pertsev and H Kohlstedt. Resistive switching via the converse magnetoelectric effect in ferromagnetic multilayers on ferroelectric substrates. *Nanotechnology*, 21(47):475202, oct 2010.

[140] C. Cavaco, M. van Kampen, L. Lagae, and G. Borghs. A room-temperature electrical field–controlled magnetic memory cell. *Journal of Materials Research*, 22(8):2111–2115, Aug 2007.

[141] N. A. Pertsev and H. Kohlstedt. Magnetic tunnel junction on a ferroelectric substrate. *Applied Physics Letters*, 95(16):163503, 10 2009.

[142] J Nogués and Ivan K Schuller. Exchange bias. *Journal of Magnetism and Magnetic Materials*, 192(2):203–232, 1999.

[143] A Hochstrat, Ch Binek, Xi Chen, and W Kleemann. Extrinsic control of the exchange bias. *Journal of Magnetism and Magnetic Materials*, 272-276:325–326, 2004. Proceedings of the International Conference on Magnetism (ICM 2003).

[144] Pavel Borisov, Andreas Hochstrat, Xi Chen, Wolfgang Kleemann, and Christian Binek. Magnetoelectric switching of exchange bias. *Phys. Rev. Lett.*, 94:117203, Mar 2005.

[145] Hajo J. A. Molegraaf, Jason Hoffman, Carlos A. F. Vaz, Stefano Gariglio, Dirk van der Marel, Charles H. Ahn, and Jean-Marc Triscone. Magnetoelectric effects in complex oxides with competing ground states. *Advanced Materials*, 21(34):3470–3474, 2009.

[146] C. A. F. Vaz, Y. Segal, J. Hoffman, R. D. Grober, F. J. Walker, and C. H. Ahn. Temperature dependence of the magnetoelectric effect in $Pb(Zr_{0.2}Ti_{0.8})O_3/La_{0.8}Sr_{0.2}MnO_3$ multiferroic heterostructures. *Applied Physics Letters*, 97(4):042506, 07 2010.

[147] William Nunn, Tristan K. Truttmann, and Bharat Jalan. A review of molecular-beam epitaxy of wide bandgap complex oxide semiconductors. *Journal of Materials Research*, 36(23):4846–4864, Dec 2021.

[148] Charles M Gilmore and James A Sprague. Molecular dynamics simulation of defect formation during energetic Cu deposition. *Thin Solid Films*, 419(1-2):18 – 26, 2002.

[149] Duan-Ming Zhang, Li Guan, Bo-Ming Yu, and Zhi-Hua Li. Monte carlo simulation of growth of thin film prepared by pulsed laser. *Chinese Physics Letters*, 20(2):263 – 266, 2003. Cited by: 7.

[150] Tsuyoshi Ohnishi, Keisuke Shibuya, Takahisa Yamamoto, and Mikk Lippmaa. Defects and transport in complex oxide thin films. *Journal of Applied Physics*, 103(10), 05 2008. 103703.

[151] Secondo Franchi. Chapter 1 - molecular beam epitaxy: fundamentals, historical background and future prospects. In Mohamed Henini, editor, *Molecular Beam Epitaxy*, pages 1–46. Elsevier, Oxford, 2013.

[152] Martin Knudsen. Die maximale verdampfungsgeschwindigkeit des quecksilbers. *Annalen der Physik*, 352(13):697–708, 1915.

[153] Irving Langmuir. The vapor pressure of metallic tungsten. *Phys. Rev.*, 2:329–342, Nov 1913.

[154] Scott A. Chambers. Epitaxial growth and properties of thin film oxides. *Surface Science Reports*, 39(5):105–180, 2000.

[155] E. Bauer and Jan H. van der Merwe. Structure and growth of crystalline superlattices: From monolayer to superlattice. *Phys. Rev. B*, 33:3657–3671, Mar 1986.

[156] Jr. Egelhoff, W. F. and D. A. Steigerwald. The role of adsorbed gases in metal on metal epitaxy. *Journal of Vacuum Science & Technology A*, 7(3):2167–2173, 05 1989.

[157] Ayahiko Ichimiya and Philip I. Cohen. *Reflection High-Energy Electron Diffraction*. Cambridge University Press, 2004.

[158] Shuji Hasegawa. *Reflection High-Energy Electron Diffraction*, pages 1–14. John Wiley & Sons, Ltd, 2012.

[159] M. Kareev, S. Prosandeev, J. Liu, C. Gan, A. Kareev, J. W. Freeland, Min Xiao, and J. Chakhalian. Atomic control and characterization of surface defect states of TiO_2 terminated $SrTiO_3$ single crystals. *Applied Physics Letters*, 93(6):061909, 2008.

[160] Jun Zhang, D. Doutt, T. Merz, J. Chakhalian, M. Kareev, J. Liu, and L. J. Brillson. Depth-resolved subsurface defects in chemically etched $SrTiO_3$. *Applied Physics Letters*, 94(9):092904, 2009.

[161] Joseph H. Ngai, Todd C. Schwendemann, Anna E. Walker, Yaron Segal, Fred J. Walker, Eric I. Altman, and Charles H. Ahn. Achieving a-site termination on $La_{0.18}Sr_{0.82}Al_{0.59}Ta_{0.41}O_3$ substrates. *Advanced Materials*, 22(26-27):2945–2948, 2010.

[162] H Seiler. Secondary electron emission in the scanning electron microscope. *Journal of Applied Physics*, 54(11):R1–R18, 11 1983.

[163] John David Jackson. *Classical electrodynamics*. J. Wiley, New York [etc, 1962 - 1962.

[164] Paolo Carra, B. T. Thole, Massimo Altarelli, and Xindong Wang. X-ray circular dichroism and local magnetic fields. *Phys. Rev. Lett.*, 70:694–697, Feb 1993.

[165] B. T. Thole, P. Carra, F. Sette, and G. van der Laan. X-ray circular dichroism as a probe of orbital magnetization. *Phys. Rev. Lett.*, 68:1943–1946, Mar 1992.

[166] J P Crocombette, B T Thole, and F Jollet. The importance of the magnetic dipole term in magneto-circular x-ray absorption dichroism for 3d transition metal compounds. *Journal of Physics: Condensed Matter*, 8(22):4095, may 1996.

[167] Cinthia Piamonteze, Piter Miedema, and Frank M. F. de Groot. Accuracy of the spin sum rule in xmcd for the transition-metal l edges from manganese to copper. *Phys. Rev. B*, 80:184410, Nov 2009.

[168] Akinobu Yamaguchi, Atsufumi Hirohata, and Bethanie J.H. Stadler, editors. *X-ray techniques to characterize nanomagnetism*, pages 199–303. Micro and Nano Technologies. Elsevier, 2021.

[169] Jun Feng and Andreas Scholl. *Photoemission Electron Microscopy (PEEM)*, pages 657–695. Springer New York, New York, NY, 2007.

[170] W. Kuch. *Imaging Magnetic Microspectroscopy*, pages 1–28. Springer Berlin Heidelberg, Berlin, Heidelberg, 2005.

[171] M. P. Seah and W. A. Dench. Quantitative electron spectroscopy of surfaces: A standard data base for electron inelastic mean free paths in solids. *Surface and Interface Analysis*, 1(1):2–11, 1979.

[172] Daniela Leanza, Carlos A. F. Vaz, Izabela Czekaj, Petr Novák, and Mario El Kazzi. Solving the puzzle of li4ti5o12 surface reactivity in aprotic electrolytes in li-ion batteries by nanoscale xpeem spectromicroscopy. *J. Mater. Chem. A*, 6:3534–3542, 2018.

[173] Stefan Hüfner. *Photoelectron Spectroscopy*. Springer-Verlag, 2003.

[174] Andrea Damascelli, Zahid Hussain, and Zhi-Xun Shen. Angle-resolved photoemission studies of the cuprate superconductors. *Rev. Mod. Phys.*, 75:473–541, Apr 2003.

[175] Simon Moser. An experimentalist's guide to the matrix element in angle resolved photoemission. *Journal of Electron Spectroscopy and Related Phenomena*, 214:29–52, 2017.

[176] Baiqing Lv, Tian Qian, and Hong Ding. Angle-resolved photoemission spectroscopy and its application to topological materials. *Nature Reviews Physics*, 1(10):609–626, Oct 2019.

[177] Eryin. Wang. *Angle-Resolved Photoemission Spectroscopy Studies of 2D Material Heterostructures*. Springer Theses, Recognizing Outstanding Ph.D. Research. Springer Singapore, Singapore, 1st ed. 2020. edition, 2020.

[178] Shigemasa Suga. *Photoelectron spectroscopy : : bulk and surface electronic structures*. Springer series in surface sciences ; Volume 72. Springer, Cham, Switzerland, second edition. edition, 2021.

[179] A. Sekiyama, S. Kasai, M. Tsunekawa, Y. Ishida, M. Sing, A. Irizawa, A. Yamasaki, S. Imada, T. Muro, Y. Saitoh, Y. Ōnuki, T. Kimura, Y. Tokura, and S. Suga. Technique for bulk fermiology by photoemission applied to layered ruthenates. *Phys. Rev. B*, 70:060506, Aug 2004.

[180] S. Suga, A. Shigemoto, A. Sekiyama, S. Imada, A Yamasaki, A. Irizawa, S. Kasai, Y. Saitoh, T. Muro, N. Tomita, K. Nasu, H. Eisaki, and Y. Ueda. High-energy angle-resolved photoemission spectroscopy probing bulk correlated electronic states in quasi-one-dimensional V_6O_{13} and $SrCuO_2$. *Phys. Rev. B*, 70:155106, Oct 2004.

[181] V.N. Strocov, L.L. Lev, M. Kobayashi, C. Cancellieri, M.-A. Husanu, A. Chikina, N.B.M. Schröter, X. Wang, J.A. Krieger, and Z. Salman. k-resolved electronic structure of buried heterostructure and impurity

systems by soft-x-ray ARPES. *Journal of Electron Spectroscopy and Related Phenomena*, 236:1–8, 2019.

[182] E. Dietz, H. Becker, and U. Gerhardt. Polarization dependence of angular-resolved photoemission from *d* bands of Cu. *Phys. Rev. Lett.*, 36:1397–1399, Jun 1976.

[183] J. Hermanson. Final-state symmetry and polarization effects in angle-resolved photoemission spectroscopy. *Solid State Communications*, 22(1):9–11, 1977.

[184] W. Eberhardt and F. J. Himpsel. Dipole selection rules for optical transitions in the fcc and bcc lattices. *Phys. Rev. B*, 21:5572–5576, Jun 1980.

[185] Eric L. Shirley, L. J. Terminello, A. Santoni, and F. J. Himpsel. Brillouin-zone-selection effects in graphite photoelectron angular distributions. *Phys. Rev. B*, 51:13614–13622, May 1995.

[186] Aaron Bostwick, Taisuke Ohta, Thomas Seyller, Karsten Horn, and Eli Rotenberg. Quasiparticle dynamics in graphene. *Nature Physics*, 3(1):36–40, Jan 2007.

[187] Aaron Bostwick, Taisuke Ohta, Jessica L McChesney, Konstantin V Emtsev, Thomas Seyller, Karsten Horn, and Eli Rotenberg. Symmetry breaking in few layer graphene films. *New Journal of Physics*, 9(10):385, oct 2007.

[188] M. Mucha-Kruczyński, O. Tsyplyatyev, A. Grishin, E. McCann, Vladimir I. Fal'ko, Aaron Bostwick, and Eli Rotenberg. Characterization of graphene through anisotropy of constant-energy maps in angle-resolved photoemission. *Phys. Rev. B*, 77:195403, May 2008.

[189] Isabella Gierz, Takayuki Suzuki, R. Thomas Weitz, Dong Su Lee, Benjamin Krauss, Christian Riedl, Ulrich Starke, Hartmut Höchst, Jurgen H. Smet, Christian R. Ast, and Klaus Kern. Electronic decoupling of an epitaxial graphene monolayer by gold intercalation. *Phys. Rev. B*, 81:235408, Jun 2010.

[190] W. S. Jung, C. S. Leem, Chul Kim, S. R. Park, S. Y. Park, B. J. Kim, E. Rotenberg, and C. Kim. Imaging the electron density in solids by using multi-brillouin-zone angle resolved photoelectron spectroscopy. *Phys. Rev. B*, 82:235105, Dec 2010.

[191] J. Voit, L. Perfetti, F. Zwick, H. Berger, G. Margaritondo, G. Grüner, H. Höchst, and M. Grioni. Electronic structure of solids with competing periodic potentials. *Science*, 290(5491):501–503, 2000.

[192] Anshuman Pal and E. J. Mele. Nodal surfaces in photoemission from twisted bilayer graphene. *Phys. Rev. B*, 87:205444, May 2013.

[193] J. P. Hill and D. F. McMorrow. Resonant exchange scattering: Polarization dependence and correlation function. *Acta Crystallographica Section A*, 52(2):236–244, 1996.

[194] J Fink, E Schierle, E Weschke, and J Geck. Resonant elastic soft x-ray scattering. *Reports on Progress in Physics*, 76(5):056502, 2013.

[195] M. Elzo, E. Jal, O. Bunau, S. Grenier, Y. Joly, A.Y. Ramos, H.C.N. Tolentino, J.M. Tonnerre, and N. Jaouen. X-ray resonant magnetic reflectivity of stratified magnetic structures: Eigenwave formalism and application to a W/Fe/W trilayer. *Journal of Magnetism and Magnetic Materials*, 324(2):105–112, 2012.

[196] A. Kramida, Yu. Ralchenko, J. Reader, and NIST ASD Team. Nist atomic spectra database (version 5.10), [online]. *National Institute of Standards and Technology, Gaithersburg, MD.*, 2022.

[197] Piers Coleman. *Fluctuation–dissipation theorem and linear response theory*, page 292–331. Cambridge University Press, 2015.

[198] L. J. van der Pauw. A method of measuring specific resistivity and hall effect of discs of arbitrary shape. *Philips Res. Repts.*, 13:1, 1958.

[199] L. J. van der Pauw. A method of measuring the resistivity and hall coefficient of lamellae of arbitrary shape. *Philips Tech. Rev.*, 20:220, 1958.

[200] U. Flechsig, F. Nolting, A. Fraile Rodríguez, J. Krempaský, C. Quitmann, T. Schmidt, S. Spielmann, and D. Zimoch. Performance measurements at the SLS SIM beamline. *AIP Conference Proceedings*, 1234(1):319–322, 06 2010.

[201] Cinthia Piamonteze, Uwe Flechsig, Stefano Rusponi, Jan Dreiser, Jakoba Heidler, Marcus Schmidt, Reto Wetter, Marco Calvi, Thomas Schmidt, Helena Pruchova, Juraj Krempasky, Christoph Quitmann, Harald Brune, and Frithjof Nolting. X-Treme beamline at SLS: X-ray magnetic circular and linear dichroism at high field and low temperature. *Journal of Synchrotron Radiation*, 19(5):661–674, Sep 2012.

[202] V N Strocov, X Wang, M Shi, M Kobayashi, J Krempasky, C Hess, T Schmitt, and L Patthey. Soft-X-ray ARPES facility at the ADRESS beamline of the SLS: concepts, technical realisation and scientific applications. *J Synchrotron Radiat*, 21(Pt 1):32–44, November 2013.

[203] F. Stramaglia, G. Panchal, F. Nolting, and C. A. F. Vaz. Fully magnetically polarized ultrathin $La_{0.8}Sr_{0.2}MnO_3$ films. *ACS Applied Materials & Interfaces*, 16(3):4138–4149, 2024.

[204] F. Stramaglia, G. Panchal, F. Nolting, and C. A. F. Vaz. Origin of magnetism in epitaxial ultrathin $LaMnO_3$ films. 2023. Unpublished.

[205] G. Panchal, F. Stramaglia, F. Nolting, and C. A. F. Vaz. Magnetic state crossover in $La_{0.8}Sr_{0.2}MnO_3/La_{0.45}Sr_{0.55}MnO_3$ bilayer structures. 2023. Unpublished.

[206] Pavlo Zubko, Stefano Gariglio, Marc Gabay, Philippe Ghosez, and Jean-Marc Triscone. Interface physics in complex oxide heterostructures. *Annual Review of Condensed Matter Physics*, 2(1):141–165, 2011.

[207] C. A. F. Vaz, J. A. C. Bland, and G. Lauhoff. Magnetism in ultrathin film structures. *Rep. Prog. Phys.*, 71:056501, 2008.

[208] Pei-Xin Qin, Han Yan, Xiao-Ning Wang, Ze-Xin Feng, Hui-Xin Guo, Xiao-Rong Zhou, Hao-Jiang Wu, Xin Zhang, Zhao-Guo-Gang Leng, Hong-Yu Chen, and Zhi-Qi Liu. Noncollinear spintronics and electric-field control: a review. *Rare Metals*, 39(2):95–112, Feb 2020.

[209] Yaqing Feng, Kui-juan Jin, Lin Gu, Xu He, Chen Ge, Qing-hua Guo, Zhang, Min He, Qin-lin Guo, Qian Wan, Meng He, Hui-bin Lu, and Guozhen Yang. Insulating phase at low temperature in ultrathin $La_{0.8}Sr_{0.2}MnO_3$ films. *Scientific Reports*, 6:1, 3 2016.

[210] Hongyan Chen, Yang Yu, Zhe Wang, Yu Bai, Hanxuan Lin, Xiaolong Li, Hao Liu, Tian Miao, Yunfang Kou, Yongsheng Zhang, Yan Li, Jin Tang, Zechao Wang, Peng Cai, Yinyan Zhu, Zhaohua Cheng, Xiaoyan Zhong, Wenbin Wang, Xingyu Gao, Lifeng Yin, Ruqian Wu, and Jian Shen. Thickness-driven first-order phase transitions in manganite ultrathin films. *Phys. Rev. B*, 99:214419, Jun 2019.

[211] C. A. F. Vaz, A. Kleibert, and M. El Kazzi. Nanoscale xpeem spectromicroscopy. In K. D. Sattler, editor, *21st CENTURY NANOSCIENCE – A HANDBOOK*, chapter 17. Taylor & Francis (CRC Press), 2020.

[212] H Zenia, G A Gehring, and W M Temmerman. Orbital ordering in cubic $LaMnO_3$ from first principles calculations. *New Journal of Physics*, 7(1):257, dec 2005.

[213] Y. S. Hou, H. J. Xiang, and X. G. Gong. Intrinsic insulating ferromagnetism in manganese oxide thin films. *Phys. Rev. B*, 89:064415, Feb 2014.

[214] Ming An, Yakui Weng, Huimin Zhang, Jun-Jie Zhang, Yang Zhang, and Shuai Dong. Appearance and disappearance of ferromagnetism in ultrathin $LaMnO_3$ on $SrTiO_3$ substrate: A viewpoint from first principles. *Phys. Rev. B*, 96:235112, Dec 2017.

[215] J. Rodríguez-Carvajal, M. Hennion, F. Moussa, A. H. Moudden, L. Pinsard, and A. Revcolevschi. Neutron-diffraction study of the Jahn-Teller transition in stoichiometric $LaMnO_3$. *Phys. Rev. B*, 57:R3189–R3192, Feb 1998.

[216] C. A. F. Vaz, J. Hoffman, Y. Segal, M. S. J. Marshall, J. W. Reiner, Z. Zhang, R. D. Grober, F. J. Walker, and C. H. Ahn. Control of magnetism in $Pb(Zr_{0.2}Ti_{0.8})O_3/La_{0.8}Sr_{0.2}MnO_3$ multiferroic heterostructures (invited). *Journal of Applied Physics*, 109(7):07D905, 2011.

[217] X. Renshaw Wang, C. J. Li, W. M. Lü, T. R. Paudel, D. P. Leusink, M. Hoek, N. Poccia, A. Vailionis, T. Venkatesan, J. M. D. Coey, E. Y. Tsymbal, null Ariando, and H. Hilgenkamp. Imaging and control of ferromagnetism in $LaMnO_3/SrTiO_3$ heterostructures. *Science*, 349(6249):716–719, 2015.

[218] Ruiqiang Zhao, Kuijuan Jin, Zhongtang Xu, Haizhong Guo, Le Wang, Chen Ge, Huibin Lu, and Guozhen Yang. The oxygen vacancy effect on the magnetic property of the $LaMnO_{3-\delta}$ thin films. *Applied Physics Letters*, 102(12):122402, 2013.

[219] H. Kawano, R. Kajimoto, M. Kubota, and H. Yoshizawa. Ferromagnetism-induced reentrant structural transition and phase diagram of the lightly doped insulator $La_{1-x}Sr_xMnO_3$ ($x <\sim 0.17$). *Phys. Rev. B*, 53:R14709–R14712, Jun 1996.

[220] B. Dabrowski, X. Xiong, Z. Bukowski, R. Dybzinski, P. W. Klamut, J. E. Siewenie, O. Chmaissem, J. Shaffer, C. W. Kimball, J. D. Jorgensen, and S. Short. Structure-properties phase diagram for $La_{1-x}Sr_xMnO_3$ ($0.1 <\sim x <\sim 0.2$). *Phys. Rev. B*, 60:7006–7017, Sep 1999.

[221] N. -H. Chan, R. K. Sharma, and D. M. Smyth. Nonstoichiometry in srtio3. *Journal of The Electrochemical Society*, 128(8):1762, aug 1981.

[222] F. Song, Å. F. Monsen, Z. S. Li, J. W. Wells, and E. Wahlström. The layer-by-layer stoichiometry of $La_{0.7}Sr_{0.3}MnO_3/SrTiO_3$ thin films and interfaces. *Surface and Interface Analysis*, 45(7):1144–1147, 2013.

[223] Jens E. T. Andersen and Preben J. Mo/ller. Impurity-induced 900°C (2×2) surface reconstruction of $SrTiO_3(100)$. *Applied Physics Letters*, 56(19):1847–1849, 05 1990.

[224] Bonjae Koo, Kyeounghak Kim, Jun Kyu Kim, Hyunguk Kwon, Jeong Woo Han, and WooChul Jung. Sr segregation in perovskite oxides: Why it happens and how it exists. *Joule*, 2(8):1476–1499, 2018.

[225] M. Pajda, J. Kudrnovský, I. Turek, V. Drchal, and P. Bruno. Oscillatory curie temperature of two-dimensional ferromagnets. *Phys. Rev. Lett.*, 85:5424–5427, Dec 2000.

[226] S. S. A. Razee, J. B. Staunton, L. Szunyogh, and B. L. Györffy. Local moments and magnetic correlations above the curie temperature in thin films on and embedded in nonmagnetic substrates: Fe/Cu(100), Co/Cu(100), and Fe/W(100). *Phys. Rev. B*, 66:094415, 2002.

[227] S. E. Lofland, S. M. Bhagat, K. Ghosh, R. L. Greene, S. G. Karabashev, D. A. Shulyatev, A. A. Arsenov, and Y. Mukovskii. Magnetic transition and electronic transport in colossal magnetoresistance perovskites. *Phys. Rev. B*, 56:13705–13707, Dec 1997.

[228] T. S. Santos, S. J. May, J. L. Robertson, and A. Bhattacharya. Tuning between the metallic antiferromagnetic and ferromagnetic phases of $La_{1-x}Sr_xMnO_3$ near $x = 0.5$ by digital synthesis. *Phys. Rev. B*, 80:155114, 2009.

[229] Y. Segal, K. F. Garrity, C. A. F. Vaz, J. D. Hoffman, F. J. Walker, S. Ismail-Beigi, and C. H. Ahn. Dynamic evanescent phonon coupling across the $La_{1-x}Sr_xMnO_3/SrTiO_3$ interface. *Phys. Rev. Lett.*, 107:105501, Aug 2011.

[230] B. Gilbert, B. H. Frazer, A. Belz, P. G. Conrad, K. H. Nealson, D. Haskel, J. C. Lang, G. Srajer, and G. De Stasio. Multiple scattering calculations of bonding and x-ray absorption spectroscopy of manganese oxides. *The Journal of Physical Chemistry A*, 107(16):2839–2847, 2003.

[231] T. Burnus, Z. Hu, H. H. Hsieh, V. L. J. Joly, P. A. Joy, M. W. Haverkort, Hua Wu, A. Tanaka, H.-J. Lin, C. T. Chen, and L. H. Tjeng. Local electronic structure and magnetic properties of $LaMn_{0.5}Co_{0.5}O_3$ studied by x-ray absorption and magnetic circular dichroism spectroscopy. *Phys. Rev. B*, 77:125124, Mar 2008.

[232] M. Abbate, F. M. F. de Groot, J. C. Fuggle, A. Fujimori, O. Strebel, F. Lopez, M. Domke, G. Kaindl, G. A. Sawatzky, M. Takano, Y. Takeda, H. Eisaki, and S. Uchida. Controlled-valence properties of $La_{1-x}Sr_xFeO_3$ and $La_{1-x}Sr_xMnO_3$ studied by soft-x-ray absorption spectroscopy. *Phys. Rev. B*, 46:4511–4519, Aug 1992.

[233] John B. Goodenough. Theory of the role of covalence in the perovskite-type manganites [La, M(II)]MnO_3. *Phys. Rev.*, 100:564–573, Oct 1955.

[234] F. M. F. de Groot, M. Grioni, J. C. Fuggle, J. Ghijsen, G. A. Sawatzky, and H. Petersen. Oxygen 1s x-ray-absorption edges of transition-metal oxides. *Phys. Rev. B*, 40:5715–5723, Sep 1989.

[235] C. Aruta, G. Ghiringhelli, A. Tebano, N. G. Boggio, N. B. Brookes, P. G. Medaglia, and G. Balestrino. Strain induced x-ray absorption linear dichroism in $La_{0.7}Sr_{0.3}MnO_3$ thin films. *Phys. Rev. B*, 73:235121, Jun 2006.

[236] E. Pellegrin, L. H. Tjeng, F. M. F. de Groot, R. Hesper, G. A. Sawatzky, Y. Moritomo, and Y. Tokura. Soft x-ray magnetic circular dichroism study of the colossal magnetoresistance compound $La_{1-x}Sr_xMnO-3$. *Journal of Electron Spectroscopy and Related Phenomena*, 86:115, 1997.

[237] Y. Konishi, Z. Fang, M. Izumi, T. Manako, M. Kasai, H. Kuwahara, M. Kawasaki, K. Terakura, and Y. Tokura. Orbital-state-mediated phase-control of manganites. *J. Phys. Soc. Japan*, 68:3790, 1999.

[238] M. D. Núñez Regueiro, M. Altarelli, and C. T. Chen. X-ray-absorption sum rule for linear dichroism: Application to high-t_c cuprate oxides. *Phys. Rev. B*, 51:629–631, Jan 1995.

[239] Aruta, C., Balestrino, G., Tebano, A., Ghiringhelli, G., and Brookes, N. B. Cooperative enhancement of in-plane orbital ordering by oxygen deficiency and in-plane tensile strain in $La_{0.7}Sr_{0.3}MnO_{3-\delta}$ thin films. *EPL*, 80(3):37003, 2007.

[240] B. R. K. Nanda and S. Satpathy. Effects of strain on orbital ordering and magnetism at perovskite oxide interfaces: $LaMnO_3/SrMnO_3$. *Phys. Rev. B*, 78:054427, 2008.

[241] X. Zhai, . Cheng, Y. Liu, C. M. Schlepütz, S. Dong, H. Li, X. Zhang, S. Chu, L. Zheng, J. Zhang, A. Zhao, H. Hong, A. Bhattacharya, J. N. Eckstein, and C. Zeng. Correlating interfacial octahedral rotations with magnetism in $(LaMnO_3)N/(SrTiO_3)N$ superlattices. *Nat. Commun.*, 5:4283, 2014.

[242] F. Stramaglia, G. Panchal, L. Tovaglieri, C. Lichtensteiger, F. Nolting, and C. A. F. Vaz. Direct imaging of the magnetoelectric coupling in $BaTiO_3/La_{0.8}Sr_{0.2}MnO_3$ multiferroic heterostructures. 2023. Unpublished.

[243] T. A. Kaplan and S. D. Mahanti, editors. *Physics of Manganites*. Kluwer Academic Publishers, New York, 2002.

[244] G.H. Jonker and J.H. Van Santen. Ferromagnetic compounds of manganese with perovskite structure. *Physica*, 16(3):337–349, 1950.

[245] Hidekazu Tanaka, Jun Zhang, and Tomoji Kawai. Giant electric field modulation of double exchange ferromagnetism at room temperature in the perovskite manganite/titanate $p-n$ junction. *Phys. Rev. Lett.*, 88:027204, Dec 2001.

[246] Teruo Kanki, Hidekazu Tanaka, and Tomoji Kawai. Electric control of room temperature ferromagnetism in a $Pb(Zr_{0.2}Ti_{0.8})O_3/La_{0.85}Ba_{0.15}MnO_3$ field-effect transistor. *Applied Physics Letters*, 89(24):242506, 2006.

[247] Céline Lichtensteiger, Stéphanie Fernandez-Pena, Christian Weymann, Pavlo Zubko, and Jean-Marc Triscone. Tuning of the depolarization field and nanodomain structure in ferroelectric thin films. *Nano Letters*, 14(8):4205–4211, 2014.

[248] Céline Lichtensteiger, Christian Weymann, Stéphanie Fernandez-Pena, Patrycja Paruch, and Jean-Marc Triscone. Built-in voltage in thin ferroelectric $PbTiO_3$ films: the effect of electrostatic boundary conditions. *New Journal of Physics*, 18(4):043030, apr 2016.

[249] D. H. Dickey. Two-point probe correction factors. *National Bureau of Standards Special Publication*, 400-10:45, 1974. DOI: 10.1520/STP47393S.

[250] H.L Ju, Y.S Nam, J.E Lee, and H.S Shin. Anomalous magnetic properties and magnetic phase diagram of $La_{1-x}Ba_xMnO_3$. *Journal of Magnetism and Magnetic Materials*, 219(1):1–8, 2000.

[251] P. Mandal and B. Ghosh. Transport, magnetic, and structural properties of $La_{1-x}M_xMnO_3$ (M = Ba, Sr, Ca) for $0 <\sim x <\sim 0.20$. *Phys. Rev. B*, 68:014422, Jul 2003.

[252] A. Barbier, C. Mocuta, D. Stanescu, P. Jegou, N. Jedrecy, and H. Magnan. Surface composition of $BaTiO_3/SrTiO_3(001)$ films grown by atomic oxygen plasma assisted molecular beam epitaxy. *Journal of Applied Physics*, 112(11):114116, 2012.

[253] Federica Frati, Myrtille O. J. Y. Hunault, and Frank M. F. de Groot. Oxygen K-edge x-ray absorption spectra. *Chemical Reviews*, 120(9):4056–4110, 2020.

[254] D. Pesquera, G. Herranz, and A. et al. Barla. Surface symmetry-breaking and strain effects on orbital occupancy in transition metal perovskite epitaxial films. *Nature Communications*, 3, 2012.

[255] F. V.E. Hensling, T. Heisig, N. Raab, C. Baeumer, and R. Dittmann. Tailoring the switching performance of resistive switching $SrTiO_3$ devices by SrO interface engineering. *Solid state ionics*, 325:247–250, November 2018.

[256] Laura Elena Ştoflea, Nicoleta Georgiana Apostol, Lucian Trupină, and Cristian Mihail Teodorescu. Selective adsorption of contaminants on $Pb(Zr,Ti)O_3$ surfaces shown by x-ray photoelectron spectroscopy. *J. Mater. Chem. A*, 2:14386–14392, 2014.

[257] J. Krempaský, V.N. Strocov, P. Blaha, L. Patthey, M. Radović, M. Falub, M. Shi, and K. Hricovini. Bulk vs. surface effects in ARPES experiment from $La_{2/3}Sr_{1/3}MnO_3$ thin films. *Journal of Electron Spectroscopy and Related Phenomena*, 181(1):63–69, 2010. Proceedings of International Workshop on Strong Correlations and Angle-Resolved Photoemission Spectroscopy 2009.

[258] L. L. Lev, J. Krempaský, U. Staub, V. A. Rogalev, T. Schmitt, M. Shi, P. Blaha, A. S. Mishchenko, A. A. Veligzhanin, Y. V. Zubavichus, M. B. Tsetlin, H. Volfová, J. Braun, J. Minár, and V. N. Strocov. Fermi surface of three-dimensional $La_{1-x}Sr_xMnO_3$ explored by soft-x-ray arpes: Rhombohedral lattice distortion and its effect on magnetoresistance. *Phys. Rev. Lett.*, 114:237601, Jun 2015.

[259] S. de Jong, Y. Huang, I. Santoso, F. Massee, R. Follath, O. Schwarzkopf, L. Patthey, M. Shi, and M. S. Golden. Quasiparticles and anomalous temperature dependence of the low-lying states in the colossal magnetoresistant oxide $La_{2-2x}Sr_{1+2x}Mn_2O_7$ ($x = 0.36$) from angle-resolved photoemission. *Phys. Rev. B*, 76:235117, Dec 2007.

[260] X. Y. Huang, O. N. Mryasov, D. L. Novikov, and A. J. Freeman. Electronic and magnetic properties of layered colossal magnetoresistive oxides: $La_{1+2x}Sr_{2-2x}Mn_2O_7$. *Phys. Rev. B*, 62:13318–13322, Nov 2000.

[261] J. M. Luttinger. Fermi surface and some simple equilibrium properties of a system of interacting fermions. *Phys. Rev.*, 119:1153–1163, Aug 1960.

[262] C. Aruta, G. Ghiringhelli, V. Bisogni, L. Braicovich, N. B. Brookes, A. Tebano, and G. Balestrino. Orbital occupation, atomic moments, and magnetic ordering at interfaces of manganite thin films. *Phys. Rev. B*, 80:014431, Jul 2009.

[263] C. T. Chen, Y. U. Idzerda, H.-J. Lin, N. V. Smith, G. Meigs, E. Chaban, G. H. Ho, E. Pellegrin, and F. Sette. Experimental confirmation of the x-ray magnetic circular dichroism sum rules for iron and cobalt. *Phys. Rev. Lett.*, 75:152–155, Jul 1995.

[264] T. Koide, H. Miyauchi, J. Okamoto, T. Shidara, T. Sekine, T. Saitoh, A. Fujimori, H. Fukutani, M. Takano, and Y. Takeda. Close correlation between the magnetic moments, lattice distortions, and hybridization in $LaMnO_3$ and $La_{1-x}Sr_xMnO_{3+\delta}$: Doping-dependent magnetic circular x-ray dichroism study. *Phys. Rev. Lett.*, 87:246404, Nov 2001.